



Dynamique d'aimantation dans les jonctions tunnels magnétiques à anisotropie perpendiculaire

Thu Nhi Tran Thi

► To cite this version:

Thu Nhi Tran Thi. Dynamique d'aimantation dans les jonctions tunnels magnétiques à anisotropie perpendiculaire. Materials Science [cond-mat.mtrl-sci]. Université Joseph-Fourier - Grenoble I, 2009. English. NNT : . tel-00967000

HAL Id: tel-00967000

<https://theses.hal.science/tel-00967000>

Submitted on 27 Mar 2014

HAL is a multi-disciplinary open access archive for the deposit and dissemination of scientific research documents, whether they are published or not. The documents may come from teaching and research institutions in France or abroad, or from public or private research centers.

L'archive ouverte pluridisciplinaire **HAL**, est destinée au dépôt et à la diffusion de documents scientifiques de niveau recherche, publiés ou non, émanant des établissements d'enseignement et de recherche français ou étrangers, des laboratoires publics ou privés.

THÈSE

présentée par

Thu-Nhi TRAN THI

En vue de l'obtention du grade de
DOCTEUR DE L'UNIVERSITÉ JOSEPH FOURIER
(loi du 30 mars 1992)

Spécialité : Physique de la Matière Condensée et du Rayonnement

Dynamique d'aimantation dans les jonctions tunnels magnétiques à anisotropie perpendiculaire

Défendue publiquement le 16 juin 2009

Jury

Messieurs	D. RAVELOSONA	Rapporteur
	S. MANGIN	Rapporteur
	A. SCHUHL	
Madame	A. MOUGIN	
Messieurs	Y. SAMSON	
	P. WARIN	

Cette these a été effectuée au
CEA – Institut NAno science et Cryogénie – NanoMagnetisme – Grenoble – France

TABLE OF CONTENTS

1	Fundamentals and concepts of Domain wall Propagation and MTJ with epitaxial barrier.....	13
1.1	Introduction on the study on magnetic domain wall	14
1.2	Theory of magnetic domains and domain walls	15
1.2.1	The basis of wall motion and Landau-Lifshitz theory	16
1.2.2	Gilbert Damping factor	16
1.2.3	Domain wall dynamics in one dimension.....	17
1.2.3.1	Moving domain wall	17
1.2.3.2	Walker breakdown	18
1.2.3.3	Creep and flow regimes of domain wall motion with perpendicular anisotropy	19
1.2.3.4	Wall velocity and stability in systems of reduced dimensions	20
1.2.4	Review of the propagation process in the perpendicular anisotropy thin film	21
1.3	MTJ with epitaxial barrier	22
1.4	FePt alloy.....	26
2	Experimental techniques and simulation used.....	29
2.1	MBE system	30
2.1.1	Description of MBE system	30
2.1.2	Description of the used chamber.....	31
2.1.2.1	Description of the e-beam	31
2.1.3	Thickness control.....	31
2.1.4	Sample cleaning.....	31
2.1.4.1	Ex-situ cleaning	31
2.1.4.2	In-situ cleaning	32
2.1.5	Substrate	32

2.2	Principle of X-Ray Diffraction	32
2.3	The vibrating sample magnetometer VSM technique.....	33
2.4	Magneto – optical effect	34
2.5	Kerr polar Microscopy MOKE.....	36
2.5.1	Polar Kerr Microscopy Set-Up (in LPS)	36
2.5.2	Magnetic Field Pulse Generation.....	37
2.5.3	Recording Magneto-optical Images.....	39
2.5.4	Optical resolution and magneto-optical contrast.....	40
2.5.5	Experimental method to study domain wall velocity.....	40
2.6	Simulation method for domain wall motion with perpendicular magnetization.....	41
3	Growth, structural and magnetic characterizations.....	43
3.1	Growth process.....	44
3.1.1	Description of the growth of each layer	44
3.1.2	Growing conditions.....	45
3.2	Structural characterizations	46
3.2.1	Anisotropy of FePt thin film.....	47
3.2.2	Magnetic characterizations	48
3.2.3	A few words on FePt/MgO/FePt tunnel junction transport properties.....	50
3.3	Conclusion.....	51
4	Magnetization dynamic and Domain wall propagation in FePt single layer.....	53
4.1	Study of propagation of magnetic domain walls in FePt single layer	54
4.1.1	At thickness from 2 to 5 nm.....	54
4.1.1.1	Propagation depending on field	54
4.1.1.2	Time dependent propagation	58
4.1.1.3	Demagnetization state	61
4.1.1.4	Conclusion.....	62
4.1.2	Domain decoration when increasing thickness	62
4.1.2.1	Observing the vestigial 360° winding wall	63
4.1.2.2	Propagation at low field.....	64
4.1.2.3	Propagation at high field.....	65
4.2	Study on domain wall velocity in FePt single sample	67
4.2.1	Introduction	67
4.2.2	Domain wall velocity in FePt single layer with different thickness	68
4.2.2.1	The quick view from experiment data.....	69
4.2.3	Calculations from hypothesis of the regime where experiment data stay for single sample	70
4.2.3.1	The first hypothesis: we are in the regime with Walker breakdown.	70
4.2.3.2	The second hypothesis: we are in the precessional regime above the Walker breakdown	73
4.2.4	Simulation of domain wall motion with perpendicular magnetization	75
4.2.5	Conclusions	79
4.3	Conclusions	79

5	Magnetization dynamic and DW motion in FePt/MgO/FePt MTJ.....	81
5.1	Study on propagation of magnetic domain walls in MTJ sample.....	82
5.1.1	Applying field around the first reversal	83
5.1.2	Applying field between reversal of the soft layer and of the hard layer	85
5.1.3	Around the second reversal: 2.32 kOe	88
5.1.4	Demagnetization.....	89
5.1.5	Conclusion	91
5.2	Study on domain wall velocity in MTJ sample.....	91
5.2.1	MOKE results for domain wall velocity in MTJ sample	91
5.2.2	Comparison between MTJ sample and 5nm MTJ sample	93
5.2.3	Analysis of the experimental results of DW propagation in MTJ	94
5.2.4	Conclusion	95
5.3	Demagnetizing the hard layer by cycling the soft layer	96
5.3.1	Introduction.....	96
5.3.2	Kerr effect experiment for cycling measurements	97
5.3.2.1	Kerr- effect measurement.....	97
5.3.2.2	Observation of the demagnetization of the structure by cycling the soft layer	98
5.3.2.3	Behavior of amplitude and centre of the minor loop during cycling process.....	100
5.3.2.4	Demagnetizing procedure under different value of applied field for cycling H_{cyc}	102
5.3.3	MFM experiment.....	105
5.3.3.1	MFM experiment at various points of the cycling experiment.....	105
5.3.3.2	MFM experiments to observe domains of both soft and hard layer at lower applied field $H_{cyc} = 1.8$ kOe	107
5.3.4	Mathematical analysis of the behavior of the centre and remanent amplitude during cycling.....	111
5.3.4.1	Formula for centre of minor loop.....	111
5.3.4.2	Formula for remanent amplitude of minor loop	116
5.3.5	Conclusion	117

TABLE OF FIGURES

Fig. 1.1: Structure of a Bloch wall in a uniaxial crystal. The magnetization vector remains always normal to the x direction. [LEE80]	15
Fig. 1.2: Structure of a Néel wall in a uniaxial crystal. The magnetization vector remains always parallel to the xz plane.	15
Fig. 1.3: The figure shows a section of a 180° Bloch wall containing a vertical Bloch line (BL) in the centre. The magnetization directions indicated are those of the centre of the wall. The Bloch line carries a Bloch point (BP).....	15
Fig. 1.4: in a moving domain wall the magnetization is rotated upwards by the torque of the demagnetization field. The peak velocity is reached at $\phi = \pi / 4$ or $\phi = 3\pi / 4$ where this torque reached its maximum [LEE80].	17
Fig. 1.5: Wall velocity normalized to the Walker velocity $V_w = \gamma \Delta K' / M$ as a function of drive field H for three values of damping α [MAL79].	19
Fig. 1.6: theoretical variation of the velocity [MET07]:.....	19
Fig. 1.7: Sketch of a 180° domain wall's velocity as a function of an external magnetic field H. This cartoon indicates the two linear regimes of velocity, below and far above the Walker breakdown. The dotted line in the transient non-linear regime is a guide for the eyes.	20
Fig. 1.8: The calculated transmission probabilities as a function of $k_{ }$ in the Fe(100)/MgO(100)/Fe(100) system for 8 ML MgO for:.....	24
Fig. 1.9: Tunneling DOS for $k_{ } = 0$ for Fe(100)/8MgO/Fe(100).	25
Fig. 1.10: Conductance as a function of the number of MgO layers [BUT01]......	26
Fig. 1.11: FePt alloy ordered in the L1 ₀ phase.	28
Fig. 2.1: Scheme of the MBE system.	30
Fig. 2.2: in-situ cleaning process by heating with 5A current is considered to 550°C.	32
Fig. 2.3: Crystalline structure of MgO substrate.	32
Fig. 2.4: X-Ray Diffraction principle.	33
Fig. 2.5: MOKE set up.	34
Fig. 2.6: Kerr Polar Microscopy Set-Up.	36
Fig. 2.7: schema of the experiment with the various electronic apparatus.....	37
Fig. 2.8: the Sample holder.	38

Fig. 2.9: Computation modeling with the width w and the thickness t .	41
Fig. 3.1: MTJ structure on substrate MgO (001).	44
Fig. 3.2: RHEED patterns of the different layers of this structure.	45
Fig. 3.3: Structural characterizations of Perpendicular MTJ	47
Fig. 3.4: Hysteresis loop out of plane, in plane and difference of the two curves for 4 nm (a) and 2 nm (b) FePt thin film.	48
Fig. 3.5: Hysteresis loops of FePt layers with different thickness, measured by Kerr Polar effect under the perpendicular applied field.	49
Fig. 3.6: Hysteresis loop of perpendicular MTJ.	50
Fig. 3.7: a) $I(V)$ curve at 300 K for a FePt/MgO(2 nm)/FePt junction in parallel configuration b) Conductance derived from curve a).	51
Fig. 4.1: PMOKE images of field evolution of the magnetic domain structure for sample FePt 2 nm, starting from negative magnetization saturation:	55
Fig. 4.3: PMOKE images of single sample FePt 5 nm	57
Fig. 4.4: PMOKE images of single sample FePt 5 nm under the high field during a short time	58
Fig. 4.5: PMOKE images of time evolution of magnetic domain structure of single FePt(4 nm) layer under the same field: 1913 Oe.	60
Fig. 4.6: PMOKE images of time evolution of magnetic domain structure of single FePt _{4nm} layer under the high field: 2527 Oe.	61
Fig. 4.8: PMOKE to observe vestigial domains for a 6 nm thick FePt layer	62
Fig. 4.9: PMOKE for sample FePt 6 nm at low field.	64
Fig. 4.10: PMOKE of ring decoration and magnetized channels in side for sample FePt 6 nm	65
Fig. 4.11: PMOKE of sample FePt 6 nm under the field $H = 1700$ Oe.	66
Fig. 4.12: PMOKE of sample FePt 6 nm under the field $H = 1770$ Oe.	66
Fig. 4.13: Domain wall velocity as a function of applied field with different thickness of FePt.	68
Fig. 4.14: Domain wall velocity $v = mH$ for different thicknesses of FePt in the hypothesis of steady regime with $m = \gamma(\delta/\alpha)$.	71
Fig. 4.15: Domain wall velocity $v = mH$ with different thickness of FePt in hypothesis of precessional regime with $m = \gamma\delta/(\alpha + \alpha^{-1}) + v_0$.	73
Fig. 4.16: Time evolution of domain wall position and velocity	75
Fig. 4.17: Simulation of domain wall velocity versus field at several value of damping vector α .	76
Fig. 5.1: Room temperature polar Kerr hysteresis loop of the MTJ structure. Only the decreasing field part has been measured. The other part was obtained by symmetry.	82
Fig. 5.2: PMOKE images obtained from magnetic configurations under low fields	83
Fig. 5.3: PMOKE images of magnetic configurations with positive saturation +4.2 kOe	84
Fig. 5.4: PMOKE image of the magnetic configuration after a field pulse: $H = 1.803$ Oe during $\Delta t = 2$ s.	85
Fig. 5.5: PMOKE images showing the propagation of the soft layer and nucleation of the hard layer after different field pulses. For all the images, the indicated fields were applied during $\Delta t = (0.3 + 0.8 + 1.2)$ μ s.	85
Fig. 5.6: magnetic stray field created above the domain wall in the soft layer within the hard layer.	86
Fig. 5.7: PMOKE image of magnetic configurations starting with positive magnetic saturation:	87
Fig. 5.8: PMOKE for sample FePt starting with negative magnetic saturation.	88
Fig. 5.9: PMOKE images for magnetic behaviors of the hard layer.	89
Fig. 5.10: PMOKE images of ac-demagnetizing.	90
Fig. 5.11: Domain wall velocity, v , versus applied magnetic field H for the MTJ sample (red points are experimental data – blue line is only a guide for the eyes).	92
Fig. 5.12: Fitting velocity with two different regimes.	95
Fig. 5.13: The change in remanent magnetization of the reference layers with numbers of field cycles or rotations of the free layers, plotted on a logarithmic scale. The curves are	

normalized by the remanent magnetization M_R , set at 5000 Oe before cycling or rotating. [GID98].....	97
Fig. 5.14: Demagnetization of the MTJ by the cycling the soft layer between the field $-H_{cyc} = -1.83$ kOe and $H_{cyc} = 1.83$ kOe. The angle of the Kerr signal is measured in μV	98
Fig. 5.15: the evolution of remanent signal (amplitude of the loop on the zero field axis) and centre of minor loop after 200 cycles with the applied field $H_{cyc} = 1.9$ kOe. The ellipticity of the Kerr signal is measured in μV	100
Fig. 5.16: Demagnetization of hard layer by cycling the soft layer at different field and the evolution of centre and remanent amplitude of minor loop during cycling procedure	103
Fig. 5.17: Centre of minor loop after normalization.	104
Fig. 5.18: AFM image for the area where is taken MFM images. All the MFM images report after were taken carefully at almost the same area of the same sample.	104
Fig. 5.19: MFM images of magnetic configuration during cycling procedure with applied field $H_{deg} = 2.0$ kOe.	105
Fig. 5.20: Cycling the soft layer at 1.8 kOe during 300 cycles.	108
Fig. 5.21: Cycling the soft layer at 1.8 kOe during 30 cycles with some different value of H_{end}	108
Fig. 5.22: variations of the position of the centre in Kerr measurements during cycling. The fitting curve is an exponential decay.....	111
Fig. 5.23: variations of the position of the centre in Kerr measurements during cycling. The two fitting curves are exponential decays, one with a demagnetization parameter of 82 mV and the other one with a constrained value of 127 mV.	112
Fig. 5.24: characteristic number of cycles during a demagnetization process versus the applied field. The data shows an exponential behavior with a characteristic applied field $H_0 = 0.12$ kOe.....	114
Fig. 5.25: variations of the remanent amplitude of the cycle in Kerr measurements during cycling. The fitting curves are exponential decays.	115

GENERAL INTRODUCTION

It has been just a year since spintronic was recognized as a major scientific achievement by the Nobel committee from the Swedish academy of science: in 2008, the committee awarded the Nobel Prize to Albert Fert and Peter Grünberg for their discovery of the giant magnetoresistance. Performed 20 years ago, this discovery opened the path to a tremendous increase in the bit density of hard drive disk that shifted from 20% per year to 60 % per year after the introduction of the spin valves in recording heads. It also led to the development of a new generation of memory device: the MRAM (for Magnetic Random Access Memory).

Such progresses and perspectives fueled and have been fueled by a huge interest and effort in research laboratories in the field of magneto-electronic. In the same period, some old subjects have been unearthed, and new discoveries made. Still now, magnetoelectronics is more than ever buzzing (to use a trendy word) and bursting with life, mostly because of a strong interplay between fundamental physics and applications. Certainly, the secret desire to uncover and to apply new concepts drives many researchers across the world.

We can trace the birth of spintronic to two main ideas. One is that in a naive picture the spin polarized current in a ferromagnet is carried by two currents - up and down spin carriers - flowing independently from each other. This is the “two currents” model from Mott. It is well known that the underlying hypothesis might not always be verified, but the Mott model allowed researchers to explain the resistivity curves of ferromagnets as the function of temperature.

Other key aspects, often forgotten, are the major progresses made in the 70's and the beginning of the 80's for the growth of ultra thin films and multilayers. People around the world became able to grow stacks of materials with a better control of the interfaces, and with a higher intrinsic quality of each layers... One important discovery then made possible was the antiferromagnetic coupling between ferromagnetic layers in ferro-normal metal multilayers [GRU86]. This latter discovery was one of the key ingredients of the discovery of GMR [BAI88].

In 1995 Moodera and coworkers [MOO95] observed tunnel magnetoresistance at room temperature in alumina based magnetic tunnel junction (MTJ). This observation paved the way for another step in the information storage technology. It also led to the concept of MRAM (Magnetic Random Access Memory). Then, for many years, researchers tried to improve

alumina based MTJ for the MRAM application. High voltage throughput, homogeneities on the scale of the silicon wafer, high TMR ratio were some of the issues tackled at that time.

I tried to show, with a few examples, that spintronic has been a very active field in the last 20 years. It has also revived the interest for magnetism in metal from slumber. Basic studies and technical progresses have both been helped by the invention of STM and of some linked techniques like Atomic Force Microscopy (AFM) and Magnetic Force Microscopy (MFM). Near field observation techniques and progress in patterning techniques enabled researchers to design and observe smaller and smaller structures down to the nanoscale. Theories have been tested, refined or rejected. One should never forget the importance of the technical progress in the advancement of science.

Most importantly regarding this thesis work, spintronics does not require the sole understanding of electronic transport, but also the fine mastering of magnetization phenomena in thin magnetic films, and in magnetic multilayers. Controlling magnetization reversal at an always reduced scale is indeed required to store and read information in all kind of magnetic devices.

For decades, the desire to anticipate the need of the storage industry for higher data densities pushed scientists to investigate more closely materials with strong perpendicular anisotropy. Such materials were used as model materials because they could be viewed as one-dimensional, at least with respect to some of their properties. They had hours of glory in the 70's with the "bubble memory". Many important theories were first introduced at that time. However, as the interest for bubble memory faded away, high perpendicular anisotropy materials were put back on the shelves of the laboratory. They were still used as model materials, but their use in magnetic media was regularly postponed by the progresses of longitudinal media. Finally, thin layers with perpendicular anisotropies are used in the magnetic hard disk since 2005.

Such thin films with perpendicular magnetic anisotropy offer a fascinating playground to the physicist:

- truly uniaxial perpendicular anisotropy can be readily obtained, either by building stackings with suitable interface anisotropy (such as Pt/Co/Pt trilayers), either by establishing uniaxial chemical ordering in chemically ordered alloys such as FePt.
- there is a competition between the perpendicular magnetic anisotropy and the magnetostatic field. This latter parameter favors in plane magnetization in thin films, but, when the perpendicular anisotropy is dominant, is at the origin of the formation of magnetic domains (and hence magnetic domain walls).

As a result, conversely to what is observed in systems with in plane magnetization, domain walls are not linked to a specific magnetic history and / or to sample defects, but are intrinsically part of the equilibrium magnetic state of the material. Indeed, the energy cost (anisotropy, exchange) related to the formation of the magnetic domain walls is compensated by a gain in the magnetostatic energy of the system when dividing the perpendicularly magnetized thin films in up and down domains [GEH97A, GEH97B, GEH99].

Let us now shift our discussion from thin layers to magnetic multilayers. Magnetic tunnel junctions are not focusing interest only because of the applied perspectives derived from their specific transport properties, or even because of the rich physics associated with spin filtering and induced by the epitaxial nature of the stacking. Indeed, in addition to electronic transport physics, Magnetic Tunnel Junctions also exhibit highly interesting magnetic properties, as being made of two ferromagnetic electrodes very close to each other. Average distance between the two ferromagnetic layers (thickness of the electrically insulating layer) is between 1 and a few nm. Practically, the question of a magnetic coupling between the two layers is of the utmost importance. Indeed, both spin valves based recording heads and MTJ based MRAM cells rely

on the magnetic stability of one of the two ferromagnetic electrodes, the so-called reference layer. Let us remind that this stability is ensured by exchange coupling of one of the magnetic layer (the reference layer) with an antiferromagnet in most devices.

In the case of MTJ with in plane magnetization, it has been shown that the hard layer can be demagnetized by cycling the soft layer – even when the cycling field is lower than the coercive field of the hard layer - at least in the absence of pinning by an antiferromagnet [GID98]. This has been explained by the action of the stray field created in the hard layer in the vicinity of the domain walls propagating in the soft layer during its magnetization reversal. Obviously, one could ask what will happen in MTJ with perpendicular magnetic layers, when stray field would be involved in both the interactions between magnetic layers and in defining the equilibrium size of the magnetic domains. Till now, similar studies are not numerous and the very few existing ones have been reported on spin valves - like magnetic systems [WIE06]. Nevertheless, these latter studies, often relying on MFM and Kerr observations, have shown that coupling between the two ferromagnetic electrodes gives rise to interesting magnetic patterns like decoration domains, domains mirroring... It is then tempting to investigate further this area. However almost nothing has been published on the dynamical properties of such systems, and this can be easily understood.

Indeed, until recently, the physics of domain wall propagation was of reduced interest for most of spintronics devices. MRAM cells or magnetic recording heads tended to rely on elements with a single domain configuration. This changed recently as new concepts of spintronics devices based on magnetic domain walls (DWs) have been proposed [ALL05], with the concept of racetrack memory emerging from the group of S. Parkin [PAR08]. In the most advanced designs, such memories would rely on the direct manipulation of magnetic walls using spin polarized electrical current (so-called Spin Transfer mechanism (ST)). This emerging field promises very low power consumption, simple architectures, ultra-fast operations, 3D stacking and thus has the potential to become a key technology for non-volatile memories and logic circuits. Here, materials with perpendicular magnetic anisotropy offer specific advantages as the large achievable anisotropy ends up with thin magnetic domain walls (a few nm in FePt thin films). So, thin domain walls are obviously desirable when targeting high data densities. They are also probably advantageous as the efficiency of current driven DW motion is probably strongly enhanced at such reduced domain wall widths.

These ideas currently fuel a strong interest in the physics of domain wall propagation in thin films with perpendicular anisotropy. Together with multilayers such as the widely studied Pt/Co/Pt, FePt is one of the preferred materials for such studies. Indeed, such alloys (FePt, FePd...) exhibit large magneto-optical effects, making these well-suited to use polar magneto-optical Kerr effect (MOKE) to study their magnetic properties in the static and dynamic cases. In addition, the large magnetization also facilitates local and high resolution observations by Magnetic Force Microscopy. Coupling both techniques then offer insight in the system properties combining time and spatial resolutions

This Phd work has then been focused on some emerging questions in these promising areas:

- What can be said of the domain wall dynamics in thin films with perpendicular anisotropy (FePt), going beyond the limit of the ultra-low thicknesses associated with the Pt/Co/Pt system?
- What are the phenomena occurring upon magnetization reversal in MTJ-like systems with perpendicular magnetization (FePt/MgO/FePt)?

We then focused our work on a thorough study concerning magnetic coupling between the hard and the soft layer of a fully-epitaxial Magnetic Tunnel Junction with perpendicular magnetization (FePt/MgO/FePt). In the first part of this manuscript, we start describing the fundamental concepts of magnetic domain walls in thin films with perpendicular magnetization as well as some theoretical elements on Magnetic Tunnel Junctions.

In the second part, we describe the main experimental techniques we used and some results common to both out-of-plane FePt single layers and FePt/MgO/FePt Magnetic Tunnel Junction. The third part reports on the growth and the basic characterization of the FePt thin layers and FePt/MgO/FePt MTJ.

The fourth part deals with FePt single layers with high perpendicular anisotropy. These studies are on two directions. First, the polar magneto-optic Kerr effect is used to observe the domain wall propagation on FePt single layer. Taking advantage of the bulk origin the magneto-crystalline anisotropy, the thickness of FePt was varied from 2 nm to 6 nm while preserving a large perpendicular anisotropy. Here, the behaviors of the domain wall are investigated in details. Second, the domain wall speed was measured as a function of the value of an applied perpendicular magnetic field. Then, the nature of the propagation regime was analyzed according to different hypothesis. Domain wall motion simulations are included confirming the analysis of the experimental data.

The fifth part deals first with similar studies on perpendicular magnetization FePt/MgO/FePt MTJ. We now focus on the additional complexity introduced by the coupling between the soft and the hard layer. Then, to answer the question about the interdependency between the two electrodes, Kerr – effect experiments were done to follow the magnetization of both magnetic layers when cycling the soft layer. Additional insight into the involved processes was provided by Magnetic Force Microscopy images. These images uncovered unique and unexpected magnetic patterns in the hard layer at intermediate stage of the demagnetization process.

1 Fundamentals and concepts of Domain wall Propagation and MTJ with epitaxial barrier

1.1 Introduction on the study on magnetic domain wall

Magnetic domain walls (DWs) are one of the focus points for research in spintronic. The discovery that one could push DW [GRO02] with a current has renewed an already considerable interest in such objects. Because magnetic thin films and nanostructures needing no power to maintain magnetic states, it has been tried to use this ability either in reprogrammable logic [ALL05] or in memory devices like the MRAM or the racetrack memory [PAR08].

Static properties of magnetic domain walls have been investigated thoroughly. With the advance of microscopical techniques like Lorentz microscopy, magnetic force microscopy and kerr microscopy, a deep understanding has been achieved. The reader can refer to the book of Hubert and Schäffer [HUB98] to gain more insights into their properties. Our work has focused on the dynamic properties of high perpendicular anisotropy thin films. Therefore, I will only review the basic properties of out-of-plane domain wall (Bloch wall) in the first part of this chapter.

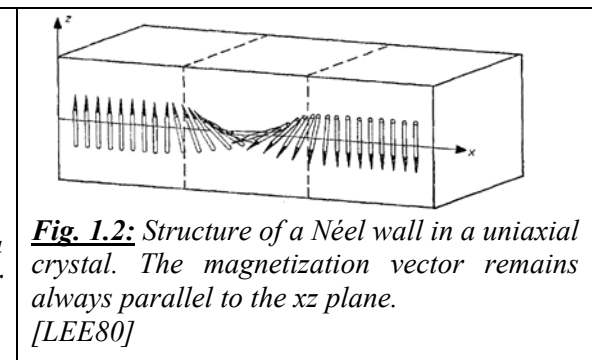
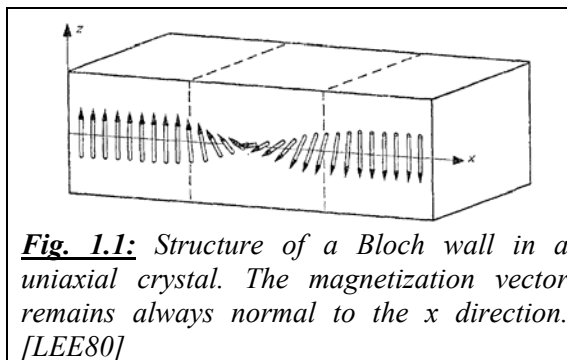
In high perpendicular anisotropy thin films, domains take the form of bubble. In the 70's, such a kind of domain was foreseen as the core of new memory devices. In spite of a strong effort from the community of magnetism, magnetic bubbles were abandoned. However this effort was transmitted to the future generation in one work that is the legacy of that era. The book of Malozemoff and Slonczewski [MAL79] is a "must read" to anyone interested in the dynamic properties of DW in high perpendicular anisotropy thin films. I will review the relevant ideas for our study in the second part of this chapter. I will introduce the different regimes of propagation that may be observed in our systems. A brief review of published experiments relevant to our work will also be presented.

In the racetrack device one way to measure the position of a moving DW is through its interaction with a sensing layer positioned above the DW. However the dynamic of coupled systems has not been studied in details. I will also review the published work on that topic.

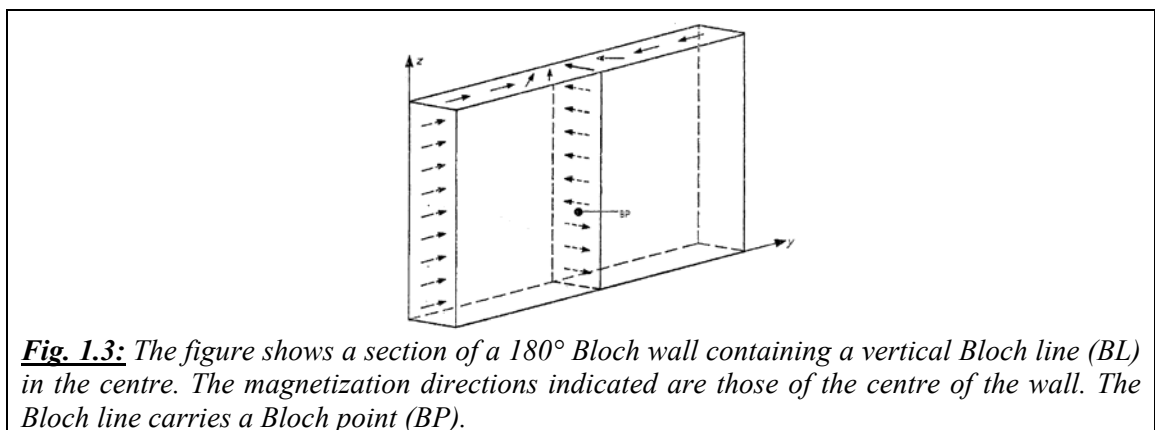
Finally, I will briefly introduce MTJ and why epitaxial MTJ have been such a revolution in the last 10 years.

1.2 Theory of magnetic domains and domain walls

Magnetic domains are formed into ferromagnetic materials to minimize the energy of the magnetic configuration. Several energy terms are to be taken into account to understand: crucial parameters for determining the size of the domains and the type of the boundaries between them are the shape of the sample, the saturation magnetization, the magnetic anisotropies... [LEE80]. Domain wall is the name by which we call the area of the sample that separate two adjacent domains with different magnetization orientations. We will restrict ourselves to the two basic types of domain walls: *Bloch walls* (Fig. 1.1) and *Néel walls* (Fig. 1.2).



In a 180° Bloch wall the magnetization vector rotates such that it always remains parallel to the plane of the wall. In a Néel wall the magnetization vector, while rotating, remains parallel to a plane normal to the wall. Néel wall may have a higher specific energy than the Bloch wall, due to the additional energy of the demagnetization field introduced by the free poles on the surface of the wall. In some cases, when the dimensions of the sample become comparable to the wall width, such as in thin permalloy films, the situation may reverse. Bloch and Néel walls have an additional degree of freedom: the sense of rotation may be clockwise or counter-clockwise. If in a Bloch wall both senses of rotation occur, the two wall type regions are separated by a *Bloch line* (Fig. 1.3). A Bloch line is a string-like discontinuity. It may contain *Bloch points* which are also shown in Fig. 1.3.



The domain structure of a ferromagnetic crystal is governed by the principle of minimum total energy, consisting in general of three different parts. The first part is the total wall energy, *i.e.*

the total surface of the wall multiplied by the specific wall energy per unit area. For most static problems, the specific wall energy is considered to have a constant value unaffected by stray fields. The non-zero width of the walls is usually disregarded. The second part consists of the total magnetization energy due to the external magnetic field. The third contribution is the magnetization energy due to the stray field of the domains. In general, the latter contribution is the most complex to evaluate. It has only been calculated for a limited number of simple domain structures. One of the domain structures which has been studied in detail is the domain structure in thin platelets of a uniaxial crystal with a preferential direction normal to the platelet. It is this basic geometry which has been used for most of the experiments described in the present review.

1.2.1 The basis of wall motion and Landau-Lifshitz theory

The physical basis of the dynamic process of wall motion is the gyroscopic precession of the electronic spin. This property of the electron determines directly the macroscopic properties: the magnetization vector responds orthogonally to the torque acting on it. The rate of change of the direction of the magnetization \mathbf{M} is described by the equation proposed by Landau and Lifshitz [MAL79]:

$$\dot{\mathbf{M}} = \gamma \mathbf{M} \times \frac{\delta w}{\delta \mathbf{M}} + \frac{\alpha \dot{\mathbf{M}} \times \mathbf{M}}{M} \quad (1.1)$$

This equation is the starting point for all discussions of bubble dynamics where $\gamma = ge/2mc (> 0)$ is the gyromagnetic ratio and α is the dimensionless Gilbert damping factor.

The term $\dot{\mathbf{M}}$ on the left hand side and $\frac{\alpha \dot{\mathbf{M}} \times \mathbf{M}}{M}$ on the right hand side maybe considered

“dynamic” terms because they contain a time derivative of M . By contrast the term $\gamma \mathbf{M} \times \frac{\delta w}{\delta \mathbf{M}}$ is

essentially a static term. If this term is zero, then equation (1.1) can be satisfied with $\dot{\mathbf{M}} = 0$, so that no spin motion or “precession” occurs. The static torque term is nonzero whenever the effective field H_e has a component normal to the spin direction.

The effective field can be conveniently expressed as the sum of two terms thusly:

$$H_e = -\frac{\delta w}{\delta \mathbf{M}} - \frac{\delta \dot{\mathbf{M}}}{\gamma \mathbf{M}}, \quad (1.2)$$

In the general case with H_e not constant, the total energy represented by the volume integral of Ω is conserved when $\alpha = 0$.

1.2.2 Gilbert Damping factor

Gilbert damping factor has been defined as the phenomenological coefficient of the non-conservative term of eq. (1.1).

For low damping, $\alpha \ll 1$, equation (1.1) describes a precession of the magnetization around the magnetic field having angular frequency $\omega = \lambda/\gamma M$. The damping term causes the precession angle to decrease.

For values of $\alpha \gg 1$ both terms are equivalent. The damping terms introduced here are empirical in nature but have proven useful for the description of various phenomena, such as ferromagnetic resonance and domain wall dynamics [WAL56].

1.2.3 Domain wall dynamics in one dimension

1.2.3.1 Moving domain wall

An external magnetic field along the z axis favors the orientation of the magnetization in one of the domains. Accordingly this domain will tend to grow and thereby displace the domain wall. Determining the equation of motion of a domain wall starts by studying the equation of motion for the magnetization $\mathbf{M}(r, t)$:

$$\frac{\delta \mathbf{M}(r, t)}{\delta t} = -\gamma \mathbf{T}(r, t) \quad (1.3)$$

where γ is the gyromagnetic ratio and $\mathbf{T}(r, t)$ is the total torque density. It contains contributions from exchange, anisotropy, magnetic fields and damping.

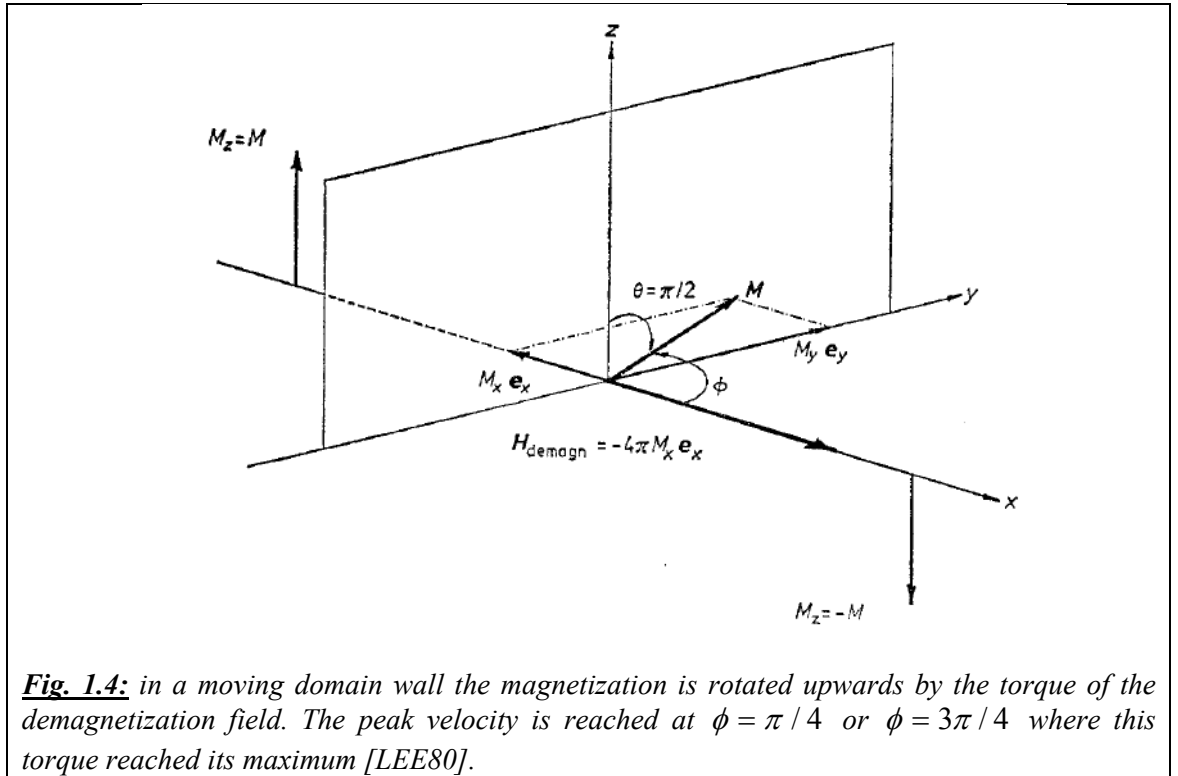
The equations of motion can then be integrated for a uniformly moving wall (Walker 1956 and Schlomann 1972) and give:

$$v = 2\gamma\Delta M \sin 2\phi (1 + Q^{-1} \cos^2 \phi)^{-1/2} \quad (1.4)$$

Where the quality factor Q is defined by:

$$Q = K_u / 2\pi M^2 = H / 4\pi M \quad (1.5)$$

Where K_u is the uniaxial anisotropy constant.



The applied field does not exert a torque moving the magnetization upward. This role is fulfilled by the demagnetization field. The torque acting on the magnetization is then:

$$-4\pi M^2 \sin \phi \cos \phi$$

The velocity expression is then:

$$v = -4\pi\Delta_{eff} M \sin \phi \cos \phi$$

From this expression of the velocity of the wall, it will be clear that there is an upper limit to the wall velocity due to the finite value of the demagnetizing field. In materials with $Q \gg 1$ the wall has a peak velocity:

$$v_p = 2\pi\gamma\Delta M \quad (1.6)$$

that is reached when

$$\phi = \pi/4 \quad \text{or} \quad \phi = 3\pi/4$$

This peak velocity is usually referred to as the Walker limit.

Equating these results we find a linear relationship between the velocity and the drive field:

$$v = \mu H \quad (1.7)$$

with the mobility μ given by:

$$\mu = \gamma\Delta / \alpha \quad (1.8)$$

Or:

$$v = \gamma\Delta H / \alpha$$

The velocity is in this case inversely proportional to α .

1.2.3.2 Walker breakdown

The domain-wall velocity is sustained by a torque on the in-plane magnetization. And according to the two static types of Bloch wall [LEE80], they have:

$$\dot{q}_{\max} \equiv v_W = 2\pi\gamma\Delta_0 M, \quad (1.9)$$

with q is the wall displacement along the x axis and M is the saturation magnetization.

The velocity occurs at a net drive field $H[= H_a - (kq/2M - H_c)]$ of:

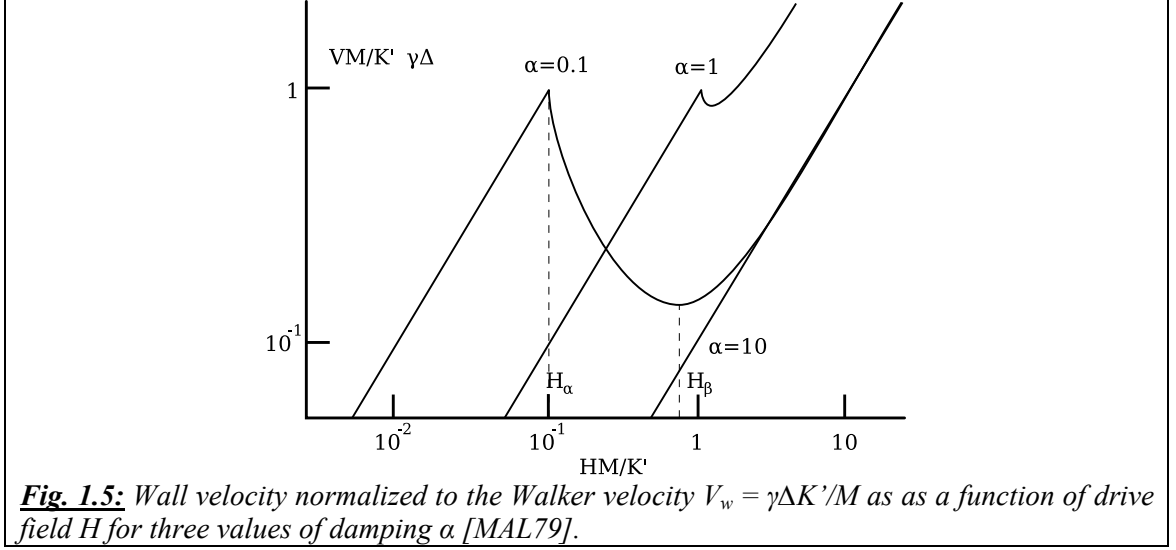
$$H_w = 2\pi\alpha M \quad (1.10)$$

These are the important formulae for the “Walker breakdown velocity” v_w and the “Walker critical field” H_w .

The critical velocity \dot{q}_{\max} in each of above cases corresponds to a critical drive field:

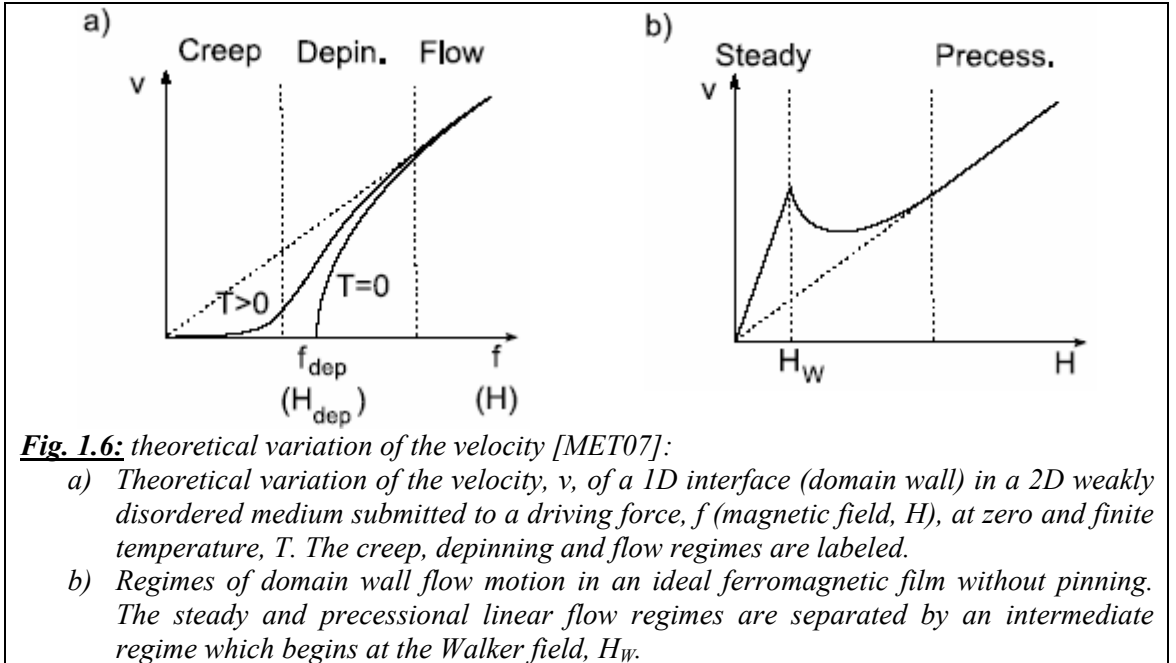
$$H_{\max} = \dot{q}_{\max} / \mu = \alpha \dot{q}_{\max} / \gamma\Delta_0. \quad (1.11)$$

Fig. 1.5 shows a plot of an analytic expression for the complete field dependence of the velocity average over a precessional cycle, for the case of demagnetizing an in – plane anisotropy torques. If the damping is small, the average velocity drops above the breakdown velocity and then increases again as the damping torque takes over. In the region of decreasing velocity or negative mobility, the domain wall is expected to be unstable, for if one area of the wall begins to lag, it experiences an increasing drive that, in this negative mobility region, will cause it to lag even further. Clearly the one dimensional model is inadequate to describe such behavior. If the damping is large ($\alpha \gg 1$), the nonlinearity in V versus H is suppressed altogether (see in Fig. 1.5).



1.2.3.3 Creep and flow regimes of domain wall motion with perpendicular anisotropy

Two theoretical variations of the velocity [MET07] are shown in Fig. 1.6. The dynamics of an elastic interface driven through a weakly disordered medium by an applied force is a challenging problem relevant to many physical systems such as domain walls in ferromagnetic and ferroelectric materials. While theory predicts three main regimes of motion only the low force regime of creep has been experimentally studied through direct observation of the interface, regimes beyond that of creep, namely depinning and flow, have however been evidenced indirectly via ac susceptibility measurements ([CHE02] and [KLE07]).



In these theories, at zero temperature, an elastic interface in the presence of weak disorder will be pinned for all driving forces, f , below the depinning force, f_{dep} , at which a critical depinning

transition occurs (Fig. 1.6a) At finite temperature the depinning transition becomes smeared due to thermal activation and a finite velocity is then expected for all non-zero forces. This is true even for $f \ll f_{\text{dep}}$ where the thermally activated interface motion is known as creep. At the other extreme, once f is sufficiently beyond f_{dep} , disorder becomes irrelevant resulting in a dissipative viscous flow motion with $v \approx f$. Finally, between the creep and flow regimes, a transitory depinning region is expected. In magnetic domain wall motion experiments, the applied magnetic field, H , plays the role of a force, f . The film's nanoscale inhomogeneties create the disorder which pins the wall and the domain wall energy provides the elasticity.

1.2.3.4 Wall velocity and stability in systems of reduced dimensions

According to [MOU07], the average velocity far above the Walker breakdown is simply given by:

$$\bar{v} = \gamma \Delta \frac{\alpha}{1 + \alpha^2} H \quad (1.12)$$

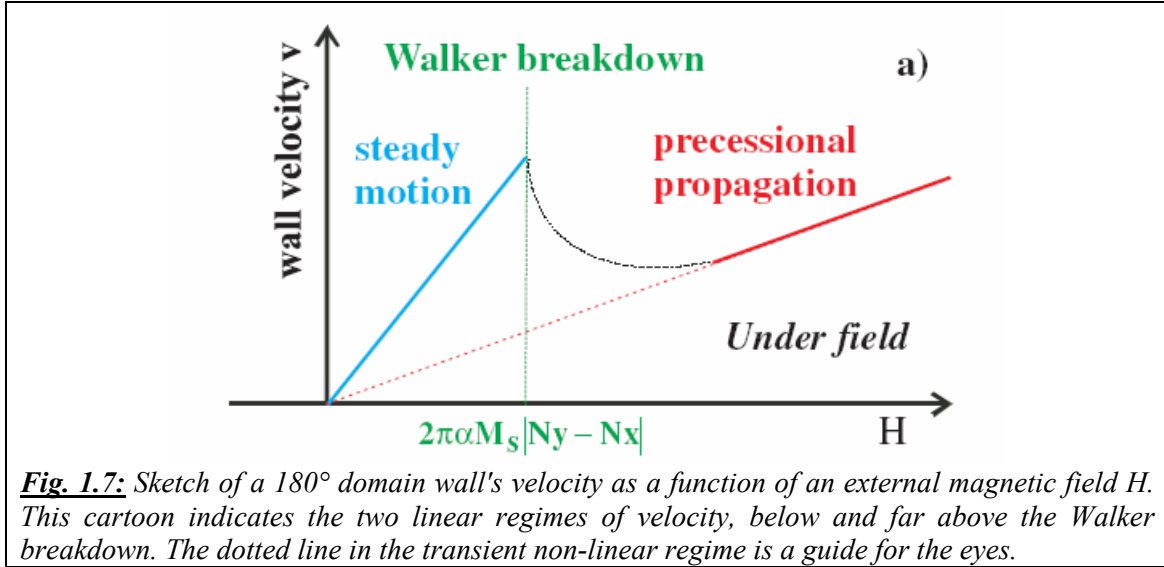
Where:

γ is the gyromagnetic ratio

Δ is characteristic domain wall width. It is a normalized value taken into account of a thin film with a small given value of thickness of the thin film.

u has the dimension of a velocity and scales as the electrical current density.

- This regime is similar to the usual high field one described for a 180° Bloch wall. The average velocity is linear with the field, following an initial drop in the mobility at the breakdown.



In a one-dimensional statement of wall motion, without current, a qualitative understanding of the damping/demagnetizing interrelation is easy to provide. When a drive field is applied along the anisotropy direction, \mathbf{M} starts a ϕ precession movement, and tilts away with respect to its equilibrium orientation at rest. The component of the magnetization outside of the xz wall plane creates magnetic charges. The θ component of the torque resulting from the induced magnetostatic field describes the resulting additional precession of the spin around \mathbf{H}_d .

At the Walker field, the wall reaches its maximum velocity in the linear regime. At that moment, the damping/demagnetizing torque and the drive field torque do not cancel each other

anymore. Then, above the Walker field, the motion is characterized by an oscillation around an equilibrium position. In the presence of damping, the forward movement is favored and thus the equilibrium position moves on.

1.2.4 Review of the propagation process in the perpendicular anisotropy thin film

Up to now, many studies on the propagation process in the perpendicular anisotropy thin film have been performed. The knowledge of dynamic behavior then developed strongly over the last decades. Lately this knowledge has also been used to study possible coupling between magnetic layers separated by a spacer layer. Recently, the group of Jacques Ferré from the Laboratoire de Physique des Solides at Orsay University obtained significant breakthroughs over the previous knowledge by imaging domain wall propagation with their MOKE experimental system. We report below some of the studies they have performed to provide to the reader a full picture of the recent studies of the propagation process in perpendicular anisotropy thin film study.

1. Their first report on the MOKE experiment study of high field DW dynamic is in Au/Co/Au films with perpendicular anisotropy [KIR93]. The Gilbert damping factors are derived from the study of DW velocity. The variation of DW velocity vs. the applied magnetic field can be distinguished by three regimes. They estimated approximate value of Gilbert damping from the viscous DW motion regime. The DW velocity in their case revealed the same qualitative behavior as in thicker bubble film or in bulk materials: at low field thermally activated jumplike motion, viscous motion at higher field (even if the relationship between the velocity and the field was not linear).

Continuing with the same system, in [FER97] they reported on the magnetization reversal process, starting from an initial demagnetized state. The dynamic of the magnetization reversal is much faster for the indirect process since it is initiated from quasi-homogeneous “Swiss cheese” domain state with small non reversed region which act as nucleation centers when the magnetic field is subsequently reversed. The distribution function of local coercivities can then be determined from the experimental field dependence of the domain wall velocity. As in thicker film, a direct consequence of a nanoscale distribution of the coercivity is domain – boundary jaggedness.

2. Dynamic studies of two ferromagnetic layers separated by a non magnetic one, like spin-valve or MTJ have not attracted much attention. One must say that any coupling between the two layers complicate significantly the interpretation of the experiment. It is then desirable to be able to study each layer individually. Bonfin and coworkers [BON01] used X-ray magnetic circular dichroism (XMCD) at different element edges to observe independently the reversal of the two layers in a Co/Al₂O₃/Ni₈₀Fe₂₀ MTJ in the nanoscale range. They showed that the coupling between the two layers may differ between the static regime and the dynamic regime they could observe. Fukumoto and coworkers [FUK06] used XMCD and X-ray photoemission electron microscopy on the same system to demonstrate the role of domain wall energy on the magnetization reversal of the soft layer in these MTJs. They observed that when the domains are small (perimeter below 2 μm) there is a delay in the domain expansion.
3. S. Wiebel *et al.* studied the magnetic domain structure of the hard layer: [Pt(1.8 nm)/Co(0.6 nm)] and the soft layer: [Co(0.6 nm)/Pt(1.8 nm)] separated by a Pt(4 nm) layer]

[WIE06]. They clearly showed the influence of dipolar coupling into the domain left in the remanent state, observing how domain decoration expands over time, even in the absence of any applied field. Moreover, at high field, the suppression of 360° domain walls in perpendicular system was reported.

4. In 2007, P. Metaxas *et al* [MET07] studied the domain wall velocity in ultrathin Pt/Co/Pt films with perpendicular anisotropy. For the first time, the complete velocity-field characteristics of a 1D interface in a 2D weakly disordered medium was reported, and obtained through direct measurements of domain wall motion in ultrathin Pt/Co/Pt films. The transition between thermally activated creep and viscous flow motion regimes - as predicted from general theories for drive elastic interfaces in weakly disordered media - are experimentally observed in this study. The authors also determined the value for the magnetic damping parameter based on the hypothesis of DW velocity staying in the precessional regime, which describes the dissipation occurring during flow motion.

Worth noting, almost nothing has been published on coupled systems, such as Magnetic Tunnel Junctions or Spin Valves systems. In such cases, two magnetic layers are separated by a thin insulating or metallic layers, whose thickness is in the nm range. Such a configuration results in unique behaviors as the two magnetic layers may strongly interact through the stray field creating by one of these on the other. If other interactions, such as RKKY coupling, may be significant in some specific cases, these are not to be considered in our systems. Finally, we emphasize that published studies (such as the one cited above) were performed in spin-valve like magnetic systems, while we are not aware of any detailed studies of the dynamics of coupled magnetic layers in magnetic tunnel junctions.

Metaxas *et al* [MET08] have conducted domain wall velocity measurement in coupled spin valve made of two ultrathin Co films separated by a 4 nm thick Pt spacer. The coupling manifests itself in the asymmetry between positive and negative driving field in the velocity measurement.

1.3 MTJ with epitaxial barrier

The magnetoresistance of magnetic tunnel junctions (MTJ) is of uncontested interest for key applications with, in particular, promising perspectives for the fabrication of nonvolatile memories: Magnetic Random Access Memories (MRAM). Till 1995 most studies have been performed on MTJs with a layer of amorphous alumina as insulating barrier between the ferromagnetic electrodes. Building upon continuous progresses, these studies produced systems with large and reproducible tunneling magnetoresistance (TMR), typically 50% at room temperature [TSY03].

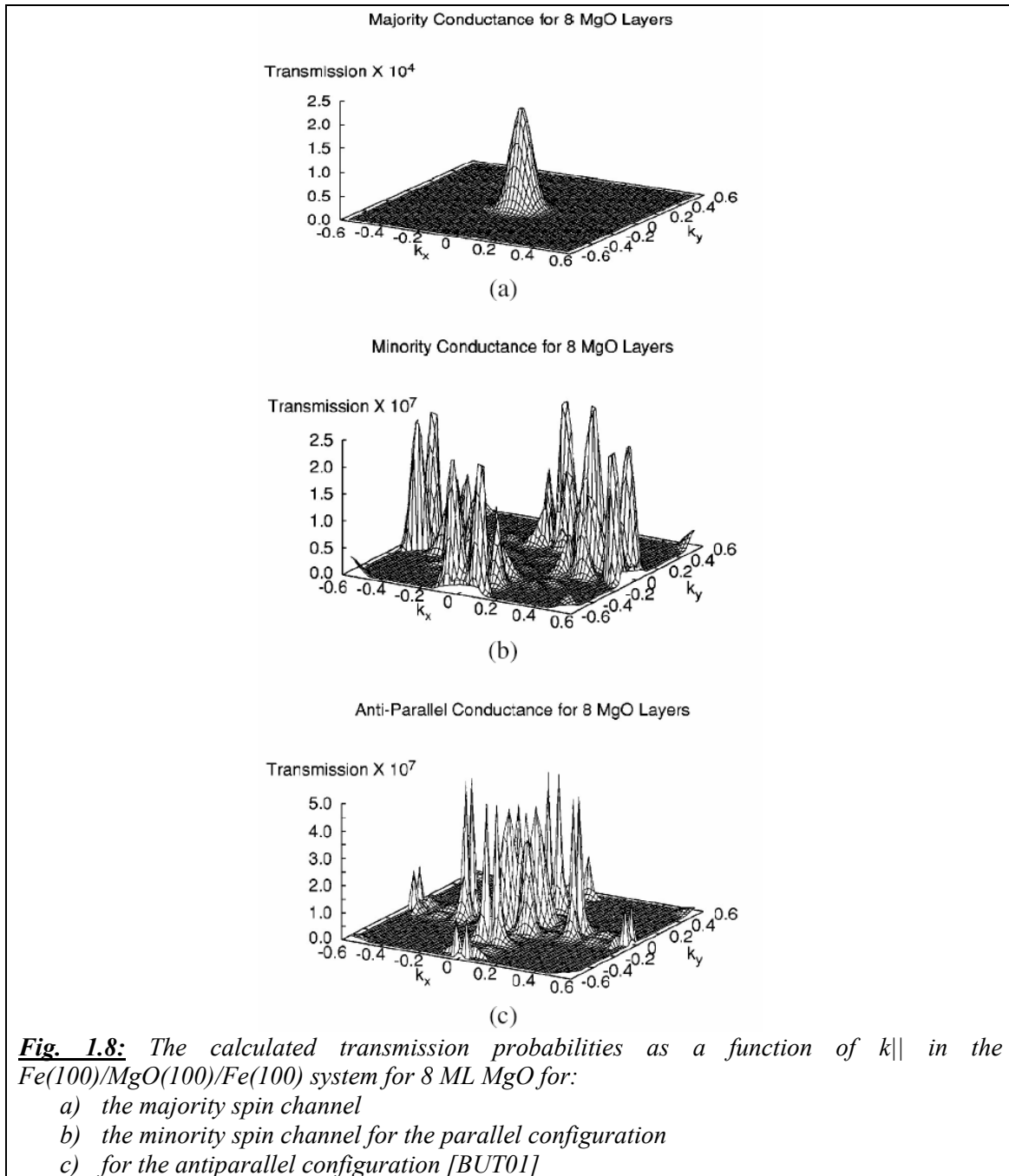
The theoretical picture is far more complex in systems with an epitaxial barrier. Indeed, a correct depiction of the spin-dependent tunneling properties of epitaxial MTJs must transcend the simple potential barrier image and take into account the interplay of electronic structure between metal and insulator. A test of these models can be performed on single-crystal epitaxial grown structures. Towards this end, much work has been dedicated to characterize the growth and electrical behavior of ultra thin MgO layers. The interest for MgO based MTJ comes from the seminal work of Butler and collaborators. It is this work that has initiated the vast interest in MgO based MTJ.

One of the simplest theoretical model systems is an epitaxial Fe(100)/MgO(100)/Fe(100) sandwich which is formed of two infinite stacks of Fe layers corresponding to the leads on either side of the barrier. Moreover, the Fe-MgO system provides a good template for experimental work because the Fe-MgO interface is such that Fe or MgO thicknesses can be reduced to a few atomic layers while preserving a good epitaxy.

The following theoretical description of the tunneling process in Fe/MgO/Fe sandwiches is taken from a recent publication of MacLaren *et al.*, which provides a reasonable theoretical approach for tunneling in layered epitaxial systems [BUT01]. The basic messages are:

- The tunneling conductance depends strongly on the symmetry of the Bloch states in the electrodes and of evanescent states in the barrier.
- Bloch states of different symmetry decay at different rates within the barrier.
- There may be quantum interference of the decaying states in the barrier.
- Interfacial resonance states can allow particular Bloch states to tunnel efficiently through the barrier.

In Fe(100)/MgO(100)/Fe(100) quite different tunneling mechanisms may dominate the conductance in the two spin channels. In Fig. 1.8 the calculated transmission probabilities are shown as a function of $k_{||}$ for (a) the majority spin channel and (b) the minority spin channel for the parallel as well as (c) for the antiparallel configuration of 8 layers of MgO. For the majority channel in Fig. 1.8a the conductance has a rather broad peak at $k_{||} = 0$. A somewhat similar peak is predicted for the tunneling of free electrons through a simple square barrier. The conductance has also an increasing amplitude of transmission near $k_{||} = 0$ as the insulating barrier layer is made thicker.



For a further clarification of the conductance process, the tunneling density of states (TDOS) has been examined, defined as the density of electron states subjected to the following boundary conditions. On the left-hand side of the interface there is an incoming Bloch state with unit flux and a reflected state. On the right-hand side are the corresponding Bloch states.

Fig. 1.9 [ZHA04] shows the TDOS associated with each of the Fe(100) Bloch states having $k_{||} = 0$. Both the majority (Fig. 1.9a) and the minority (Fig. 1.9b) channels have four Fe(100) Bloch states for $k_{||} = 0$. In the majority channel there is a Δ_1 state, a double degenerated Δ_5 state, and a Δ_2 state. The minority channel has four states with the same symmetries as the states of

the majority channel with the exception that the majority Δ_1 state is replaced by the Δ_2 minority state. Only the majority channel has a slowly decaying Δ_1 state, therefore, its conductance is much higher than the one of the minority channel. The next slowest decay is that of the Δ_5 states which are present in both channels. Both Fe channels have a Δ_2 state that couples to a Δ_2 state in the MgO barrier where it rapidly decreases because there are no real Δ_2 bands near the Fermi energy.

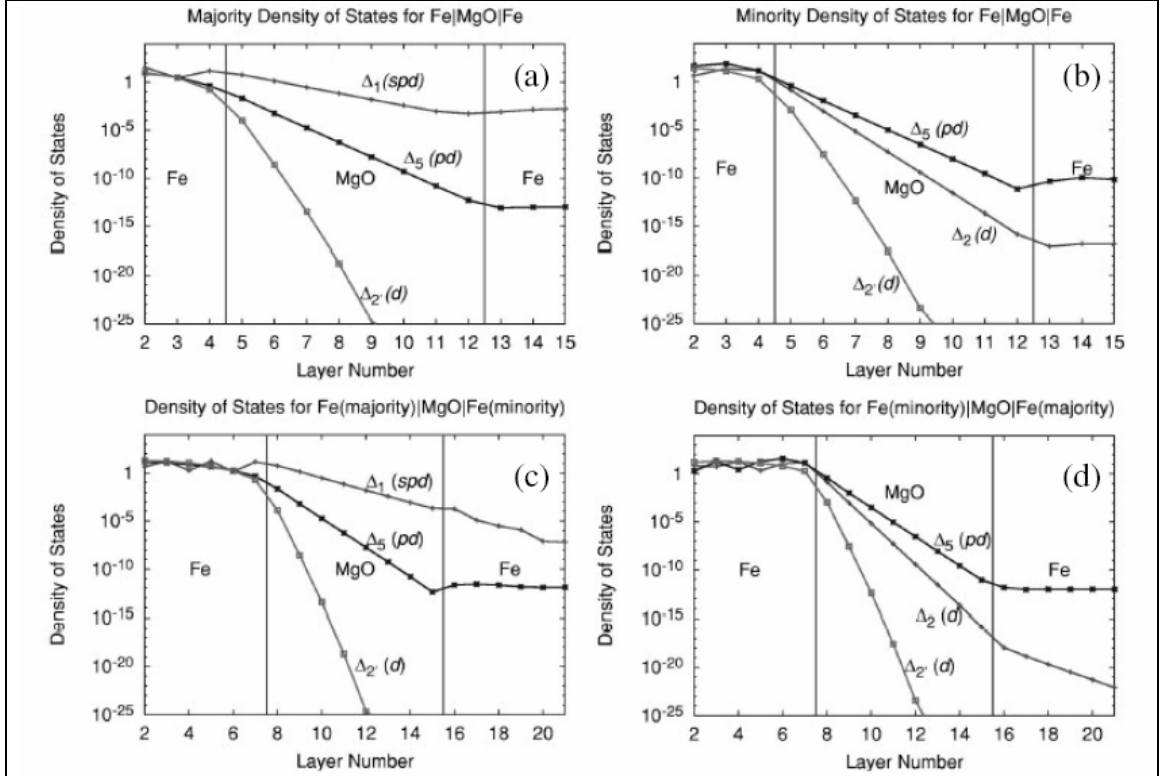
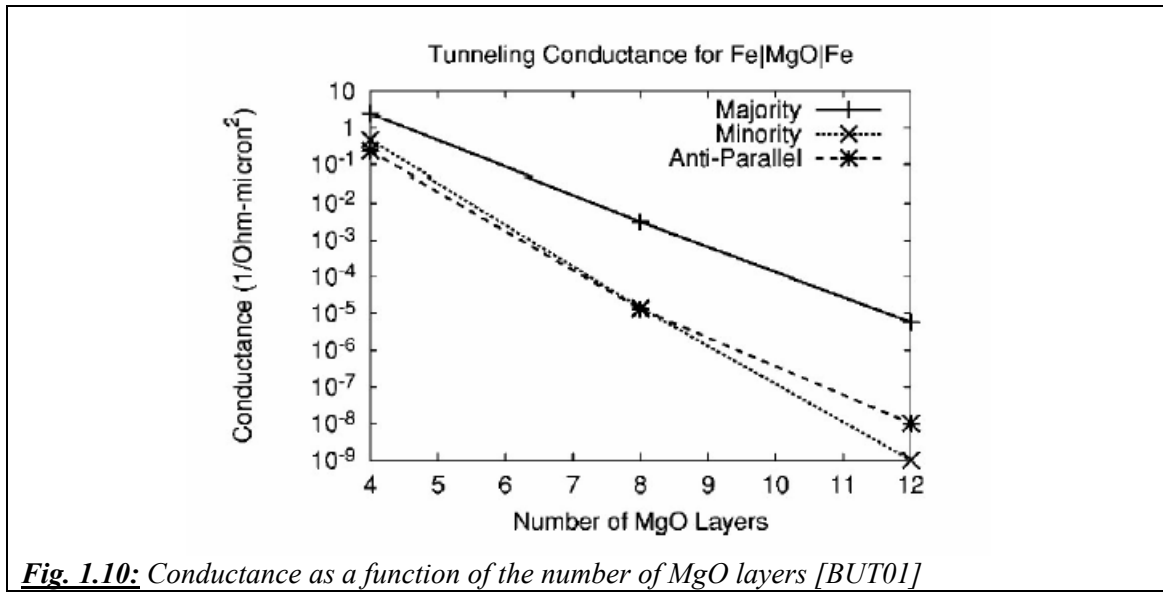


Fig. 1.9: Tunneling DOS for $k_{||} = 0$ for Fe(100)/8MgO/Fe(100).

The four panels show the tunneling DOS for majority (a), minority (b), and antiparallel alignment of the moments in the two electrodes (c) and (d). Additional Fe layers are included (c) and (d) to show the TDOS variation in the Fe. Each TDOS curve is labeled by the symmetry of the incident Bloch state in the left Fe electrode [ZHA04].

Fig. 1.10 demonstrates that for all thicknesses the majority conductance overwhelms the minority and the antiparallel conductance because of the slow decay of the Δ_1 states in MgO, leading also to an increasing TMR as the barrier thickness increases. Nevertheless, for thinner barriers the minority and antiparallel conductance are much closer to the majority conductance than for thicker barriers emphasizing the importance of the interfacial resonance states for very thin barriers.



1.4 FePt alloy

Strong uniaxial anisotropy is important for data storage. In the hard drive disk technology, information is stored as domain wall between domains of reverse magnetization (for in plane magnetic hard drive disk HDD) and as domains (for out of plane HDD). These domains consist of many small grains as much as possible magnetically decoupled from each other. The equilibrium direction of the magnetization is determined by both the shape anisotropy and the magnetocrystalline anisotropy. However thermal fluctuations can switch the magnetization direction of these grains if the anisotropy is not strong enough (superparamagnetism). The energy barrier associated with the anisotropy being proportional to the volume, the significant ratio indicative of the thermal stability of the recorded information is:

$$\tau = K_u \cdot V / k_b T \quad (1.13)$$

A widely accepted criterion is that the information should be stable over a ten year period. As a result, this ratio has to be larger than 30. With the demand for higher density data storage, the size of the bit continuously shrunk (typically down to 40 x 120 nm today), and the need to preserve the media Signal to Noise Ratio (SNR) required a parallel diminution of the grain size. As a result, the interest for strong uniaxial magnetic material (increasing K_u) has raised medias a way to compensate for the diminution of the grain volume (V). Materials belonging to the $L1_0$ alloys family (FePd, FePt...) attracted a specific interest as they exhibit the highest magnetocrystalline anisotropy.

The magnetic anisotropy of ferromagnetic materials

Ferromagnetic materials possess at least one easy axis of magnetization. This or (these axes) is (are) called axis (axes) of anisotropy. This anisotropy may be of different origin: crystalline, shape... Reversal along or perpendicular to the easy axis leads to completely different magnetization curves. The different competing energy terms entering into account when trying to understand magnetization reversal behavior are:

- Zeeman,
- magnetocrystalline,
- magnetoelastic,
- dipolar (shape anisotropy),
- interface (in magnetic multilayer).

In the case of $L1_0$ alloys, we can usually neglect interface and magnetoelastic energy terms with respect to the huge magnetocrystalline anisotropy or to the large dipolar energy (see later). In the case of thin FePt layers with uniaxial perpendicular chemical ordering, these approximations are realistic. For a thin film with perpendicular magnetic anisotropy, it is common to refer to the quality factor Q , defined as the ratio of the magnetocrystalline energy to the dipolar energy:

$$Q = K_u / 2\pi M_s^2 \quad (1.14)$$

If $Q > 1$ the magnetocrystalline is predominant and the magnetization is out of plane, whereas if $Q < 1$ the shape anisotropy is dominant and the magnetization lies in plane (at least in the single domain configuration [GEH99]).

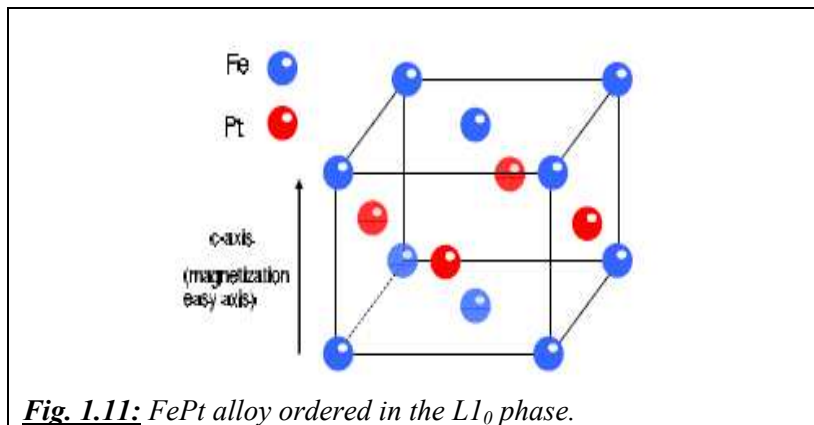
As said, one example of such materials with strong uniaxial anisotropy is found in the $L1_0$ ferromagnetic alloy. Members of that family include CoPt, FePt, FePd. Our lab has an extended experience in the growth of those alloys ([GEH97], [HAL01] and [PER07]).

The $L1_0$ structure is basically a face-centre cubic (fcc) structure with chemical ordering. It can be seen as a layered structure. Pure atomic planes of Fe alternate with pure atomic plane of Pt along the c-axis being the one along which the chemical ordering takes place, we have for FePt: $a = b = 3.85 \text{ \AA}$ and $c = 3.71 \text{ \AA}$. Obviously, chemical ordering may be partial, and the corresponding parameter is then defined as:

$$S = |n_{Fe} - n_{Pt}| \quad (1.15)$$

with n_{Fe} being the occupational rate of Fe atoms on Pt rich plane sites and n_{Pt} the occupational rate of Pt atoms on sites of this same plane. This long range chemical order parameter can be measured by X-ray diffraction (see experimental techniques). There is a link between the long range chemical order parameter and the magnetic anisotropy (see Okamoto *et al.* [OKA02], also [HAL04]), even if a detailed description should take into account the short range chemical order.

The $L1_0$ FePt layer composition ($Fe_{50}Pt_{50}$) with $K_u = 7.0 \times 10^7 \text{ erg/cm}^3$ exhibits a large uniaxial magnetic anisotropy. However, for any given materials, there is a critical grain size where thermal fluctuation becomes dominant at room temperature: for FePt, the critical diameter would be in the 3-3.5 nm range, implying a huge potential for ultra-high density data storage. A $L1_0$ FePt (001) layer in magnetic pillar is considering being a candidate as a perpendicular spin polarizer.



2 Experimental techniques and simulation used

This part described all the experimental techniques we have used to observe the results of this thesis, including the growth equipment or the method and set up of some systems to measure the characteristics of the samples.

2.1 MBE system

This section presents the experimental techniques used to grow the samples for both perpendicular and in-plane magnetization systems. Our laboratory is equipped with a Molecular Beam Epitaxy system (MBE) which is presented in Fig. 2.1.

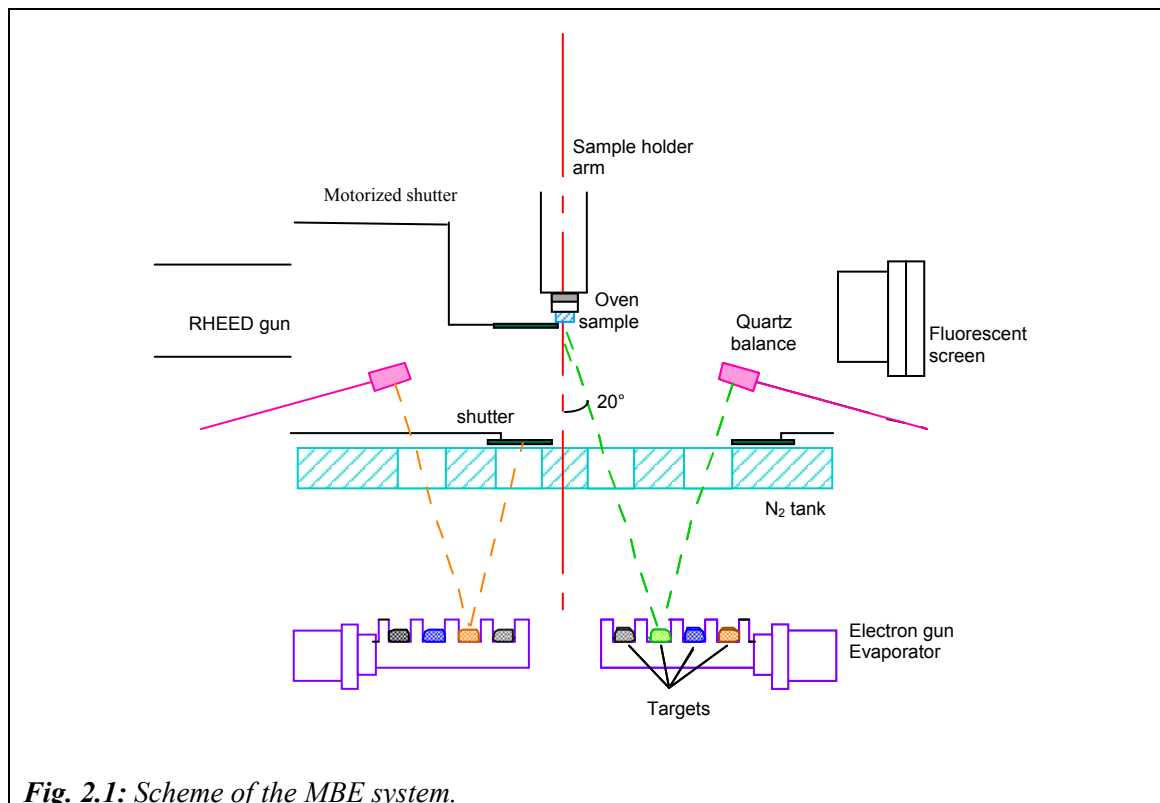


Fig. 2.1: Scheme of the MBE system.

2.1.1 Description of MBE system

Molecular beam epitaxy is a growth technique under ultra-high vacuum. It corresponds to an orientated growth over a crystal of a crystalline material, identical or more generally of a different material. Epitaxy is possible only if the two materials have close crystalline structures (in some systems, lattice rotation allows epitaxial growth in spite of strongly different lattice parameters). The requirements are on both the crystallographic symmetries and the lattice parameters. Atomic or molecular beams come from one or several sources (in the case of a co-deposition) and converge in the direction of the substrate position.

For our study, we use a RIBER epitaxy chamber dedicated to the growth of metals and oxides. The deposited elements, like iron (Fe) or platinum (Pt) are positioned in copper crucibles. An electron beam of high energy (10 keV) with a high intensity (several tens of mA) emitted by a filament located near the crucibles allows to evaporate the element one wants to deposit.

2.1.2 Description of the used chamber

The epitaxy machine used for the growths is made of several ultra-high vacuum chambers linked together. The mean pressure inside is between 10^{-9} and 10^{-10} mbar. The vacuum is obtained with the help of ionic pumps and Ti sublimator. In our system, we use 3 chambers:

The samples are introduced inside the chamber by a load-lock for quick introduction. A reasonable vacuum ($<10^{-6}$ mbar) is maintained by the primary pumping, turbo pumping and ionic pumping. Then the “molyblock” is transferred into the introduction chamber. The former is equipped with a heater to degas the substrates before the deposition. The growth of the sample is done in an evaporation chamber, as shown on Fig. 2.1.

In the evaporation chamber, the shutter can be moved by a motor during the growth to hide a part of the sample (see Fig. 2.1). This can be used to create steps or corner when the hiding part is moved in a continuous way.

During the growth, the sample is put on a sample holder located at the centre of the evaporation chamber. It has a heater to anneal the samples up to 1200°C . It can indeed increase the temperature to 500°C within 2 minutes if one wants to perform a flash annealing. As shown on Fig. 2.1, the samples are directed toward the bottom of the chamber, which implies during a growth at high temperature that the samples are only holding by the capillarity of the indium.

2.1.2.1 Description of the e-beam

The deposition chamber has two electron guns that can work at the same time. Each of them can operate four crucibles, dedicated to the evaporation of four different materials. Two shutters can quickly block the fluxes, and thus assure a precise control of the thickness of evaporated material.

2.1.3 Thickness control

We rely on two quartz balances to measure and regulate the fluxes of material. The quartz balances are positioned such as to receive the same quantity of material as the sample. The regulation of the deposition speed is done by a counter-reaction on the quartz balances: an increase in the flux will induce a decrease of the power of the electron gun.

During the growth, we use liquid nitrogen to cool the walls of the chamber: condensation on the cold walls improves the quality of the vacuum.

2.1.4 Sample cleaning

2.1.4.1 Ex-situ cleaning

The process of ex-situ cleaning for MgO substrate consists of three steps. First the MgO substrate is degreased in a bath of trichloroethylene at 300 K for 15 minutes, thereafter in a bath of acetone for 15 minutes and then in a bath of ethanol for 15 minutes also. The substrate is finally dried out with a flux of N_2 .

After drying out with nitrogen, the substrate is stuck with an indium drop on a molybdenum sample holder, called “molyblock”. This “molyblock” is introduced into the chamber.

2.1.4.2 In-situ cleaning

The substrate is annealed at 500°C for 6.5 hours to obtain a clean surface. Annealing process with different temperatures steps is illustrated by Fig. 2.2. The aim of this in-situ cleaning is to eliminate all gases like water, CO, hydrocarbon... adsorbed on the surface of the sample. It is thus essential that the temperature of the off-gassing is higher than deposit temperature (500°C in our case), in order to minimize adsorptions of chemical species coming from the “molyblock” and the furnace during the growth process.

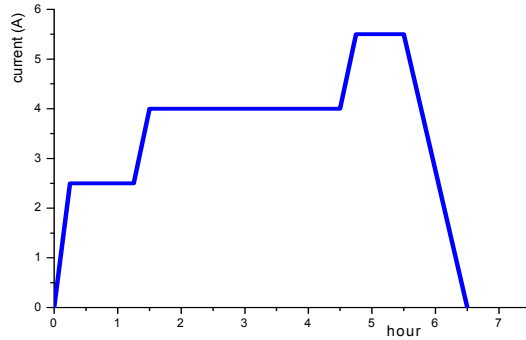


Fig. 2.2: in-situ cleaning process by heating with 5A current is considered to 550°C.

2.1.5 Substrate

Fe/MgO/Fe epitaxial structure is grown on MgO(100) substrate. The MgO substrates used for our sample is monocrystalline with cubic structure of NaCl, with atomic lattice cell $a = 4.219 \text{ \AA}$ as shown on Fig. 2.3. MgO substrate is cleaned following the process described above, before any growth is done.

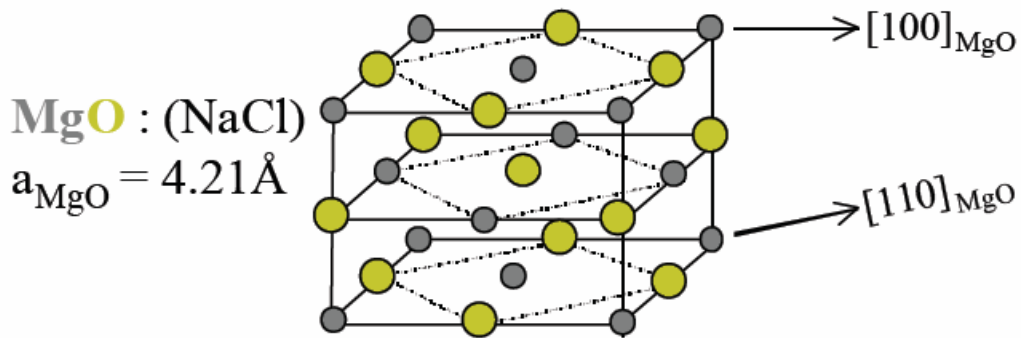


Fig. 2.3: Crystalline structure of MgO substrate.

2.2 Principle of X-Ray Diffraction

If we consider that there is an incident X-wave going directly to atomic planes (hkl) of spacing d with an incident angle ω , the X-wave will be reflected after the diffraction on atomic plane by an angle 2θ (see in Fig. 2.4). 2θ is called the diffraction angle. The diffused intensity for a crystal will correspond to the sum of the diffused waves by all the atoms of the crystal.

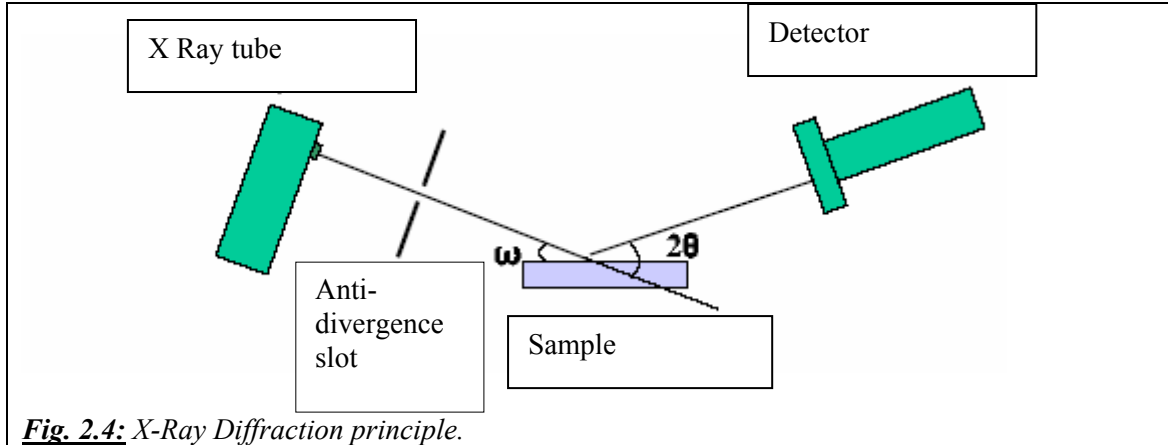


Fig. 2.4: X-Ray Diffraction principle.

The incident wave is coherent and results in diffraction picks when θ follows the Bragg law given by:

$$\lambda = 2d_{hkl} \sin(\theta) \quad (2.1)$$

h, k, l are the Miller indexes of the plane involved and d_{hkl} is the spacing between those planes, a, b, c are the lattice parameters, for a cubic structure in 3 dimension space, the spacing d_{hkl} is given by:

$$d_{hkl} = \frac{1}{\sqrt{\left(\frac{h}{a}\right)^2 + \left(\frac{k}{b}\right)^2 + \left(\frac{l}{c}\right)^2}} \quad (2.2)$$

For our experiment, we used a Philips X'Pert diffractometer system. XRD geometry is presented on Fig. 2.4. Incident beam is produced by a Cobalt cathode (radiation $\lambda_{Co-K\alpha} = 1.7890 \text{ \AA}$ and $\lambda_{Co-K\beta} = 1.6207 \text{ \AA}$). Part of this radiation is diffracted in the direction of a mobile detector.

2.3 The vibrating sample magnetometer VSM technique

The vibrating sample magnetometer was invented in 1956 by Simon Foner and nowadays, this technique is widely used in almost any magnetism laboratory.

By VSM, measurements of magnetic moments as small as 1×10^{-5} emu are possible in magnetic fields from zero to 9 Tesla (or higher) at temperature range from 2.0 to 1050 K. Powders, bulk and thin films can be measured and studied.

The principle of Vibrating Sample Magnetometer (VSM) operates on Faraday's Law of induction, which measures the changing magnetic field through an electric field. A sample of any material is placed in a uniform magnetic field, created between the poles of an electromagnet, a dipole moment will be induced, called the **magnetic stray field**. As the sample vibrates up and down, this magnetic stray field is changing as a function of time and can be sensed by a set of pick-up coils. The alternating magnetic field will cause an electric field in the pick-up coils according to Faraday's Law of induction. This current will be proportional to the magnetization of the sample. The greater the magnetization is, the greater the induced current. So, the sample vibrates along the Z axis perpendicular to the magnetizing field.

2.4 Magneto – optical effect

As we relied on a Magneto–Optical Kerr effect system (MOKE) to perform the demagnetizing experiments, we now introduce the principle of Magneto-Optical Kerr Effect and describe the MOKE set-up we used. MOKE is particularly important in the study of ferromagnetic and ferromagnetic films and materials, and exhibits specific advantages for our study, as described below.

The first observation of the modification of the light polarization state by a magnetized metallic iron mirror was done by John Kerr in 1877. He found that this Magneto-Optical effect in reflection was proportional to the sample magnetization M [HAM03].

Nowadays, MOKE is widely used as a tool to investigate how the magnetization state depends on field in ferromagnetic samples. MOKE has indeed some advantages with respect to other techniques:

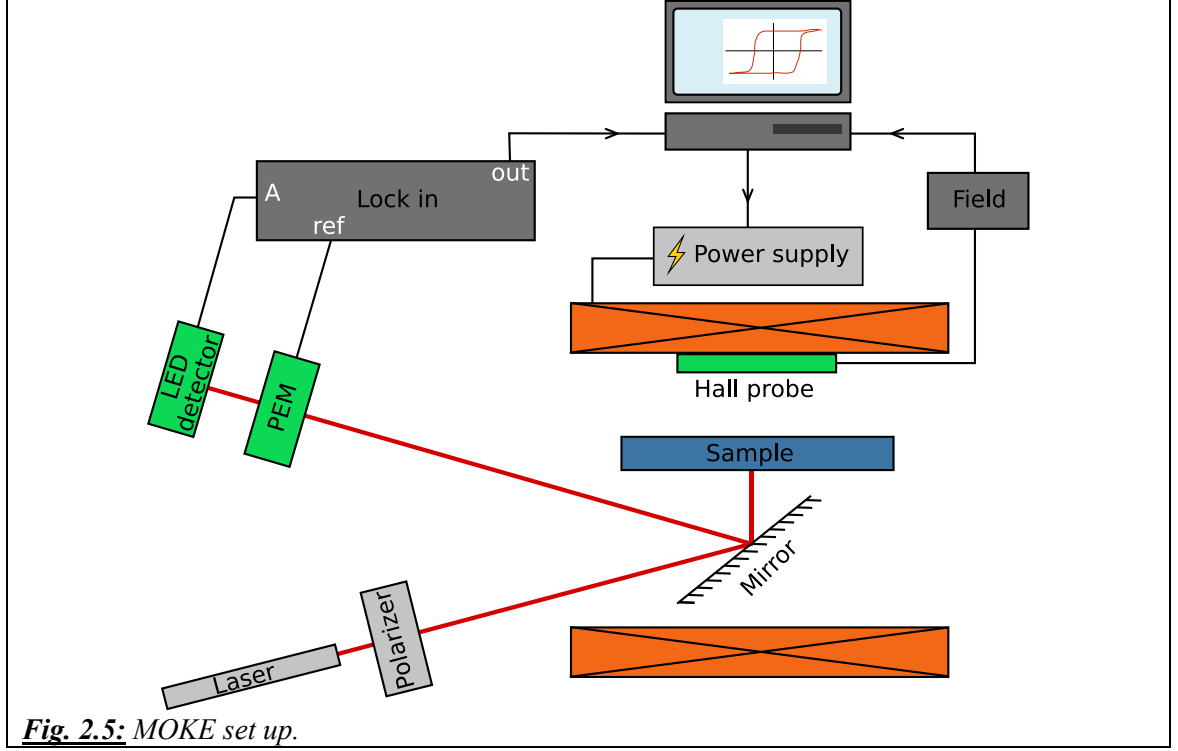
- It is a very sensitive technique that can compete with the best SQUID magnetometry, especially to study the magnetism of ultrathin films. It can detect the magnetization of a fraction of Atomic Layer (AL) of the FM material.
- It can be a very fast method and the short duration of the light/matter interaction allows time resolved measurements of the magnetization.
- It is depth sensitive (approximately 30 nm) and thus, in principle, can probe the magnetic state of several FM layers in a multilayer structure. However it is difficult to separate the contribution of each layer.
- Especially, for the cycling of the soft layer with around 1000 cycles, we need a very fast method. In our system, when performing a 1000 cycles experiment cycling between $\pm 2.0\text{KOe}$, it takes less than 24 hours, while other methods take several days.
- It is insensitive to (non magnetic) substrates.

Principles and set –up of MOKE

The Magneto-Optic Kerr Effect (MOKE) exploits the changes in reflection of polarized light on a magnetic sample. This reflection can produce several effects, including:

- Rotation of the direction of polarization of the light
- Introduction of ellipticity in the reflected beam
- A change in the intensity of the reflected beam.

Polar MOKE is most frequently studied at near-normal angles of incidence and normal to the reflecting surface. A practical reason is that it is convenient to have both beams (incoming and reflected) going through a hole in one pole of the magnet.



As can be seen from Fig. 2.5, the light from the He/Ne laser is vertically polarized by a polarizer. When the beam reflects on a ferromagnetic layer, the polarization becomes elliptical and rotates by a small angle. This is the Kerr effect. Angle of rotation and ellipticity of the beam are proportional to the magnetization of the sample.

The sample is mounted on a rotatable sample holder, inside the field. In **the longitudinal MOKE**, the magnetization vector is parallel to both the reflection surface and the plane of incidence while, for **transversal MOKE**, the magnetization is perpendicular to the plane of incidence and parallel to the surface.

Fig. 2.5 shows our experimental setup. The photo-elastic modulator (PEM) modulates the light at 50 kHz to increase the sensitivity of the set-up. It also allows us to record both the ellipticity and rotation of the reflected beam. A photodiode transform the optical signal into an electrical one that is transmitted to a lock-in amplifier. The output of the lock-in is then transmitted to a computer for recording the measurement. This computer also drives the electro-magnet.

The operation of this system may be analyzed using Mueller matrices and Fourier series. The Kerr rotation angle θ_k and the Kerr ellipticity ϵ_k are typically very small numbers; therefore small angle approximations may be used. We can record both ellipticity and angle signal with the help of the PEM. The intensity of light (as a function of time) arriving at the detector is calculated:

$$I(t) = I_0[1 + 2\theta \cos(A_0\omega t) - 2\epsilon_k \sin(A_0\omega t)] \quad (2.3)$$

where I_0 represents the “average” or DC intensity, $\omega = 2\pi/f$ is the angular frequency of the PEM oscillations and A_0 , the retardation amplitude of the PEM. Using a Fourier series expansion to represent this equation and keeping only the first three terms:

$$I(t) = I_0[1 + 2\theta_k J_0(A_0) - 4\epsilon_k J_1(A_0) \sin(\omega t) + 4\theta_k J_2(A_0) \cos(2\omega t)] \quad (2.4)$$

The second term is part of the DC term and may be neglected for either or both of two reasons: 1) θ_k is a very small number and/or 2) $A_0 = 2.405$ radians, in which case $J_0 = 0$. Three voltages are measured: V_{DC} , V_{1f} and V_{2f} . It is traditional to form the ratios of the AC term to the DC term, since by doing so the experiment becomes immune to fluctuations in the light intensity, changes in transmission, etc. Thus:

$$\theta_k = \frac{\sqrt{2}}{4J_2} \frac{V_{2f}}{V_{DC}} \quad (2.5) \quad \text{and} \quad \varepsilon_k = \frac{\sqrt{2}}{4J_1} \frac{V_{1f}}{V_{DC}} \quad (2.6)$$

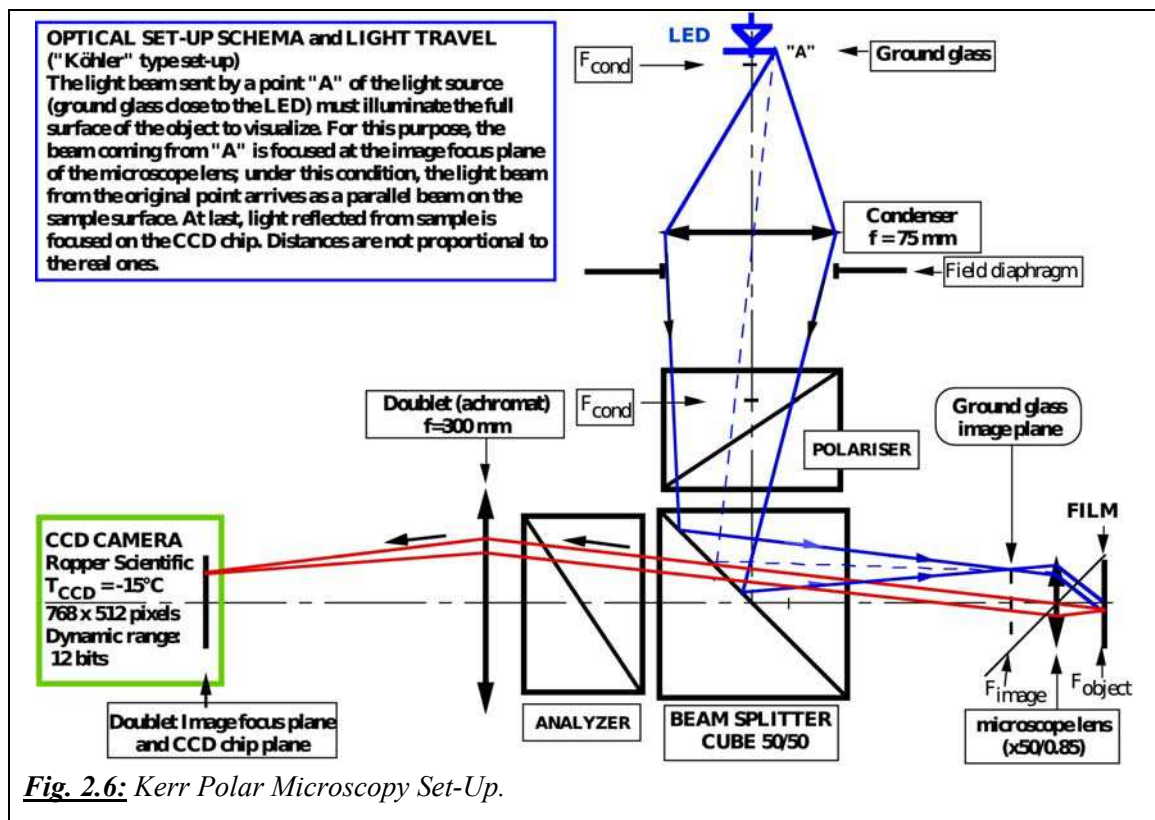
The factor $\sqrt{2}$ arises since lock-in amplifiers display the rms voltage, whereas the theory is written in terms of peak voltage or voltage amplitude.

With the help of the PEM we can record either the Kerr ellipticity or the Kerr angle. Because we are not strictly in a polar geometry, it is somehow difficult to correctly record the two signals at the same time. Some spurious effects induce by a mixing of the polarization during the reflection of the beam on the mirror and the sample gives rise to hysteresis loop that are difficult to interpret.

2.5 Kerr polar Microscopy MOKE

2.5.1 Polar Kerr Microscopy Set-Up (in LPS)

The set-up is inside an optically opaque box localized on a granite optical table (Fig. 2.6). The table is inside a thermally regulated box to avoid thermal drift of the sample ($T = \text{setting} \pm 50$ mK over more than one day) during optical image acquisition. The set-up is optimized to work as a polar Kerr microscope, *i.e.* when the magnetization has a component perpendicular to the sample plane: for this reason, it used linearly polarized light. It relies on a powerful and very stable solid-state continuous light source: a light emitting diode (LED). The emission wavelength is 505 nm with a bandwidth of 40 nm. To decrease the non homogeneity of the LED emitting surface, a ground glass is placed very closely in front of it and this glass behaves as a secondary emission source.



The illumination of the sample is Köhler-type as in a standard microscope, *i.e.* the light source image is formed in the image focus plane of the microscope lens; in this way, each point of the light source illuminates the whole, but field limited, sample surface (the optical intensity decreases by about 15% on the edge of the optical image). Polarizer and analyzer are high grade Glan-Thomson calcite prisms. The beam splitter (non polarizing cube) is a 50/50 type (the transmitted and reflected light powers represent each of them close to one half of the incident power). The microscope lens (Olympus) was chosen to have no stress to avoid undesirable birefringence effect; it has a x50 magnification and a 0.85 numerical aperture. An $f = 300 \text{ mm}$ lens projects the sample image on the cooled (-15°C) CCD chip of the camera, so that each square pixel of the CCD chip represents a $0.106 \mu\text{m} \times 0.106 \mu\text{m}$ square surface of the sample and the field of view on the sample is close to $80 \mu\text{m} \times 50 \mu\text{m}$. The resolution is around $0.45 \mu\text{m}$. Polarizer and analyzer are uncrossed by 9° ; this angle value represents a good compromise between the necessary linear detection of the Kerr rotation (small in our samples), a reasonable small time of exposure (of the order of some seconds at maximum per image) and a not too large continuous component of the light intensity, which otherwise would deplete the signal/noise of optical images. A computer receives images (772 Ko), stores them and allows us to process them. Accumulation of several images and their summation are sometimes necessary to improve the signal/noise ratio in case of a small Kerr rotation.

2.5.2 Magnetic Field Pulse Generation

The sample is glued on a sample holder at the centre of the gap of an electromagnet. The electromagnet has polar pieces with 25 mm diameter axial holes to allow light going through it. A calibrated Hall probe placed in the middle of the gap, measures the continuous magnetic field very close to the sample. The electromagnet field is generated by a symmetric power supply

giving ± 2.4 kOe (0.24 Tesla) at maximum. The field value is adjusted either manually or with a LabView program (author: V. Klein) driven by the computer. A fine adjustment of the field can be done manually to within ± 0.02 Oe (± 2 μ T). Furthermore, for short duration but large amplitude field pulses, a very small coil (VSC) attached to the sample holder has been designed; it is in physical (but not electrical) contact with the sample surface. The VSC is typically done with 4 isolated copper wire turns (1.6 mm inner diameter) and is driven by a laboratory made pulse generator delivering current pulses as high as $I = 80$ A (1.7 kOe or 0.17 T) during $t = 50$ to 2,000 ns; the main limitation is a drift of the sample temperature itself; in practice, the parameters (I and t) were not allowed to induce more than $T = 0.2^\circ\text{C}$ temperature increase. This last value was calculated in an adiabatic regime, at the end of the experimental pulse. Furthermore, a larger coil (LC) is used in the intermediate regime of fields between the VSC and the electromagnet; it can generate much longer pulses ($10\text{ }\mu\text{s} < t < 1\text{ s}$). The VSC design could have been smaller; nevertheless, one must keep in mind that precise measurements on the position of the domain walls ask for field homogeneity and so for sufficiently large bore coils.

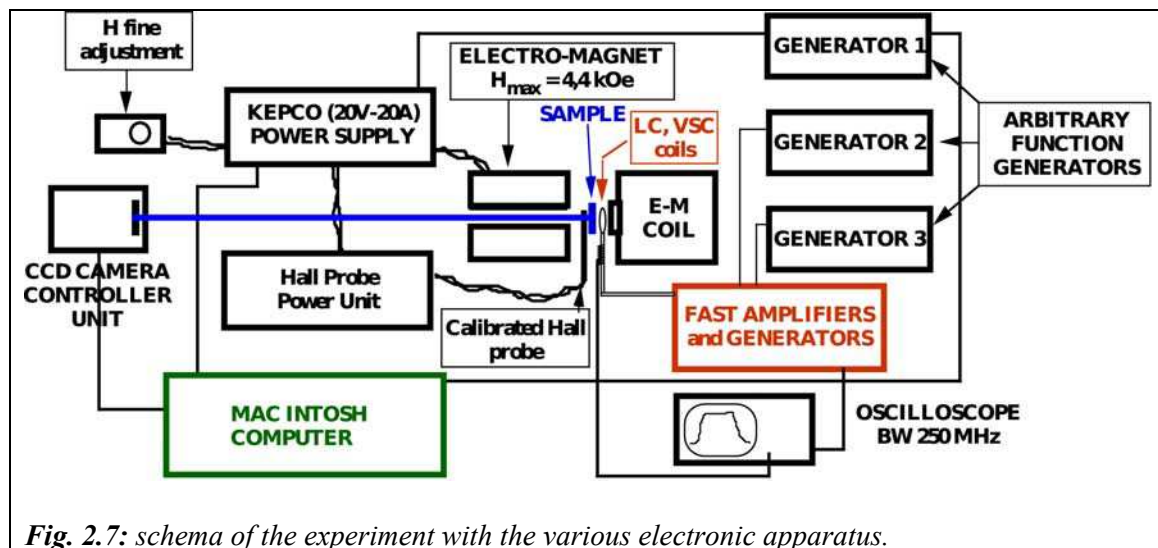


Fig. 2.7: *schema of the experiment with the various electronic apparatus.*

The Fig. 2.7 above displays the electronic schema of the experiment with the various electronic apparatus. The electromagnet has a large diameter bore to leave the optical beam to go through. Pulse generators either commercial or IEF made send current pulses into the coils and are designed for 0.5 to 1 Ohm impedance load; so, CMS resistors are in series with these coils to keep this characteristic impedance and to measure pulse shape with a large bandwidth oscilloscope. Coil generator links are done with laboratory made flat cables. In this way, one gets rather flat field plateau ($\pm 2\%$) with no overshoot. The shape of the current pulses (proportional to the field pulses) is controlled by a large bandwidth (500 Mhz) oscilloscope, by picking up the voltage on CMS resistors in series and very close to coils.

In this way, with the VSC, the LC and the electromagnet, a very large time scale is swept, from about 50 ns up to 1 hour or several days, depending on the necessary field amplitude. This allows magnetization dynamics studies on 12 decades of time, while field amplitude can be continuously varied from 10^{-4} T up to 0.4 T.



Fig. 2.8: the Sample holder.

In the Fig. 2.8 above, the sample holder has fine X, Y adjustments. The Very Small Coil and the Large Coil are visible. The sample is not present on this picture the width of which is about 15 cm. The copper plates on the left are the copper strip lines bringing the current pulses to the coils. The small black rectangles are CMS resistors.

2.5.3 Recording Magneto-optical Images

Usually, optical images barely allow to detect magnetic domains if there are, because the magneto-optical Kerr rotation is small and it gives a small contribution compared to the optical contribution of the sample. To get a better signal to noise ratio of the magneto-optical information, it is necessary to remove the optical contribution. It is easy to do so just by subtracting the images obtained usually under different field conditions, using the IPLab application present in the computer and built for the CCD camera. One image is taken for example after saturation with a negative field pulse (uniform magnetization M_-) and the second one after a positive field pulse leaving a magnetic domain with positive magnetization or a uniform positive magnetization (M_+). If the signal/noise ratio is not sufficient, it is necessary to accumulate more images for each magnetic state, sum these images and then use the difference between the two sums. One can also try to compensate for the intrinsic lack of uniformity of the optical images, due to non uniform illumination.

The noise or undesirable contributions present in the magneto-optical images results from several origins. Some of them can be removed by more or less simple tricks, some others cannot be. One of the latter ones is related to the photon statistics; the signal is proportional to the number N of photons and the noise varies as $N^{1/2}$, so that $S/N = N^{1/2}$. To extract the magneto-optical image, a difference is done between two optical images and then $S/N = 2N^{1/2}$. To improve this ratio, the solution is to increase the N value, by using more images: 64 images of both states will improve S/N by a $64^{1/2} = 8$. For example, in Pt (60 nm) / FePt (5 nm) / MgO (3 nm) / FePt (10 nm) / Pt (9 nm) structure, reflected optical image intensity is $I_{im} = 2.8 \times 10^4$ with 8 accumulations for each magnetic state and the difference between these oppositely

saturated states, *i.e.* the Kerr contribution, is $I_{\text{Kerr}} = 4 \times 10^2$ in the same area (*i.e.* $I_{\text{Kerr}}/I_{\text{im}} = 1.4 \times 10^{-2}$). The ratio S/N is then sufficient in this continuous film for domain wall dynamics study.

Other sources of non statistical noises, which can be at least partly compensated, are:

- The presence of an electronic offset coming from the camera circuits: the difference between optical images cancels it.
- The CCD chip dark noise; it can be reduced by lowering CCD temperature and reducing the time of exposure t . This noise effect is doubled in the optical difference.
- The conversion rate of each pixel of the CCD chip, which is pixel dependent but is a constant for a constant chip temperature T . The difference between optical images reduces strongly its effect.
- The 20% intensity decrease on the CCD edge as compared to centre, due to the light beam arriving on the CCD; it can be easily compensated by a mathematical procedure,
- The temperature gradient over the CCD chip surface due to the CCD cooling; it is also compensated by the previous mathematical procedure.

2.5.4 Optical resolution and magneto-optical contrast

The optical contrast is determined by the light wavelength and optical aperture of the microscope lens. Its value is of order of 400 nm. It is sufficient for velocity studies but can be a limitation for short scale studies as domain wall roughness, for example. It is also a limitation for study of small entities dynamics, as soon as their geometric dimensions are smaller than the optical wavelength.

2.5.5 Experimental method to study domain wall velocity

All the MOKE measurements reported in this chapter were also performed at the Laboratoire de Physique des Solides at Orsay University in the team of Professor J. Ferré with the help of Dr J.-P. Jamet. We used polar magneto-optic Kerr effect (PMOKE), as when observing domain wall patterns. The measurement consists in taking two frozen images at remanence of a rather flat domain wall domain before and after the application of a field pulse of a known duration. These images are then subtracted from each other to evidence by difference the wall displacement. The wall velocity can then be extracted by a linear plot of the domain wall displacement versus the pulse duration [MET07]. Obviously, it has been checked that the domain structure is stable in zero field conditions during imaging.

Due to the subtraction process and the linear plot, effects from the transient parts of the pulses are eliminated. As the domain wall speed varies over order of magnitude, magnetic fields were applied over times ranging from ≈ 150 ns to 40 min, chosen such that the displacement could be reliably determined and the wall remained within the size range of one image ($54 \mu\text{m} \times 48.6 \mu\text{m}$).

The applied field must be kept small enough to avoid secondary nucleation events, so that wall propagation is the dominant reversal process. Generally speaking, this restricts the observable field range to values far below the theoretical nucleation field deduced from the anisotropy. Indeed, a nucleation event occurs on defect sites where the energy barrier preventing nucleation is reduced. In our case, the high quality of the samples results in such a low density of nucleation sites that it is possible to observe the flow motion regime over a large range of fields.

2.6 Simulation method for domain wall motion with perpendicular magnetization

The purpose of this simulation is calculating the magnetization \mathbf{M} at each point of the “sample”, then calculating the position of domain wall and finally finding the domain wall velocity as a function of applied field.

In this simulation model, we simulate in a perfect system with perpendicular magnetocrystalline anisotropy. By “perfect system”, we mean that no structural or magnetic defects are introduced. Also, the influence of thermal effect also is neglected.

The simulation modeling of domain wall motion is based on the dynamic Landau – Lifchitz – Gilbert (LLG) equation. This equation is modified for magnetization configuration with spontaneous magnetization \mathbf{m} . It can be written as:

$$\frac{d\mathbf{m}}{dt} = -\gamma\mu_0\mathbf{m} \times \mathbf{H}_{\text{eff}}, \quad (2.7)$$

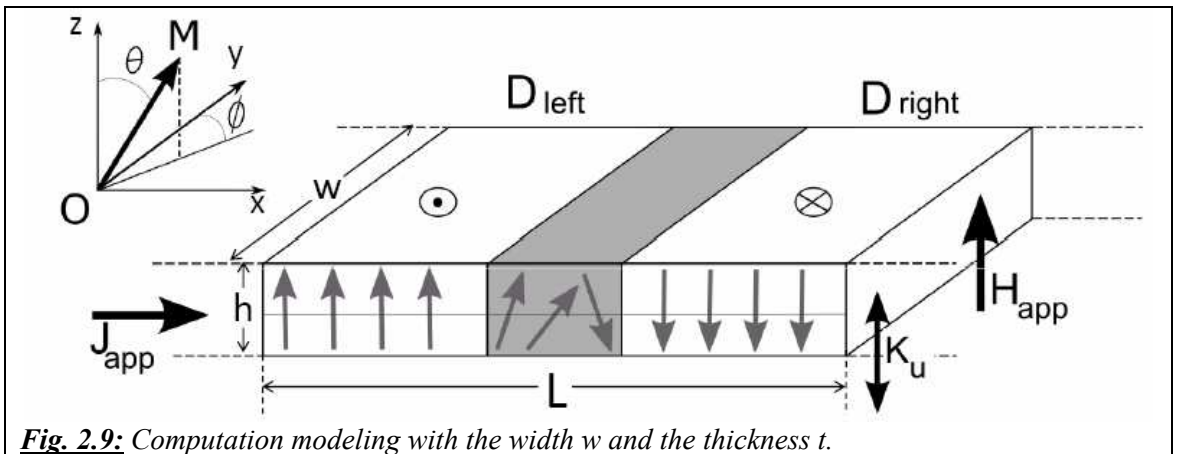
with $\mathbf{H}_{\text{eff}} = \mathbf{H} + \alpha\mathbf{m} \times \mathbf{H}$,

where α is the Gilbert damping factor and γ is gyromagnetic ratio. The field \mathbf{H} is the sum of several contributions: exchange field H_{ex} , magnetostatic anisotropy field H_{anis} , dipolar field H_{dip} and externally applied H_{app} .

The evolution of \mathbf{m} turning around the vector field \mathbf{H}_{eff} , governed by equation (2.7), is then described by:

$$\mathbf{m}(t + \delta t) = \mathbf{m}(t) \cos(H_{\text{eff}}\delta t) + \frac{\sin(H_{\text{eff}}\delta t)}{H_{\text{eff}}} (\mathbf{H}_{\text{eff}} \times \mathbf{m}(t)) + (1 - \cos(H_{\text{eff}}\delta t)) \frac{H_{\text{eff}} \cdot \mathbf{m}(t)}{H_{\text{eff}}^2} \mathbf{H}_{\text{eff}} \quad (2.8)$$

The relation tends to an exact integration of the LLG while the variation of the effective field H_{eff} remains weak during the length of time δt . The configuration is well adapted to be simulated by a rectangular box with a constant length (Ox direction), a variable width (Oy direction) and height (Oz direction), shown in Fig. 2.9. The symmetry properties allow reducing the domain of calculation to a finite size 2D box for one unique period P of the width w and the layer thickness t .



Beside that, the domain wall can be defined as a region where the angle θ goes from 0° (D_{left}) to 180° (D_{right}). ϕ is the angle of the wall with easy plane. If ϕ is zero the wall is of Bloch type and when $\phi = 90^\circ$ the wall is of Néel type.

Under applied field, as we reported before, domain wall velocity can be observed in two motion regimes, separated by a Walker breakdown which is related to the magnetization by $\mathbf{H}_w = 2\pi\alpha\mathbf{M}_s$. In each regime, the domain motion behavior as well as domain position are different. Simulating this is the main work in this part.

- In the steady regime, at the beginning of the motion, the applied field tilts the magnetization away from its original position and the M_x magnetization component takes non-zero value. The domain wall accelerates until equilibrium between the torques is reached, M_x reached its maximum (see chapter on domain wall velocity theory (1.1.3.1)). After this, the motion occurs by translation at constant velocity, while the domain wall has a mixed Bloch – Néel structure. By increasing the external field, the moments in the wall tilt more and more perpendicularly to the wall plane, the maximal inclination (ϕ_{max}) in this regime being 45° . The change of the angle ϕ affects the domain width Δ , namely the wall becomes narrower.
- In the precessional regime, both the wall position and the wall velocity have an oscillatory behavior: the wall goes back and forth, following the direction of magnetostatic field, while the wall velocity attains both positive and negative value. The oscillation frequency increases with the value of applied field. In this regime, ϕ goes periodically from 0° to 360° . The structure of the domain wall changes accordingly: for $\phi = 0^\circ$ and 180° the wall is pure the Bloch type and for $\phi = 90^\circ$ and 270° the wall become pure Néel type. The velocity is zero when the wall is either pure Bloch or pure Néel type. When transiting between the two structures type, the velocity evolves either towards a maximum or a minimum value. The oscillation period of the angle ϕ was determined to be twice the oscillation period of wall velocity.

3 Growth, structural and magnetic characterizations

3.1 Growth process

Because the high magnetic anisotropy in FePt $L1_0$ phase originates from the magneto crystalline anisotropy, in which the c -axis direction is the easy-axis, a random distribution of the crystallographic axes would lead to a very low resultant magnetic anisotropy in the film. Therefore, it is very important to engineer the crystallographic orientation of $L1_0$ ordered thin film so that the easy-axis (c -axis) can be established in the desired direction, *e.g.* along the film normal for perpendicular magnetic recording.

Pierre de Person [PER 07] discussed in great details the growth and the structure of ordered FePt single layer and FePt based MTJ. In this part, we just summarize some important results of the growth process of FePt. Further details are provided in [PER 07]. Beside that, FePt single layer sample is grown by the same process as the soft layer of FePt/MgO/FePt MTJ. Therefore we report also the growth of FePt single sample inside the part concerning MTJ growth.

The structure of FePt used for our experiment is presented in Fig. 3.1. We use **Molecular Beam Epitaxy** (MBE) to grow sample with very high vacuum $P \approx 10^{-9}$ mbar during the deposition.

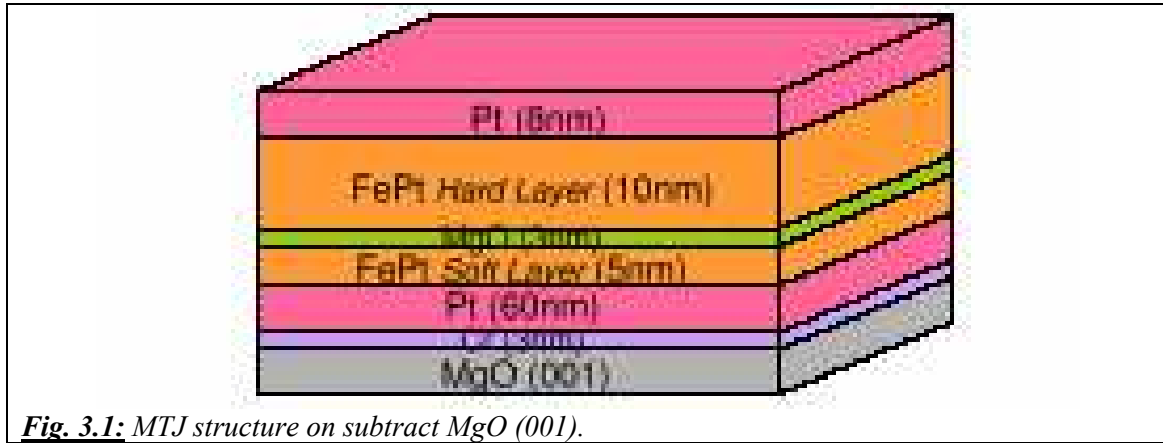


Fig. 3.1: MTJ structure on substrate MgO (001).

3.1.1 Description of the growth of each layer

This structure grows on MgO substrate with (100) direction. During the growth, all the layers keep the same growing direction (100) as MgO substrate.

First of all, on MgO substrate [100], the Cr grows at [110] direction, it means the Cr axes must be turned 45° with respect to MgO corresponding axes. By that way, the lattice cell of Cr is calculated by $a_{Cr} \sqrt{2} = \sqrt{2} \times 2.88 = 4.08 \text{ \AA}$. This value is fixed to the MgO lattice parameter 4.21 \AA . The next Pt layer follow the same growing rule than the Cr on MgO: the lattice constant of every growing layer is taken to be a factor of $\sqrt{2}$ larger than the one of the layer below, the cubic of growing layer is always turned 45° to the layer than the cubic of layer below; therefore the two layers with different material can be matched epitaxially. However, the FePt bottom electrode, MgO and FePt top electrode grow directly on the layer below, keep the [100] direction as MgO substrate.

3.1.2 Growing conditions

The first Cr layer 3 nm is grown at room temperature and a speed of $v = 1 \text{ \AA/s}$. The second layer Pt 60 nm is grown with the same condition and then annealed at 500°C to smooth the surface. The thicknesses are monitored by quartz balances during all the process. Reflection High Energy Electron Diffraction (RHEED) is used to control the growing surface in-situ during the annealing. Practically, we follow the RHEED images until the Pt surface shows sign of good crystalline quality and flatness. This corresponds to a RHEED pattern where dots have disappeared and where thin and long lines are observed (Fig. 3.2). After that, the temperature is decreased to room temperature for the next step.

After RHEED images showed good crystalline and flatness of the Pt(001), a 5 nm thick FePt layer was epitaxially grown by co-deposition of Fe and Pt at $T = 500^\circ\text{C}$. The typical growth rate was 0.5 \AA/s . Stoichiometry ($\text{Fe}_{50}\text{Pt}_{50}$) and thickness were controlled by two quartz balances. As the substrate temperature is increased, the streaks become thinner and are more clearly defined. The bottom layer always has a good crystalline structure because it is grown on a very smooth buffer surface of Pt.

A MgO(001) layer was then epitaxially grown, also by electron beam evaporation, the MgO source being made from crushed stoichiometric MgO monocrystalline substrates (a high purity material). The MgO barrier is a key and delicate step in the growth process. In order to obtain good crystallinity, the tunnel barrier was grown in two steps. First, 6 \AA were deposited at room temperature at a speed of 1.5 \AA/s . This produced a RHEED pattern with broad and quite diffuse streaks. The samples were then annealed at 500°C for a few minutes. As the substrate temperature increased, the streaks became thinner and were more clearly defined. Then the remaining part of the layer was grown with a rate of 0.5 \AA/s . MgO films grown on FePt(001) layer have a cube on cube epitaxy relation $(001)_{\text{MgO}} // (001)_{\text{FePt}}, [110]_{\text{MgO}} // [110]_{\text{FePt}}$.

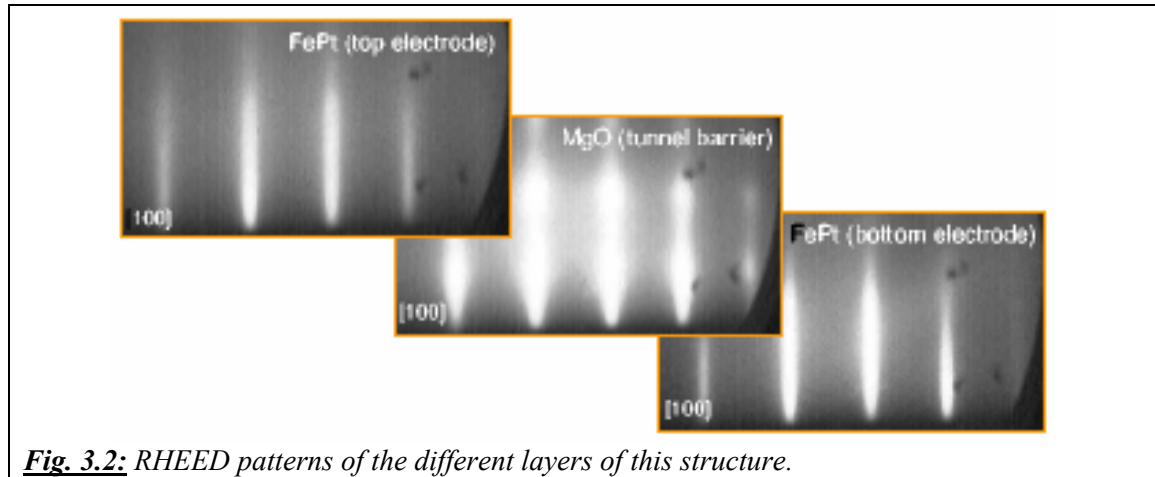


Fig. 3.2: RHEED patterns of the different layers of this structure.

The top FePt(001) electrode (10 nm thick) was then epitaxially grown on the thin MgO (001) layer, in two steps also: a 20 \AA layer was first grown by alternate mono-atomic layer deposition. Mono-atomic layers of Fe and Pt were deposited alternatively (6 times repetition) with a substrate temperature kept at 170°C . Then the sample was annealed at 500°C until obtaining of a good RHEED pattern. The growth of the remaining part (80 \AA) of the FePt layer was next performed at $T = 500^\circ\text{C}$ by co-deposition of both elements. Experimentally, it is difficult to grow a barrier with a perfectly smooth MgO surface (see RHEED image of MgO barrier on Fig.

3.2). Thus, the Fe top layer exhibits somewhat different properties than the bottom layer: it becomes naturally the hard magnetic layer.

This procedure was necessary to initiate a $L1_0$ ordering of the top FePt electrode with a c-axis only along the [001] direction, and to achieve an optimum long range order parameter. RHEED patterns for the [100] azimuth of the successively deposited layers are also shown in Fig. 3.1. As such a procedure is not required on MgO monocrystalline substrates; it is likely that the need to start with layer by layer growth is associated with a higher roughness of the MgO barrier (with respect to the surface of the MgO monocrystal).

Finally, a 30 Å thick Pt protective layer was deposited at room temperature.

3.2 Structural characterizations

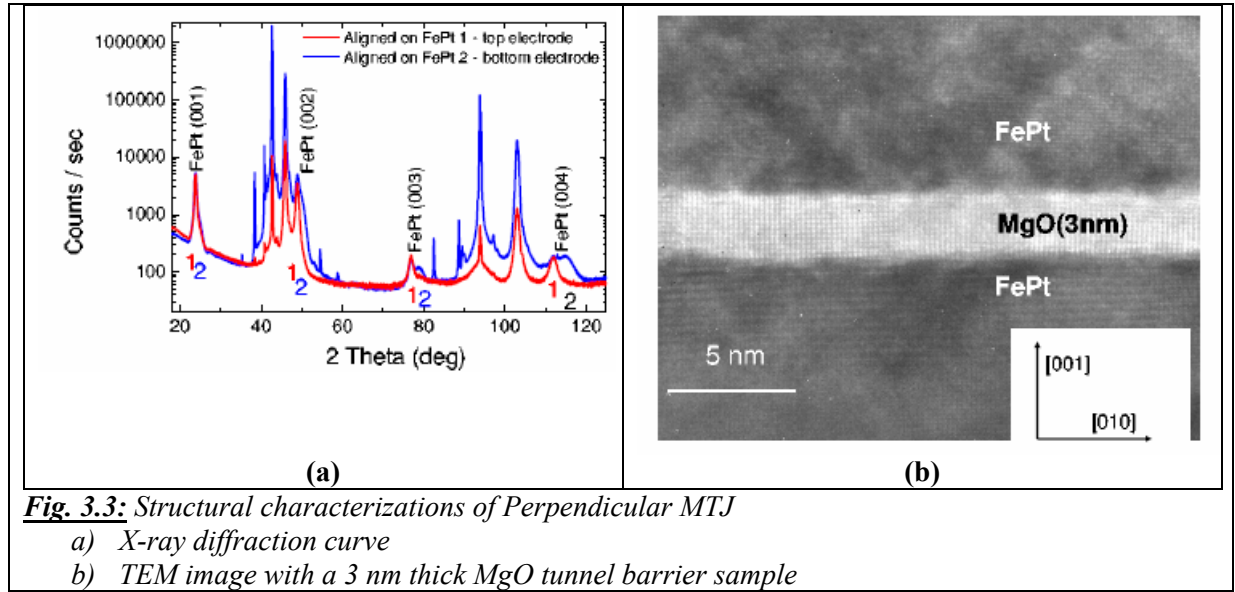
X-ray diffraction (XRD) studies with Co $K\alpha$ radiation were performed for structural characterizations, and revealed good structural coherence and high long range order for each of our two electrodes.

Fig. 3.3a shows the Bragg scan of our sample. In addition to the fundamental (002) and (004) peaks associated with the tetragonal structure of FePt, the superlattice FePt (001) and (003) peaks associated with the $L1_0$ ordered structure can clearly be observed. The pattern shows strong FePt (001) and (003) peaks indicating high long-range order parameters.

In spite of a strong overlap of the (001) (or (002)) peaks associated with the two FePt layers, two (003) (or (004)) peaks are well defined. These two peaks correspond to the two ferromagnetic layers. It has then be possible to determine the respective perpendicular lattice parameters and to fit with two contributions the broad (001) and (002) observed peaks.

The bottom electrode has a lattice parameters of $c = 3.63$ Å (perpendicular) and $a = 3.92$ Å (in plane) whereas the top electrode has lattice parameters of $c = 3.71$ Å and $a = 3.86$ Å. These latter parameters are closer to the bulk $L1_0$ FePt values (3.71 Å and 3.85 Å, respectively [JCP99]).

These results indicate that the bottom ferromagnetic electrode grows pseudomorphically strained on the Pt buffer layer (in-plane lattice parameter 3.92 Å). Conversely, the top FePt electrode grows fully relaxed. From the width of the FePt(001) Bragg peaks we could determine the chemical coherence length along the surface normal to be ~ 50 Å and ~ 100 Å. These values are similar to the thickness of the films (as expected).



The microstructure of the film was observed by transmission electron microscopy (TEM) using a 400 keV electron microscope with a resolution of 0.14 nm. Fig. 3.3b shows a cross-sectional TEM image. The high-resolution electron microscopy image shows the very good morphology of our structure, with a relatively smooth, reasonably flat and well defined tunnel barrier. No pinholes could be detected on 150 nm wide images. The MgO barrier does not exhibit significant fluctuations of its thickness.

3.2.1 Anisotropy of FePt thin film

In order to study the variation of the anisotropy with FePt thickness, we measure the hysteresis loop by superconducting quantum interference device (SQUID) magnetometer which support to measure at high field. The measurements have been performed for FePt with thicknesses of 2 and 4 nm. We measure the hysteresis loop with the field applied in two directions: perpendicular and parallel to the film. We have then subtracted the in-plane curve from the perpendicular curve. The result of this subtraction is the curve in yellow on Fig. 3.4. This operation is necessary to eliminate the diamagnetism of the MgO substrate that is very strong. Theoretically we can then deduce the anisotropy field by computing the field at which the high field slope of the yellow curve crosses the line $M = 0$.

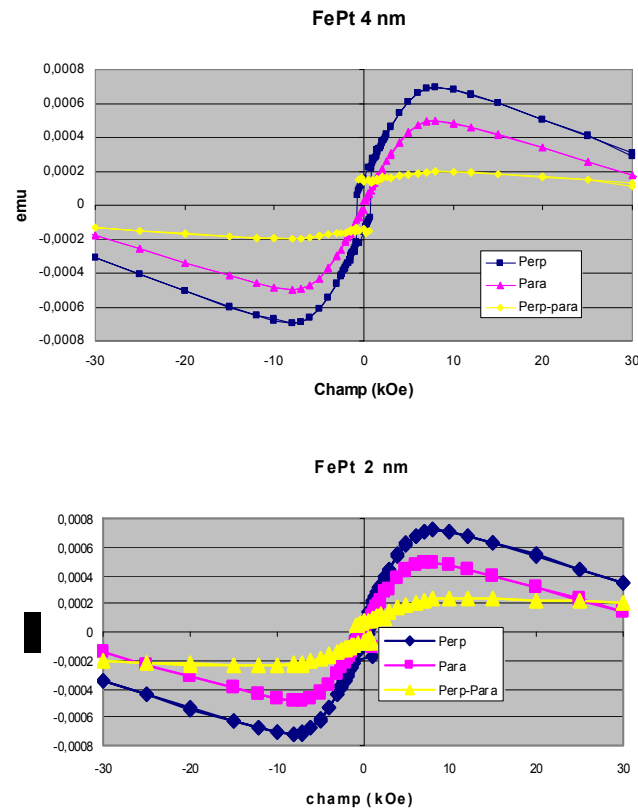


Fig. 3.4: Hysteresis loop out of plane, in plane and difference of the two curves for 4 nm (a) and 2 nm (b) FePt thin film.

Fig. 3.4a and b show the magnetization curves at RT for the 2 and 4 nm FePt thin film grown by epitaxy at the same condition. The dark blue curve presents the result with applied field perpendicular to the film while the pink one presents the result with applied field parallel to the film. The difference between the two curves is presented in the yellow curve and gives us the idea of anisotropy. Though this method may introduce some uncertainty, it is meant as a way to check that the investigated layers indeed exhibit very large magnetic anisotropies as expected for well and uniaxially ordered FePt alloys. For both results, a strong perpendicular anisotropy is indeed obtained. The values of magnetization at saturation M_s for the 4 nm and 2 nm thick sample are $M_s = 1304 \text{ emu/cm}^3$ and 1309 emu/cm^3 , respectively. It is obtained by taking the measured value of the magnetization at zero field because our FePt sample are 100 % remanent. This hypothesis has been checked on these samples by polar MOKE with a maximum applied field of 1.5 T.

3.2.2 Magnetic characterizations

For FePt single sample:

The structure of our sample, grown by molecular beam epitaxy, is:

MgO(100)/Cr(3 nm)/Pt(60 nm)/FePt(x nm)/MgO(3 nm)/Pt(4 nm)

with $x = 2, 4, 5$ or 6 nm .

The Kerr hysteresis loop with perpendicular applied field is shown in Fig. 3.5.

The purpose of this study is to carefully understand the behaviors of the domains when the thickness of the sample is increased. As said, this is a new range of observations opened by the bulk origin of the FePt anisotropy. Therefore, we also study the velocity of the domain wall as function of field with different thickness of FePt.

We can see on Fig. 3.5a, b, d, as expected, that the loops are very square, symmetric and the coercive field is ≈ 0.85 kOe, and the saturation field is larger than 1.6 kOe. However, this conclusion is not applied for the sample FePt $t = 5$ nm (fig.c) because it is not grown in the same growth run as the other films. The coercive field for the case FePt $t = 5$ nm is about 1.5 kOe.

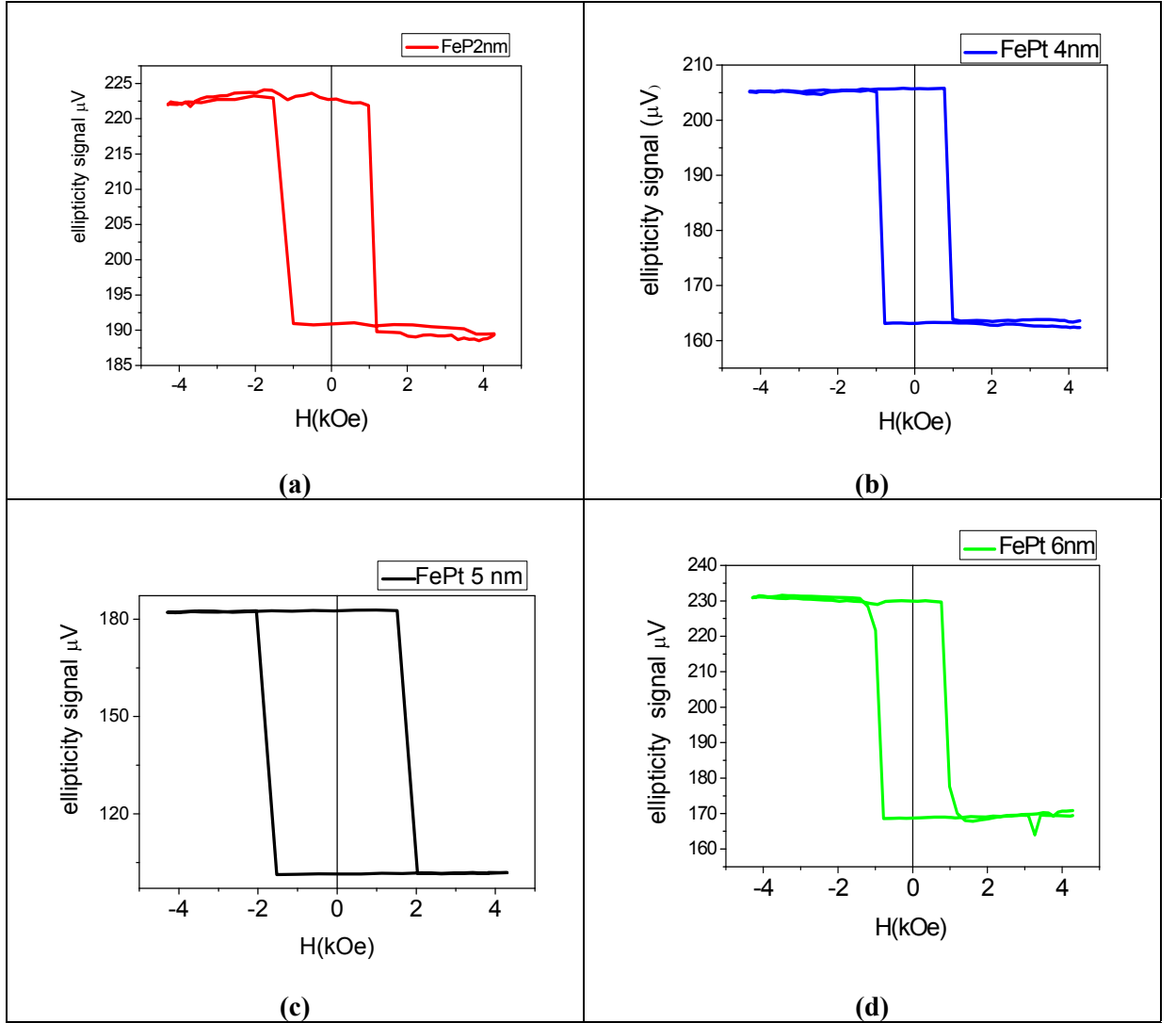


Fig. 3.5: Hysteresis loops of FePt layers with different thickness, measured by Kerr Polar effect under the perpendicular applied field.

(a) $t = 2$ nm

(b) $t = 4$ nm

(c) $t = 5$ nm

(d) $t = 6$ nm

The 2,4,6nm samples were grown during the same run. It may explain the, different with the 5nm sample.

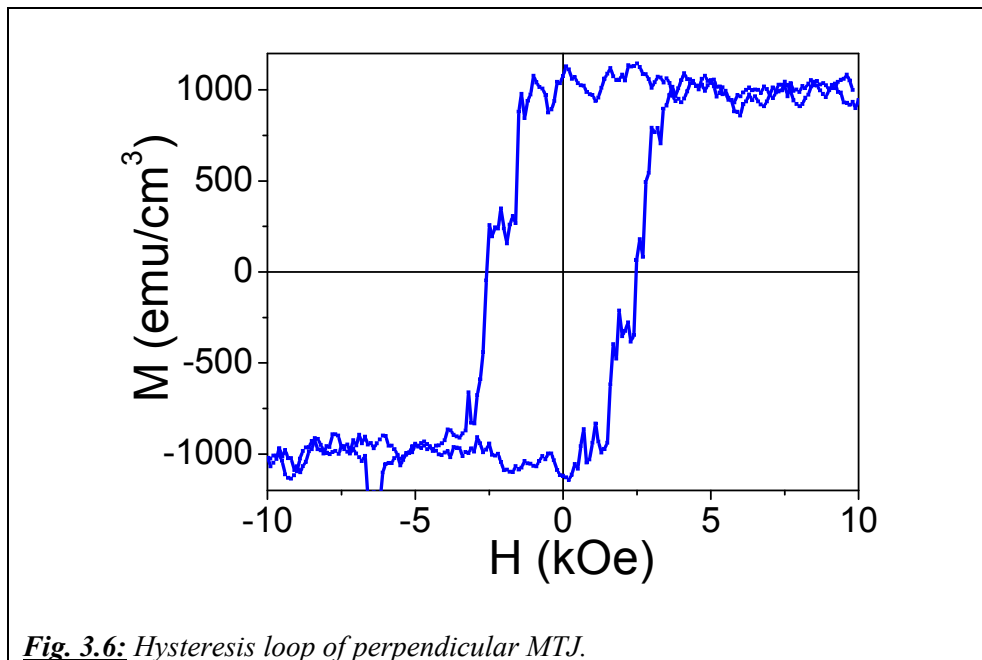
For MTJ sample:

The hysteresis loops were mainly measured using a vibrating sample magnetometer (VSM) at room temperature (see in Fig. 3.6). For all samples, the magnetic easy axis was along the [001] crystalline direction of the MgO substrate, because the [001] axis of the tetragonal $L1_0$ ordered ferromagnetic structure was perpendicular to the film plane.

The hysteresis loops are very square, each layer exhibiting 100% magnetic remanence. The top and the bottom ferromagnetic layers are switching at different coercive fields. This implies that both parallel and anti-parallel alignment of the orientation of the magnetization in the ferromagnetic layers can be obtained. The values of the coercive fields are around 0.18 T for the soft layer (5nm) and around 0.35 T for the hard layer (10nm). Since the two ferromagnetic electrodes are constituted with the same material, the difference of thickness of the layers results in the difference of coercive fields values between them. However, the main role lays on the way the FePt layers growing on: the top electrode which grows on MgO barrier has more defects inside than the bottom layer which grow on Pt buffer.

From the magnetization loops shown in Fig. 3.6, the saturated magnetization M_s is about 1100 emu/cm^3 and the first reversal is a third of the total magnetization which is coherent with the fact that the thickness of the soft layer is a third of the total thickness. We also know from kerr measurement that the sample is 100% remanent

The line corresponds to a major loop.

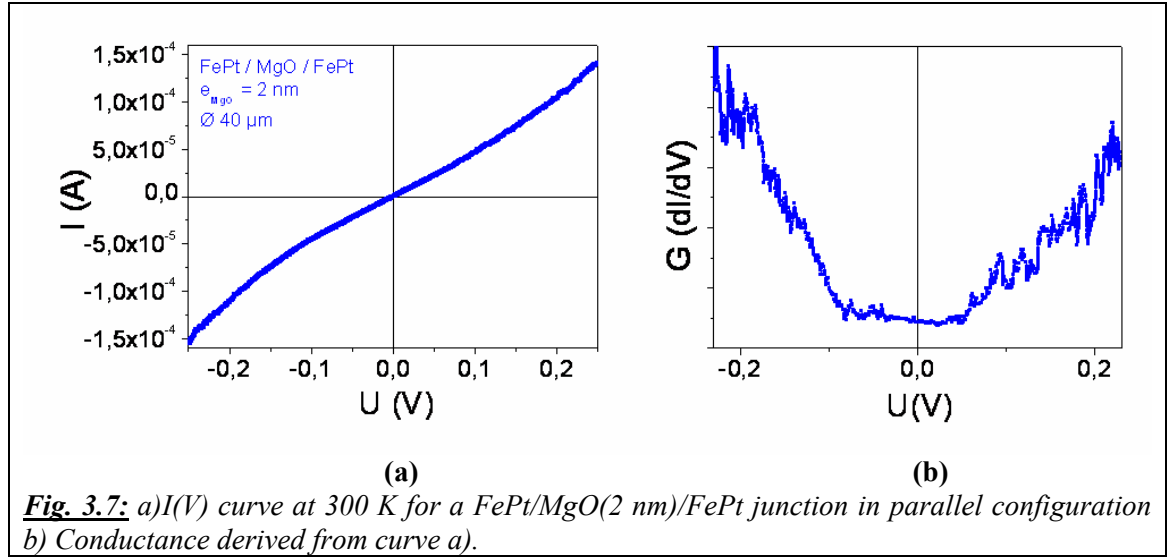


3.2.3 A few words on FePt/MgO/FePt tunnel junction transport properties

P. de Person measured some patterned FePt/MgO/FePt junctions of size $200 \mu\text{m}$ down to $40 \mu\text{m}$ in diameter [PER07a]. He observed standard non-linear $I(V)$ curve (see Fig. 3.7a and b) For a $40 \mu\text{m}$ tunnel junction of 2 nm of MgO, a fit using Simmons Model [SIM63] gives a barrier thickness of 1.9 nm and a height of 1.1 eV. These are good values considering that these

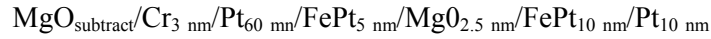
junctions are grown by MBE. It is quite difficult to have good thickness homogeneity on such a wide area. Considering the barrier height, the value deduced from the Simmons formula compares well with other published value on MgO tunnel barrier (from 1.1 to 1.7 eV for Parkin *et al.* [PAR04], 0.4 eV for Yuasa *et al.* [YUA04]). Even if we could not measure any TMR on these systems, we are quite confident that we observed tunnel transport through our MgO barrier.

I will say a last word on the TMR of FePt/MgO/FePt tunnel junction. Recently published results on FePt/MgO/Fe(*t* nm)/FePt tunnel junction with *t* varying from 0 to 3 nm show that there is no TMR for *t*=0 nm. The TMR rises to 120 % at room temperature when *t*=2 nm [YOS08]. Ab initio calculation on FePt/MgO/FePt shows that the TMR is more important for Fe-terminated FePt at the interface of MgO than for Pt-terminated FePt. It seems that the wave function symmetries at the interface play a crucial role. Maybe Fe terminated FePt/Mgo interface looks more like Fe/MgO wave function. It would explain why spin filtering in the Mgo barrier works well for this system than for Pt-terminated one.



3.3 Conclusion

In this part, we present the full epitaxy growth procedure for the structure:



The quality of the structure was controlled by RHEED pattern during depositing process and then once again by characteristic analysis. XRD showed good structural coherence and high long range order for each of our two electrodes. All the layers have good crystalline quality. TEM result showed a smooth surface, no pinholes and well defined tunnel barrier. The MgO barrier does not exhibit significant fluctuations of its thickness. The magnetization properties are good also with 2 separated reversals at 0.18 T for the soft layer and around 0.35 T for the hard layer in the very square hysteresis loop.

4 Magnetization dynamic and Domain wall propagation in FePt single layer

4.1 Study of propagation of magnetic domain walls in FePt single layer

All the experiments described in this chapter were done at the Laboratoire de Physique des solides at Orsay University within the facilities of Dr J. Ferré group, with the additional help of Dr J.-P. Jamet. We used polar magneto-optic Kerr effect (PMOKE).

In this part, I report the study we have done on single layer FePt thin film. The goal was the understanding of the dynamical process of domain wall propagation in a single layer. For this study we have used FePt samples with different thicknesses: it is worth noting that this ability we had to observe domain wall propagation phenomena in layers of different thicknesses, and of large uniaxial anisotropies is associated with the magnetocrystalline origin of the magnetic anisotropy in FePt. Most previous studies were performed on a system Pt/Co/Pt where the surface origin of the anisotropy intrinsically limited the available range of thicknesses to a few Angströms.

The structure of our samples, grown by molecular beam epitaxy, is:

MgO(100)/Cr(3 nm)/Pt(60 nm)/FePt(x nm)/MgO(3 nm)/Pt(4 nm)

with $x = 2, 4, 5$ or 6 nm.

The purpose of this study is to carefully understand the behaviors of the domains when the thickness of the sample is increased. As said, this is a new range of observations opened by the bulk origin of the FePt anisotropy. Therefore, we also study the velocity of the domain wall as function of field with different thicknesses of FePt.

The Kerr hysteresis loop with perpendicular applied field has already been shown in Fig. 3.5. In order to study dynamic process of domain wall propagation, we have visualized the evolution of magnetic domain by following two different procedures: as a function of field amplitude at constant pulse duration and for a defined field amplitude with varying pulse duration.

4.1.1 At thickness from 2 to 5 nm

4.1.1.1 Propagation depending on field

We begin our study with the thinnest sample (FePt 2 nm).

In order to generate a domain always in the right low corner of screen, we always used the same procedure:

- saturation in a -2.2 kOe field;
- apply a field $H = +120$ Oe;
- send 3 pulses with the VSC3 attached to the sample holder and with the LC (large coil) during Δt .

After this procedure from (a) to (c), the initial state has been created, with a domain appearing in the low right corner of the image, it is then possible to start studying the domain wall propagation. The process to develop the domain wall is:

- We saturate negatively down between -2.5 to -3 kOe (manually),
- We then apply a field of $+90$ Oe and send one pulse with VSC3 (pot 1000 and $\Delta t = 2 \mu\text{s}$) and several shorter pulses ($\Delta t = 0.2$ to $0.3 \mu\text{s}$). Usually, one gets a domain wall roughly "parallel" to the left side of the image.
- We cancel the DC field and record images under 2.2 s exposure time.

The sample was prepared from a magnetization \downarrow state in a negative saturation as shown in Fig. 4.1a. The black domain is the prepared domain for the \uparrow state and white color area observed the \downarrow state. Starting now from the positive field from Fig. 4.1b to Fig. 4.1e, we observed the full dynamic magnetization process with the thinnest FePt layer ($d=2$ nm).

First, applying one pulse with $H = 1650$ Oe during $\Delta t = 7 \mu\text{s}$ from Fig. 4.1a state, we observed the magnetization \uparrow state in black area shown in Fig. 4.1b. As the image shows, the domain expands its size by wall motion at the expense of the initial \downarrow state. A very interesting phenomenon shown in this image is the quasi-homogeneous large domain structure in which numerous small non-reversed \downarrow are embedded inside the created \uparrow magnetized state. This magnetic state has been called a "Swiss cheese" structure [FER97]. If we compare the applied field necessary to observe this state ($H = 1650$ Oe) and the hysteresis loop of Fig. 3.5a, we found the reason for small non-reversed areas, indeed it comes from a field not high enough to overcome locally all propagation barriers, or at least to make the domain wall propagation insensitive to the disorder associated with the defects. As we shall see later, the "Swiss cheese" state will disappear if we apply a field high enough.

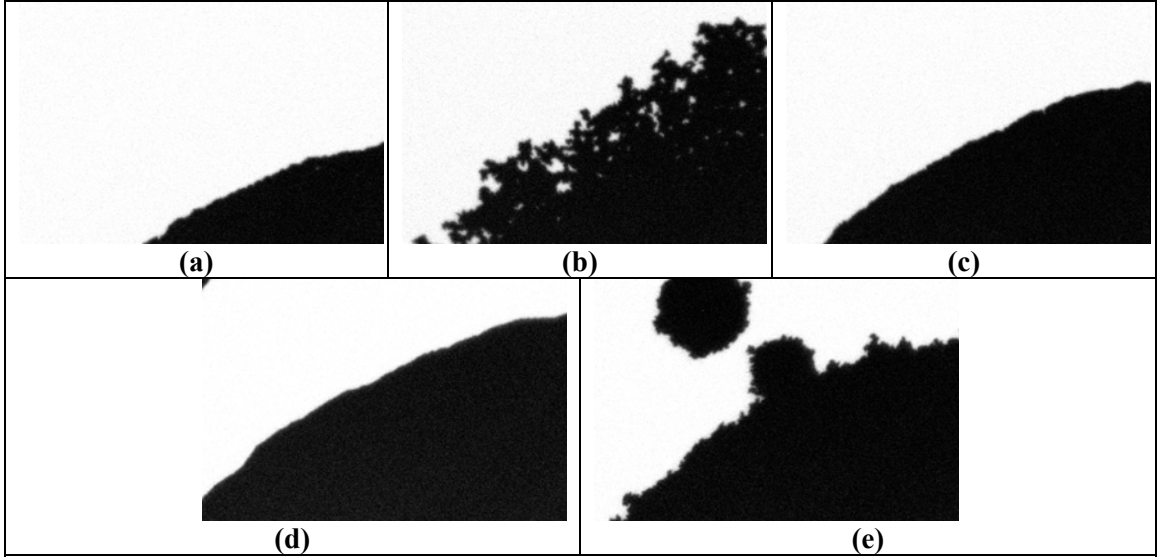


Fig. 4.1: PMOKE images of field evolution of the magnetic domain structure for sample FePt 2nm, starting from negative magnetization saturation:

- prepared domain after negative saturation.
- after applied field $H = 1650$ Oe during $\Delta t = 7 \mu\text{s}$ from the negative saturation.
- after applied field $H = 1912$ Oe during $\Delta t = 1 \mu\text{s}$ from the negative saturation.
- after applied field $H = 2310$ Oe during $\Delta t = 1 \mu\text{s}$ from the negative saturation.
- after applied field $H = 2660$ Oe during $\Delta t = 0.5 \mu\text{s}$ from the negative saturation.

Images size: $61.6 \mu\text{m} \times 41 \mu\text{m}$.

We also observed for the same field overhangs everywhere on the border of the domain. This effect is predicted in inhomogeneous materials. Indeed, domains then expand by avoiding the hardest magnetic regions. In such inhomogeneous magnetic materials, layer defects pin the domain wall during the propagation process. In order to continue its movement, a domain wall must find another path to propagate, thereby avoiding crossing the most strongly pinning defects.

Finally, one may assimilate the domain wall to an elastic line that propagates in a region with different energy barriers. The driving force – in our case the magnetic field – has to be high enough to overcome those energy barriers. If not, the line propagates without crossing the high pinning defects or regions. Thus we observe overhangs.

When increasing further the applied field, the local magnetization in the regions left unreversed switches progressively and disappears. This is confirmed in Fig. 4.1c and Fig. 4.1d. When we increased applied field up to 1912 Oe for Fig. 4.1c and then to 2310 Oe for Fig. 4.1d, the domain wall expands, the favored domain fills all the “Swiss cheese” unreversed areas inside and its border becomes smoother. We can conclude that in this case, the value of applied field decides the presence or absence of “Swiss cheese” and overhangs, and is the parameter controlling the shape of the domain border. Theoretically, at low field, the disorder inside a structured sample has the largest consequences on the domain wall shape because there is only a small driving force to induce domain wall propagation. In the case of FePt thin films, most significant defects are the ones locally modifying the chemical ordering, as such defects generally corresponds to large magnetic anisotropy defect. These are the antiphase boundaries, the local defects associated with imperfect chemical order... Some extended defects our groups studied extensively are the microtwins (strain relaxation defects). Even if we do not expect to observe these defects in the thinnest layers, relatively small microtwins may be observed in the 4 nm FePt layer grown on Pt(001). In addition, atomic steps correspond also to defects that may be significant in thin layers such as the ones we consider.

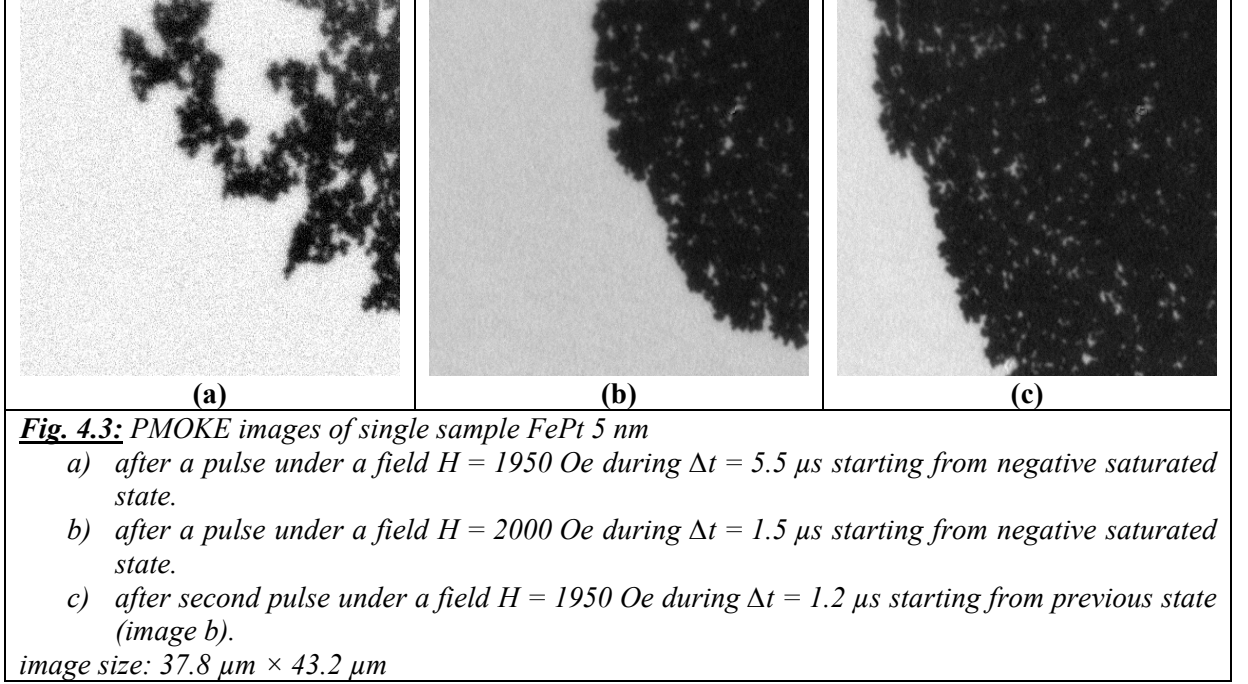
Conversely, at higher fields, the domain walls become less sensitive to the local disorder: domain walls resulting from propagation at high field are smoother than the ones resulting from propagation at low field.

However, one may object that we observe the opposite result – a rough domain wall – with an even higher field (2660 Oe) in Fig. 4.1e. Roughness even appears on the boundary of some new domains nucleated in unreversed part of the image at such a high field. The explanation can be linked to the way the field was applied. Indeed, as presented in the technical part, to apply a field, we add the combination of an electromagnet E-M and of a very small coil VSC3 (for pulse). To achieve field values similar to the ones used for Fig. 4.1e, because of the current limit in the VSC3, we must increase the value of the field created by the electromagnet E-M. Experimentally, when one uses the electromagnet with the VSC3 to get higher field amplitude, the field of the electromagnet alone must not exceed a certain threshold to avoid inducing significant propagation or deformation of the domain wall even out of the pulse duration. In Fig. 4.1e, the value of field created by the E-M (901 Oe during 0.75 s) was above this threshold: the DC field of the E-M generated the observed roughness. Moreover, new nucleation events occur due to the high total field amplitude (up to 2660 Oe during the pulse).

We performed next experiments with a sample of higher FePt thickness ($t_{\text{FePt}} = 5\text{nm}$) to confirm the “Swiss cheese” and overhangs effects observed at moderate field values.

Fig. 4.3 shows the magnetic state of the sample in several cases. As usual, the sample was saturated with a negative field ($H_{\text{sat}} = -4.2\text{ kOe}$). After $\Delta t = 5.5\text{ }\mu\text{s}$ under a field $H = +1950\text{ Oe}$, we observed local propagation of the domain wall in the 5 nm FePt sample, as shown in Fig.

4.3a. Even if the applied field is higher than saturation field, full reversal has not occurred yet. Indeed, the time of pulse is too short in this case ($\Delta t = 5.5 \mu s$) to end with a full reversal of the sample magnetization. This observation implies that domain wall propagation can be observed over a large range of applied fields, even above the quasistatic saturation field if one is able to apply short enough field pulses.



As predicted before in Fig. 4.1, once again the “Swiss cheese” and overhangs are clearly present. Some non-reversed areas also remain inside the reversed domain.

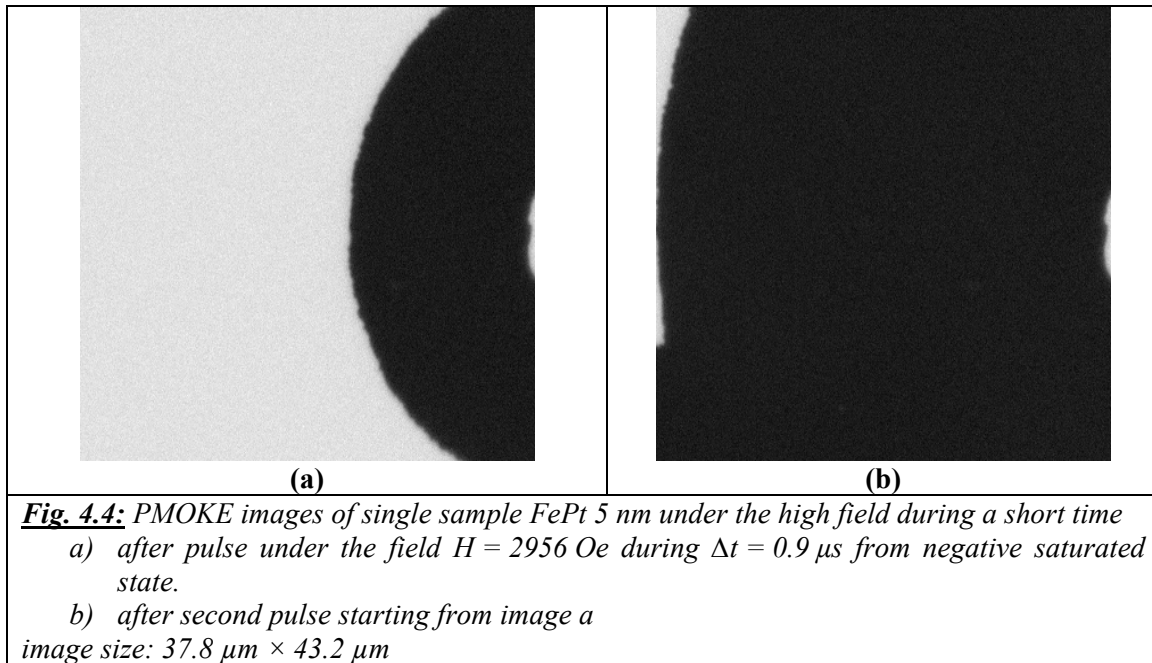
In Fig. 4.3b, we favored further domain wall propagation by providing a higher applied field. When a shorter pulse ($\Delta t = 1.5 \mu s$) is applied on the sample under a slightly higher field $H = 2000$ Oe, the domain wall switches to smoother geometries, and the reversed domain adopts (Fig. 4.3b) a more compact shape.

The growth process, illustrates on Fig. 4.3b, proceeds from the right corner to the left corner. The domain wall leaves behind many unreversed domains in the middle of the reversed area. This pattern is called a “Swiss cheese”. These un-reversed domains (on Fig. 4.3b) are smaller than before (Fig. 4.3a) and are very difficult to reverse. We continue by applying a second pulse with the same field value as before but during a shorter time $\Delta t = 1.2 \mu s$, without returning to saturation state. Fig. 4.3c shows the evolution of this magnetic domain after that pulse. The domain expands its size, but keeps its “Swiss cheese” appearance, with both old domains and new ones created during the expanding process.

It is necessary to apply a higher field value than 2000 Oe to induce nucleation and then to propagate the domain wall, with a high field value. Furthermore, even under the field value $H_a = +2.15$ kOe with typical $\Delta t = 1 \mu s$ (not shown here), the reversed domain displays many small non reversed magnetic area (Swiss cheese). So we increase the field up to 2960 Oe that is above the static saturation field of this sample (see Fig. 3.5). The pulse is applied during a short duration $\Delta t = 0.9 \mu s$ under the applied field $H = 2965$ Oe from an initial state, saturated in negative direction. The result is presented in Fig. 4.4. The nucleation domain looks like a giant bubble and the border is particularly smooth. Moreover, inside the domain, all the “Swiss

cheese” characteristics have disappeared, since the high applied field helps the system to overcome all the potential barriers. In this regime of quick propagation velocity, the pulse must be short to avoid obtaining a too big domain filling up the observed area. The second pulse was applied from domain in Fig. 4.4a and is shown in Fig. 4.4b. The domain now, is perfectly smooth. The white areas in centre of the right border, appearing in both if Fig. 4.4a and b, are related to the image processing, and are not related to the nucleation or propagation.

One relevant note can be deduced from the comparison of the 2 nm sample shown on Fig. 4.1c and the 5 nm one of Fig. 4.3c. The field required to overcome the “Swiss cheese” and “overhangs” is depend of the thickness of the FePt layer. Indeed, for the sample with 2 nm of FePt, we observe a smooth domain without “Swiss cheese” and “overhangs” at only 1912 Oe during $\Delta t = 1 \mu s$ while for the sample with 5 nm of FePt, “Swiss cheese” and “overhangs” are still there even with the higher field 2000 Oe and longer duration ($\Delta t = 1.5 \mu s$). It means that the thicker the sample is, the higher field we need to apply to avoid “Swiss cheese” and “overhangs”.



Summary:

The “Swiss cheese” and “overhangs” patterns appear after low field pulses. These features are not observed after high enough field pulses that have to be larger with higher FePt thicknesses.

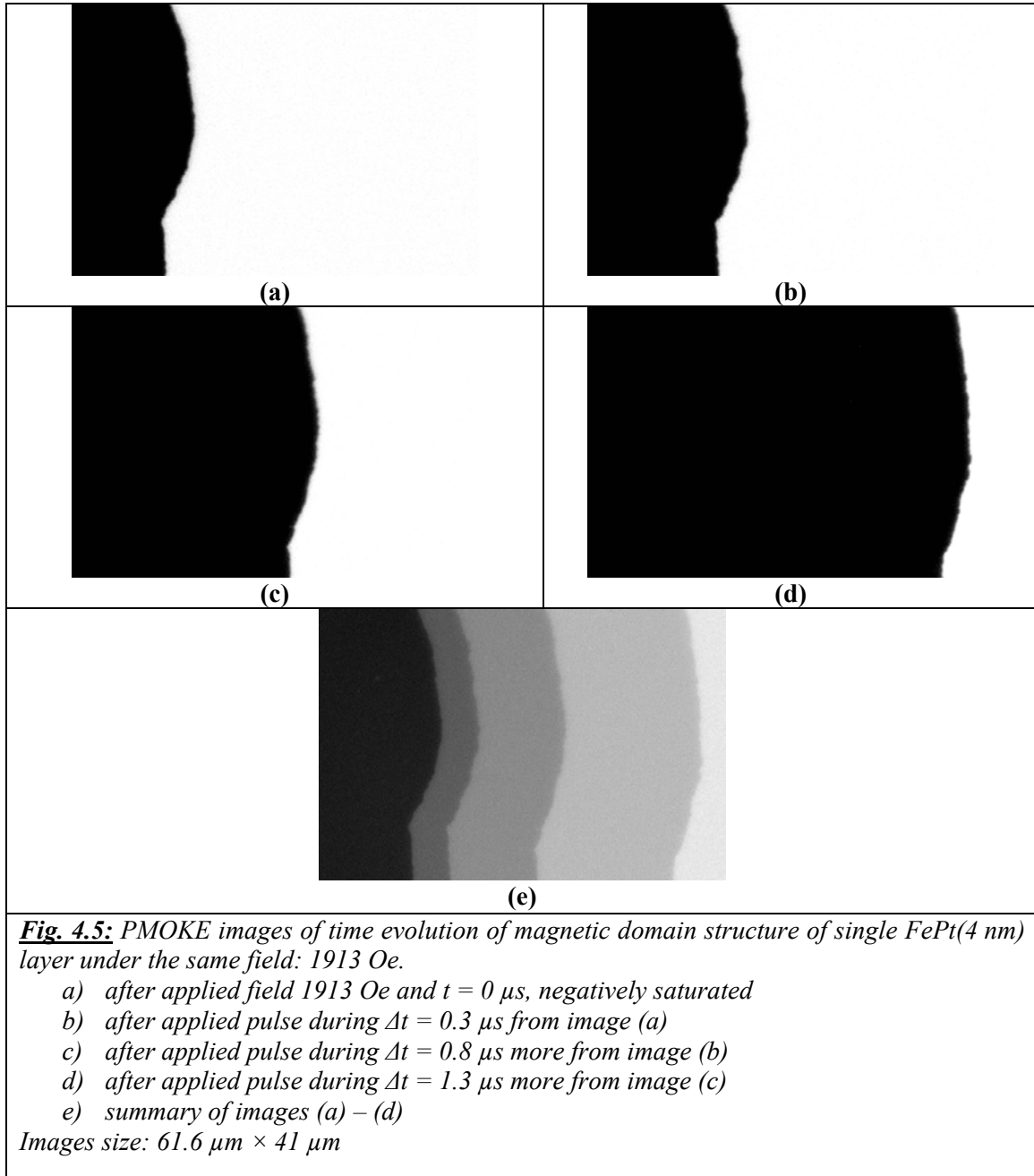
Now that the characteristics of the propagation under varying field have been developed, let's see the influence of time on the propagation.

4.1.1.2 Time dependent propagation

Since the magnetization reversal process can be stopped for a long time at any moment by switching the field off [FER97], it is easy to visualize the change of the magnetic domain under a given field H as a function of time.

The images from Fig. 4.5a – e shows the evolution of magnetic domain structure under the same field $H = 1913$ Oe after pulses of different durations. All the images were taken on the same sample area.

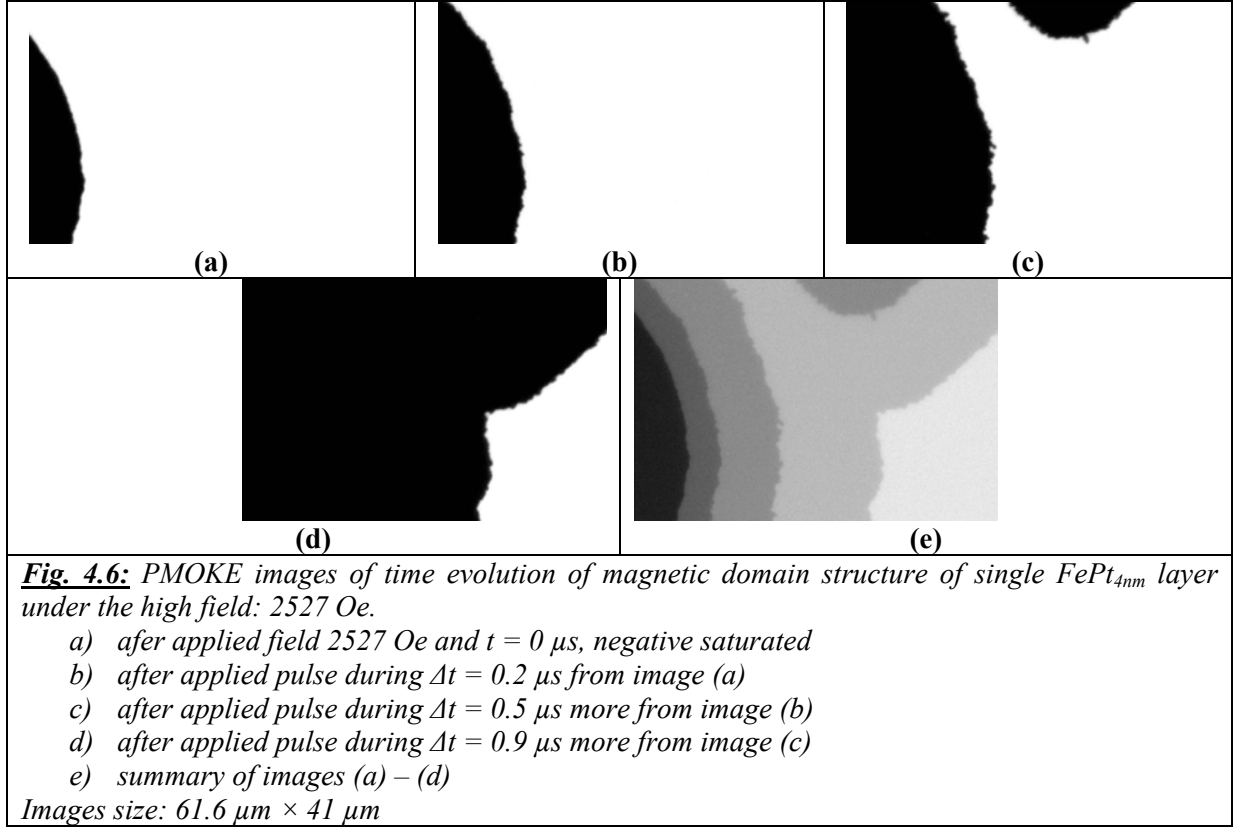
First, the experiment begins with the negative saturation with magnetization \downarrow in white color, then we apply a field $H = 1910$ Oe at time $t = 0$ s. Fig. 4.5a shows the nucleation centre at $t = 0$ s from the beginning, after the initial state for further propagation experiments. As already shown is Fig. 4.5a, the magnetization \uparrow of single domain state is in black and the \downarrow one in white. We start to apply pulses on the sample with duration $\Delta t = 0.3 \mu\text{s}$, $0.8 \mu\text{s}$ and $1.3 \mu\text{s}$ without coming back to saturation state in between. We got the time evolution of the magnetic single domain structure for the sample 4 nm and it is illustrated in Fig. 4.5b – d and summed up in Fig. 4.5e, where we can see clearly that the propagation is developing from the left to the right. The domain \uparrow (in black) expands by wall motion with a visible speed. The smoothness of the domain wall allows the calculation of the wall velocity with small error bars. The smooth border is in an indication that we are not in a thermally activated regime at that field value. However, the roughness on the domain border is not exactly 0. This is explained by the long duration - low field contribution of the electromagnet E-M, as explained in the previous part concerning the field dependent propagation.



Another series for the same sample (FePt 4 nm) at a higher field (2527 Oe) is presented in Fig. 4.6. In all those images, the propagation from Fig. 4.6a to Fig. 4.6d magnetic state is due to VSC3 $H = +1755$ Oe during $\Delta t = 0.2 \mu s$ and the E-M $H = 772$ Oe. So $H_{total} = 2527$ Oe. The domain wall is smooth but we see more clearly the low field contribution of the E-M as compared to the Fig. 4.1 series.

At high field, we observe that the domain wall looks rougher. It comes from 2 reasons: first, because of the electromagnet E-M at 772 Oe and second, because the value of the field in this case may correspond to the unstable region of the velocity curve (refer to the figure presenting

the velocity curve). Especially, on Fig. 4.6c, what is likely a new domain begins to appear (with much the same roughness) and after $0.9 \mu\text{s}$ more, those two domains combine together as presented in Fig. 4.6d. The bump observed on Fig. 4.6d induces a lack of precision in the velocity determination. Therefore we cannot determine the velocity curve above this field value.



4.1.1.3 Demagnetization state

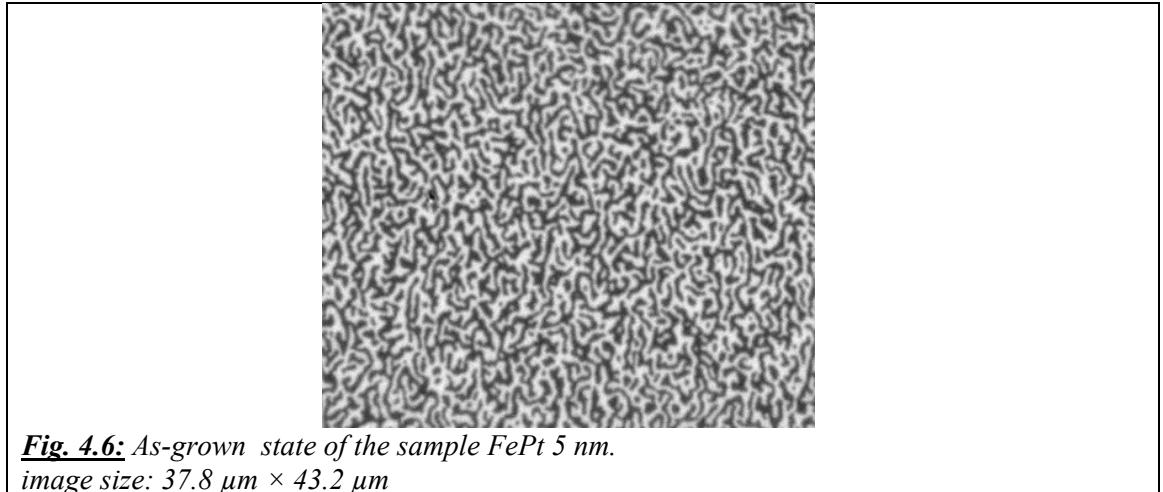


Fig. 4.6 shows as-grown state of the 5 nm FePt sample before any applied field on the sample. The ribbon structure has a space period of the order of $1.2 \mu\text{m}$ ($0.6 \mu\text{m}$ is the width of black or

white ribbons). The domain structure has standard type which is common for magnetic domain of high anisotropy material.

4.1.1.4 Conclusion

In this part, we highlighted the propagation patterns of a reversed magnetic domain for one single high-anisotropy FePt layer over a large thickness range: 2, 4 and 5 nm. Both the influence of the applied field and of the pulse duration have been observed.

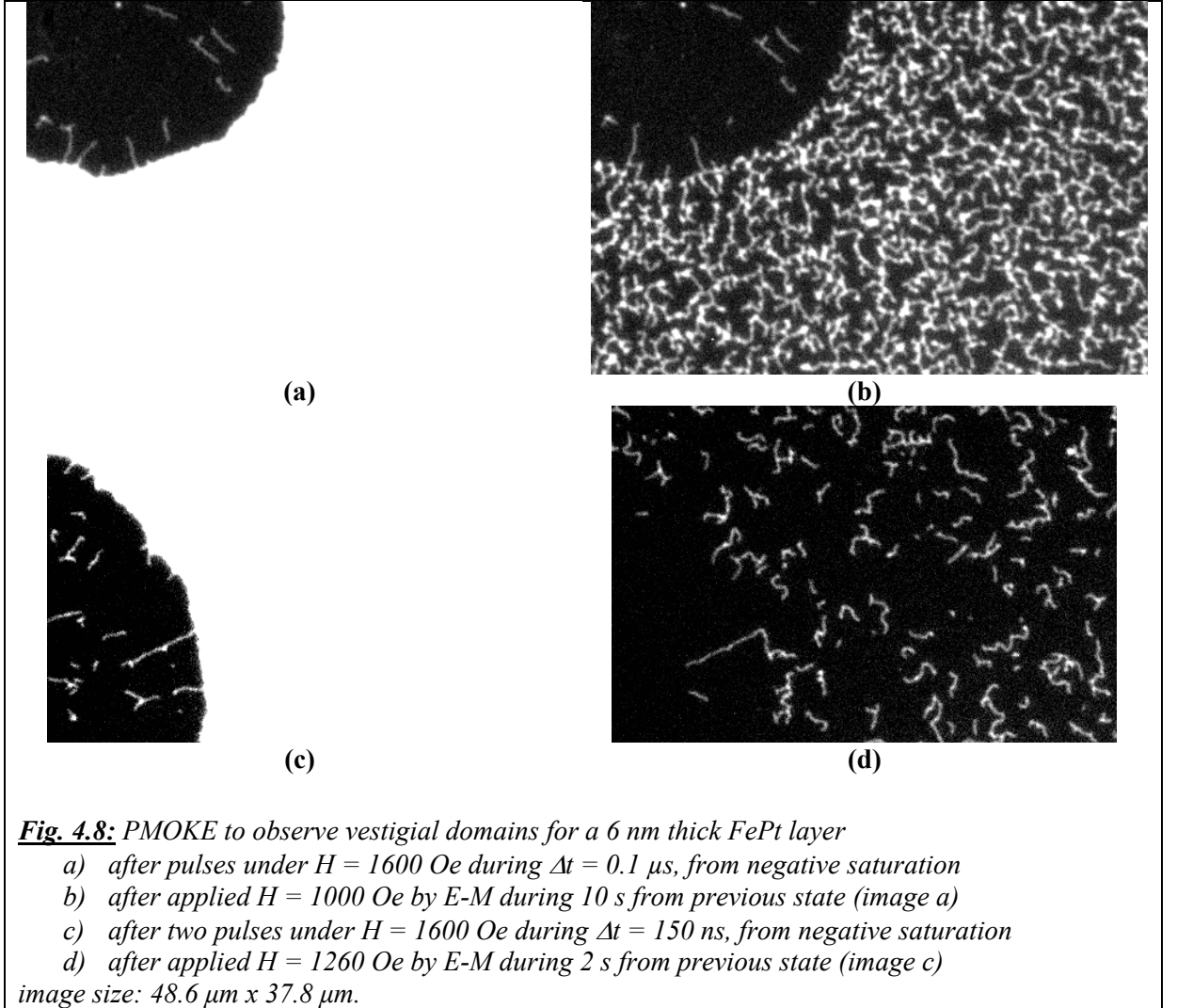
We observed “Swiss cheese” and “overhangs” patterns, characteristics of situations when the field is not high enough to render the domain wall propagation seemingly independent of local defects. When these energy barriers are overcome by higher field, the propagating domain finally becomes smooth and filled up all the unreversed areas previously left. The value of the field required to obtain a smooth domain wall depends on the thickness of the layer and increases with it. As expected, with or without “Swiss cheese” and “overhang”, domain develops with an increasing velocity at higher fields.

Experimentally, some limits of the experimental set-up appear. Indeed, the field from the electromagnet $E - M$ has to be applied over longer period than the short pulse duration. With high values of $E - M$, it can either make the border of domain rough or enables the nucleation of new domains.

4.1.2 Domain decoration when increasing thickness

In the previous parts, we observed the domain behavior in the low FePt thickness range (2, 4 and 5 nm), even if these thicknesses are higher than the ones previously observed in similar conditions for Pt/Co/Pt layers. Now, we will further increase the FePt thickness. This will result in enhanced dipolar effects (see the book of Hubert and Schafer [HUB98]). In addition, the defects present in the layer may be somewhat different, as we know from previous PhD works in our group that micro-twins progressively build up with increasing thickness in FePt/Pt(001). Both these changes may render the domain behavior more complicated. Here, we describe the behavior of domain walls as observed in 6 nm thick FePt layers.

4.1.2.1 Observing the vestigial 360° winding wall



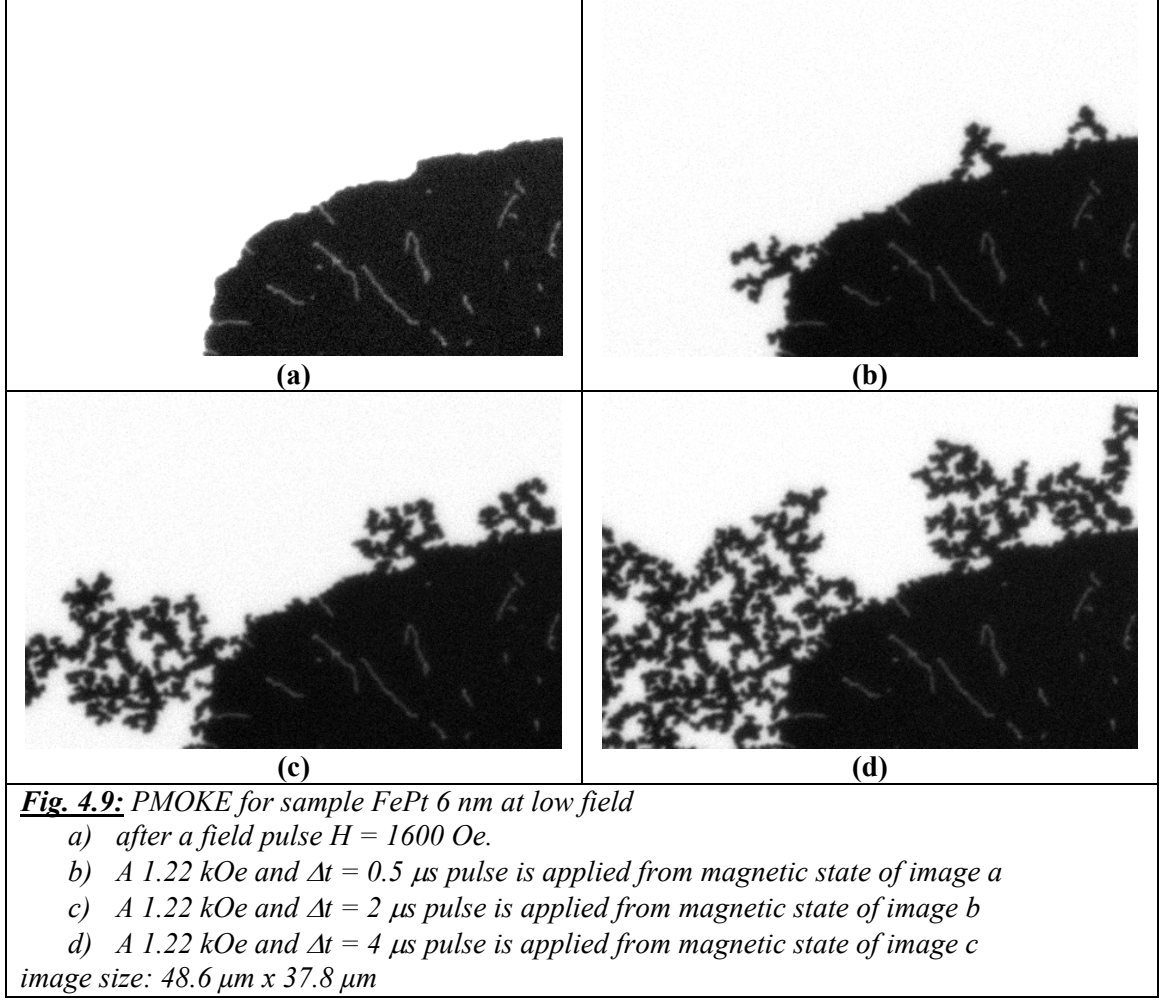
The sample is saturated under $H = -2$ kOe then a field pulse $H = +1.6$ kOe during $\Delta t = 0.1 \mu s$ is applied: a domain nucleates in the upper left corner Fig. 4.8a. The dipolar field stabilizing these few filaments is larger than 1.6 kOe. From the magnetic state of Fig. 4.8a, one applies a new field pulse (+1 kOe $\Delta t = 10$ s). The result is shown in Fig. 4.8b. The pulse amplitude is not sufficient to reverse the filaments left by the first pulse (upper left corner). The domain wall keeps propagating through the sample; a dense network of 1d magnetic defects (similar to a ramified random neuronal network with total interconnection) is left over. White ribbons percolate from the boundary of the nucleated domain (Fig. 4.8a) to the boundary of the picture (Fig. 4.8b). The density of the white ribbons decreases with the applied field. One possibility is that they originate from pinning defects. Most probably those defects have a strength that has a Gaussian distribution. Then it is normal that the density of the white ribbons decrease with the applied field.

We performed one more experiment to gain additional understanding of the vestigial 360° winding wall in the 6 nm thick FePt layer (Fig. 4.8). First, after applying 2 pulses with the same field $H = 1600$ Oe during a longer duration ($\Delta t = 150$ ns) than for Fig. 4.8a, we observe in Fig.

4.8c also some channels inside the nucleated domain, as we described above. This image shows a magnetic structure similar to Fig. 4.8a. We continued by applying a field $H = 1260$ Oe during $\Delta t = 2$ s without returning to the saturation state (the image is presented in Fig. 4.8d). The field is larger than in Fig. 4.8b and the large part of Fig. 4.8b structure has vanished. Furthermore, 1d structure is less dense than in Fig. 4.8b and the defect network has lost its interconnection. The domain growing in the \uparrow state is black. The non-reversed \downarrow states are white and, as already pointed out, the white filaments are due to some pinning defects which favors magnetically non-reversed channels called 360° walls. Nevertheless, the white ribbons inside the black domain need extra energy to be reversed that is not necessarily provided by a small field. With an applied larger than for Fig. 4.8b (as shown on Fig. 4.8d), the \downarrow state looks like a complex array of connected narrow ribbons. The remaining magnetic white ribbons disappear progressively with increasing H , as shown in Fig. 4.11 and Fig. 4.12.

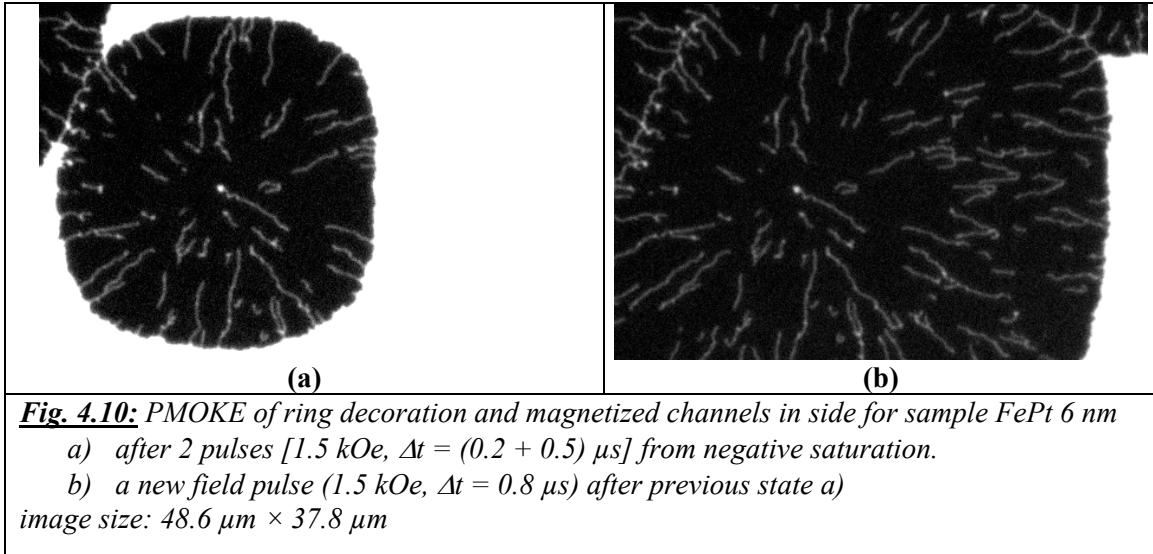
4.1.2.2 Propagation at low field

Finally, we studied the behavior of the domain at low field). All the results are shown in Fig. 4.9. A domain is nucleated with a field pulse ($H = 1.6$ kOe) after saturation under -2.2 kOe as shown in Fig. 4.9a, it is similar to the ones observed in Fig. 4.9a or Fig. 4.10a. Then a pulse under the field $H = 1220$ Oe during $\Delta t = 0.5$ μ s was applied from the state of Fig. 4.9a, without returning to the saturated state. The domain walls start to appear, from the border of the nucleated domain. They expand more and more after some pulses more in Fig. 4.9c and d. Under the high field (after saturation in this case), the domain wall don't have bubble shape any more, and have ribbons looks. This structure is still stabilized after several pulses. This dendritic growth is the sign of thermally activated reversal. When one balances the applied field, the demagnetization field and the domain wall length, for small applied field, the domain propagates by small branches (dendrites) that are stabilized by the demagnetizing field. Creating long domain wall costs energy, but that cost is balance by the gain in demagnetizing energy coming from these small reversed branches surrounded by a large unreversed domain. This balance is only valid as long as the applied field is not large enough to allow the domain wall in the hard layer to overcome most of the defects.



4.1.2.3 Propagation at high field

The sample, as usual, was saturated in negative direction; putting the FePt layer in a down (\downarrow) magnetization state. Starting from a nucleation event, we applied several pulses with field $H = 1.5$ kOe with different durations as shown in Fig. 4.10a and b. In Fig. 4.10a, after 2 short pulses $\Delta t = (0.2 + 0.5) \mu s$, we observed the up (\uparrow) domain state in black color. It looks like a large bubble. On the left upper corner, another domain propagates. An interesting detail in this image is the existence of many filaments in white color, which have the same direction, going away from the small white dot located at the centre of the bubble (the nucleation site). These white filaments correspond to \downarrow states, in other words still unreversed areas. The results we obtained here are exactly what Wiebel and collaborators observed in [WIE06]. We propose also the same physical explanations for our experiments, reported below for the reader convenience.



Generally, in ultrathin films with perpendicular anisotropy, the final sequence of the slow magnetization reversal brings into play regions with non-reversed \downarrow magnetized channels, also called vestigial 360° winding walls (these are the filaments presented in Fig. 4.10)[WIE06]. These filaments are built by two distinct mechanisms. In the first one, a few domains are nucleated far away from each other and after expansion; their walls come close together, forming a connected array of channels that is stabilized by magnetostatic forces like we see in Fig. 4.10a. For the second mechanism, as soon as a wall is touching an extrinsic defect during its motion, it coils around it to finally form two facing walls preferentially oriented along the mean displacement vector. The filaments inside the bubble of image are probably of the second type. This leaves \downarrow magnetized channels that are pinned at one of their extremities as in Fig. 4.10a. From the domain state of Fig. 4.10a, we induce further domain wall propagation with a second but identical pulse ($\Delta t = 0.8 \mu s$). We observe in Fig. 4.10b the expansion of \uparrow state domain, still with bubble decoration. All the filaments of Fig. 4.10a are still here and longer now. Furthermore, other filaments appear, presenting new connected channels coming from the fact that two channels may connect each other to form one channel.

Second type \downarrow magnetized channels can shrink after a time delay through their sudden thermally activated collapse depending on the defect located at its extremity shown in Fig. 4.11a. Since the magnetostatic interaction is weak for thin magnetic layer as the one we observe, a small increase of the field value is sufficient to wash out the second type of up-magnetized channels [WIE06]. When we increase the field by an amount as small as only 200 Oe with respect to Fig. 4.10a, (Fig. 4.11a), we end with very short filamentary \downarrow domains. With another pulse starting from Fig. 4.11a state during $\Delta t = 0.8 \mu s$, we observe the expansion of black domain but unchanged white channels (see on Fig. 4.11b). On the right of image, a short filament appears, but this one is due to a two domain confluence.

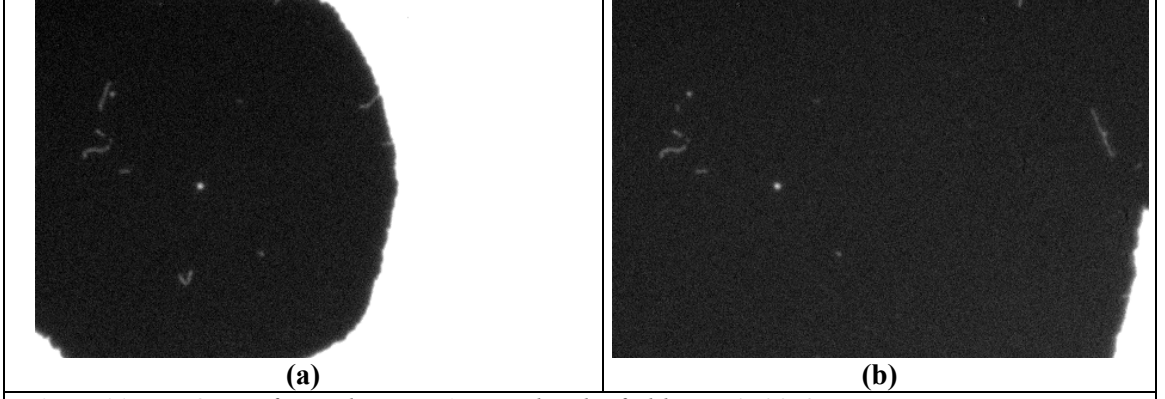


Fig. 4.11: PMOKE of sample FePt 6nm under the field $H = 1700$ Oe

- a) after 2 pulses [1.7 kOe, $\Delta t = (0.2 + 0.5) \mu s$] from negative saturation.
 b) a new field pulse [1.7 kOe, $\Delta t = 0.8 \mu s$] after previous state a)
 image size: $48.6 \mu m \times 37.8 \mu m$.

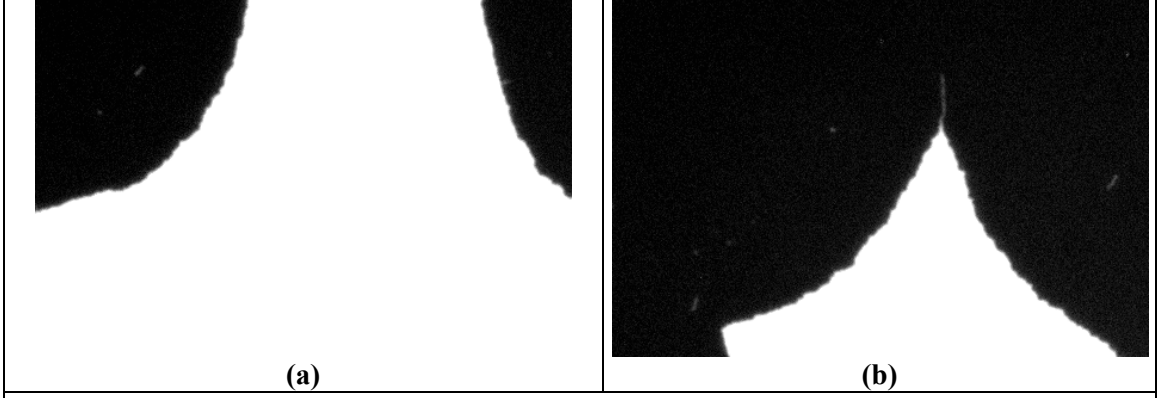


Fig. 4.12: PMOKE of sample FePt 6 nm under the field $H = 1770$ Oe

- a) after two pulses [1.77 kOe, $\Delta t = (0.2 + 0.5) \mu s$] from negative saturation.
 b) a new field pulse [1.77 kOe, $\Delta t = 0.8 \mu s$] after previous state a)
 image size: $48.6 \mu m \times 37.8 \mu m$.

Finally, all the channels inside a domain can be removed by increasing the field by an additional small value of 70 Oe (with respect to Fig. 4.10a and b). There are almost no more filaments in Fig. 4.12a. This is confirmed in Fig. 4.12b when we applied one new pulse during $\Delta t = 0.8 \mu s$ after the state of Fig. 4.12a. Again, this small domain will disappear later by depinning at one of its extremities.

4.2 Study on domain wall velocity in FePt single sample

4.2.1 Introduction

In the previous part, we have discussed the structure and dynamical behavior of domain in single sample with different thicknesses. Therefore, we have a clearer picture of the propagation process in our films. In this part we will focus our attention to domain wall dynamic processes.

We will discuss measurements of domain wall velocity as a function of applied magnetic field recorded on FePt thin films with different thicknesses.

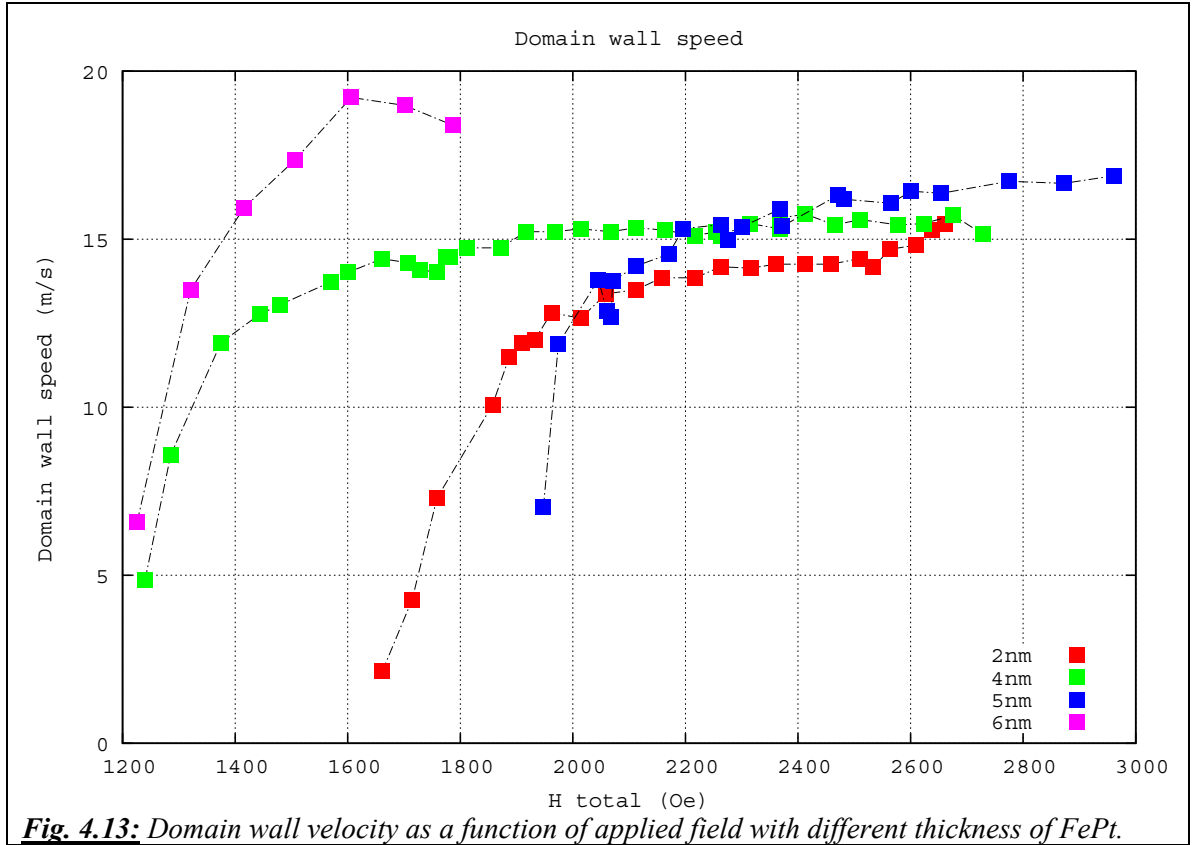
Many studies concerning domain wall motion as a function of applied field have been reported in the literature. However, most of them focused on ultrathin films. Still now, models of domain wall propagation are mostly 1D. In addition, most studies on thin films with perpendicular magnetization were on Pt/Co/Pt or Au/Co/Au trilayers, intrinsically restricting thicknesses to the sub-nm range.

However, as DW seems to have a future in logic application, 1D models are not sufficient to describe propagation in nanostructures, as it seems difficult to discard any thickness dependent effect. Furthermore, as reduced lateral dimensions are required for data density, and as data stability then requires significant magnetic volumes, practical applications would require avoiding too low thicknesses

Taking advantage of the bulk origin of the anisotropy in FePt layers, I will now describe the dynamic processes observed in thin film with different thickness. I will stress on details that separate our results from the standard 1D model.

4.2.2 Domain wall velocity in FePt single layer with different thickness

The experiments were done with a FePt single layer of 4 different thicknesses: 2, 4, 5, 6 nm. The aim was to find the general rule for the dependency of domain wall velocity on thickness. The Fig. 4.13 presents the results from all samples we measured. Experimentally, applied fields were created by adding two fields: one from the VSC3 (H_{VSC}) and the other one from the electromagnet (H_{EM}). In this procedure, the VSC3 field is applied during 1.5 s or less (creating the pulse), while the field from the electromagnet cannot be applied during less than 1 second for practical reasons (H rise time). In spite of its longer Δt , as long as the H_{EM} field is small enough. It assumed to have no effect outside of the very short Δt window where the H_{VSC} is acting.



4.2.2.1 The quick view from experiment data

FePt (2 nm) sample:

The red curve shows the propagation data for the FePt (2 nm) sample. Below a field $H_{\text{threshold}} = 1650$ Oe, the domain wall speed is impossible to evaluate. Indeed, the propagation leaves many non reversed areas behind the propagated domain wall. Furthermore, we cannot even define the domain wall position. There is a lot of hard pinning centers and it would be impossible to define a "creep" field range (this creep regime makes sense only in a weakly disordered system).

We will discuss later in the manuscript the nature of the shoulder occurring at around 2400 Oe. It is tempting to see in that the shoulder the signature of a Walker anomaly. However it has to follow certain characteristics. At last, the mobility of $v(H)$ curve is about 6.4×10^{-3} m/sOe or 64 m/sT.

FePt (4 nm) sample:

The same comment holds for the sample 4 nm FePt (data in green). At last, the higher mobility of $v(H)$ curve is about 8.9×10^{-3} m/sOe or 89 m/sT.

FePt (5 nm) sample:

The next experiment reported now is the study on a sample of 5 nm FePt single layer (data in blue). The structure of this sample is the same as the MTJ without the hard layer.

As observed on Fig. 4.13, the velocity curve has clearly no breakdown. The velocity curve as a function of field presents several characteristics:

- The velocity increases dramatically with field from a field value which is in the vicinity of 1.95 kOe, which represents a local pinning energy.
- The domain wall for this low field value is fractal with overhangs.
- At high field, the velocity tends towards an asymptote with a velocity value smaller than 20 m/s.
- There is a “shoulder” from the field 2.5 kOe up to the maximum applied field. Since 2.5 kOe, the velocity increase slower than before. However, we do not see a velocity breakdown as for the MTJ sample.

FePt (6 nm) sample:

Velocity in the 6 nm sample is shown in pink color. The velocity increases up to the maximum velocity ≈ 20 m/s (around 1.6 kOe) and then decreases. The decrease of velocity above 1600 Oe maybe correlated to the increase of domain wall roughness (see back part 4.1.2).

With the exception of the 5 nm thick sample, the data show a clear tendency: domain wall speed increases with thickness for a given field, and depinning occurs at a far lower field, with speed rapidly increasing from lower critical fields also with increasing thicknesses. The 5 nm sample may differ mainly by larger pinning fields on defects. From extensive background of the laboratory on FePd and FePt thin films, we know that, if overall parameters such as anisotropy are well reproducible from one sample to the other, the strain relaxation defects may adopt various distributions with poorly understood causes. This may be the origin of the (apparently) anomalous comportment of the 5 nm sample at low fields.

4.2.3 Calculations from hypothesis of the regime where experiment data stay for single sample

From all the curves, it is difficult to say that we observed the Walker breakdown or not. A velocity breakdown seems to appear for the sample 2 nm, but less clear for sample 4 nm and do not appear in the 5 and 6 nm sample. The main point now is we need to determine in which regime we are: are we able to observe the regime with Walker breakdown or are we far above the walker breakdown and in precessional regime for all displayed data? To answer this question, we explore different hypotheses on the base of rough calculations.

4.2.3.1 The first hypothesis: we are in the regime with Walker breakdown.

If we believe that we are in this regime and observed the Walker breakdown, it means that we also observe the steady regime below Walker breakdown. As a result, all the theories for Walker field and domain wall velocity in this regime should apply.

In the steady regime, the Walker field and domain wall velocity are given by formulas below (presented in the part 1.1):

For domain wall velocity:
$$v = \gamma(\delta/a)H.$$

Starting from the expression of H_W for thin films [MOU07], the Walker field is calculated by:

$$H_W = 2\pi \alpha M_S |N_y - N_x|$$

Since the FePt film thickness, t , is varying from 2 nm to 8 nm, $|N_y - N_x| = t / (t + \delta)$

With:

$$\gamma = 1.7 \cdot 10^7 \text{ (Oe.s)}^{-1}$$

$$M_S = 1100 \text{ emu.cm}^{-3}$$

And δ , the width of domain wall, is calculated by $\delta = \pi \sqrt{A/K}$

In the case of FePt, $\delta = 4\text{nm}$.

The difficulty in our case is we do not know the value of the damping factor α for FePt. However, α is related to the mobility μ of the velocity curve, in both the steady regime and the precessional one (refer to formulas below). Therefore, from the experimental data, we can extract a value for α . But beside that, we know the value of damping factor in FePd $\alpha = 0.02$ (from measurements of ferromagnetic resonance [YOU99]), these gives an idea of realistic order of magnitude for α (see Table 4.1).

The first idea, for the steady regime (before Walker breakdown), is that the velocity is linear with field: $\mathbf{v} = \gamma(\delta/\alpha)\mathbf{H}$. From the experiment data, we try to fit the linear curve $\mathbf{v} = \mathbf{mH}$, calculate the mobility $\mathbf{m} = \gamma(\delta/\alpha)$ of the linear curve, from that we can find the value $\alpha = \gamma\sigma/\mathbf{m}$ with each thickness of FePt. The linear fits for $\mathbf{v} = \mathbf{mH}$ are shown in Fig. 4.14 and the results of damping factor are written in Table 4.1.

Practically, this means that the steady motion regime would be observed over a restricted range of field values, after the rapid increase of speed with field, once depinning is effective, and before the Walker field value, apparent as a dip or a plateau (shoulder) of the speed values (see Fig. 4.14).

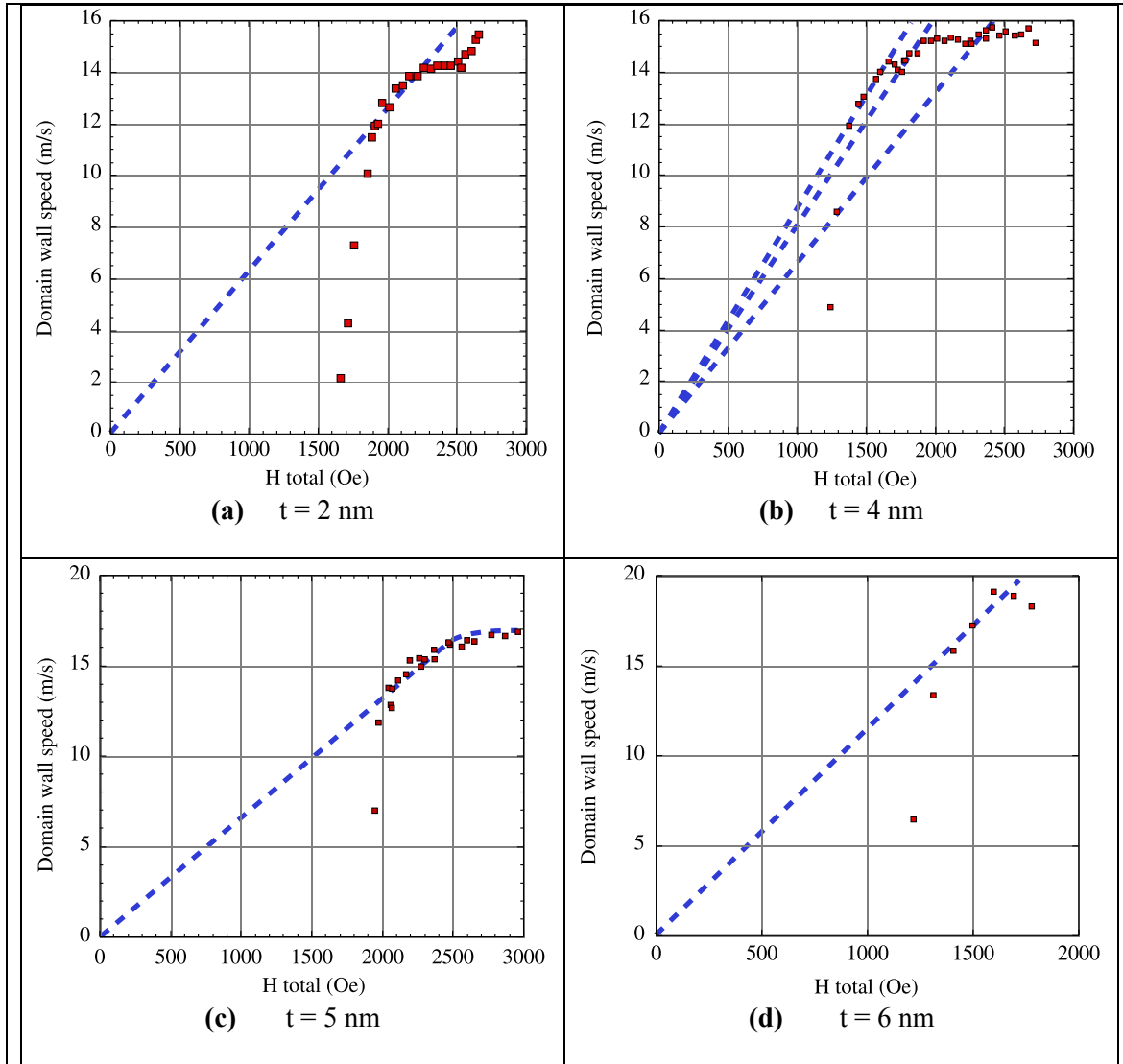


Fig. 4.14: Domain wall velocity $v = mH$ for different thicknesses of FePt in the hypothesis of steady regime with $m = \gamma(\delta/\alpha)$.

Experiment data: red points

Assumed flow regime: blue dotted line

Thickness of FePt t(nm)	Mobility m (m/(Oe.s))	Damping factor α	uncertainty of α	H_w caculated from α (Oe)	H_w experiment (Oe)
2 nm	0.82	10.79	+/- 0.04 (6.9%)	24781	2200
4 nm	0.70	7.72	+/- 0.028 (3.2%)	26665	1700
5 nm	0.78	10.15	+/- 0.039 (5.8%)	38953	2400
6 nm	0.45	6.02		24952	

Table 4.1: value of damping factor and Walker field with linear fit $v = \gamma(\delta/\alpha)H$ in steady regime.

To account for the experimental data, the model produces unrealistic values of α (varying from 6 to 10). In addition, the model is not consistent in another aspect: the value of Walker field H_w calculated with the derived value of α is not comparable with the field values of the Walker breakdown we may guess from the experimental data (see in Table 4.1).

It is then very likely that the plateaus we observe in the velocity data should not be associated with the Walker breakdown. If we do not observe the Walker breakdown, it is possible that we are above the Walker breakdown? We would then be in the precessional regime.

4.2.3.2 The second hypothesis: we are in the precessional regime above the Walker breakdown

The precessional regime, observed above the Walker field, corresponds to a second linear regime. In this one, the formula which calculates the domain wall velocity is given by:

$$V = \gamma\delta/(\alpha+\alpha^{-1})H \quad (4.1)$$

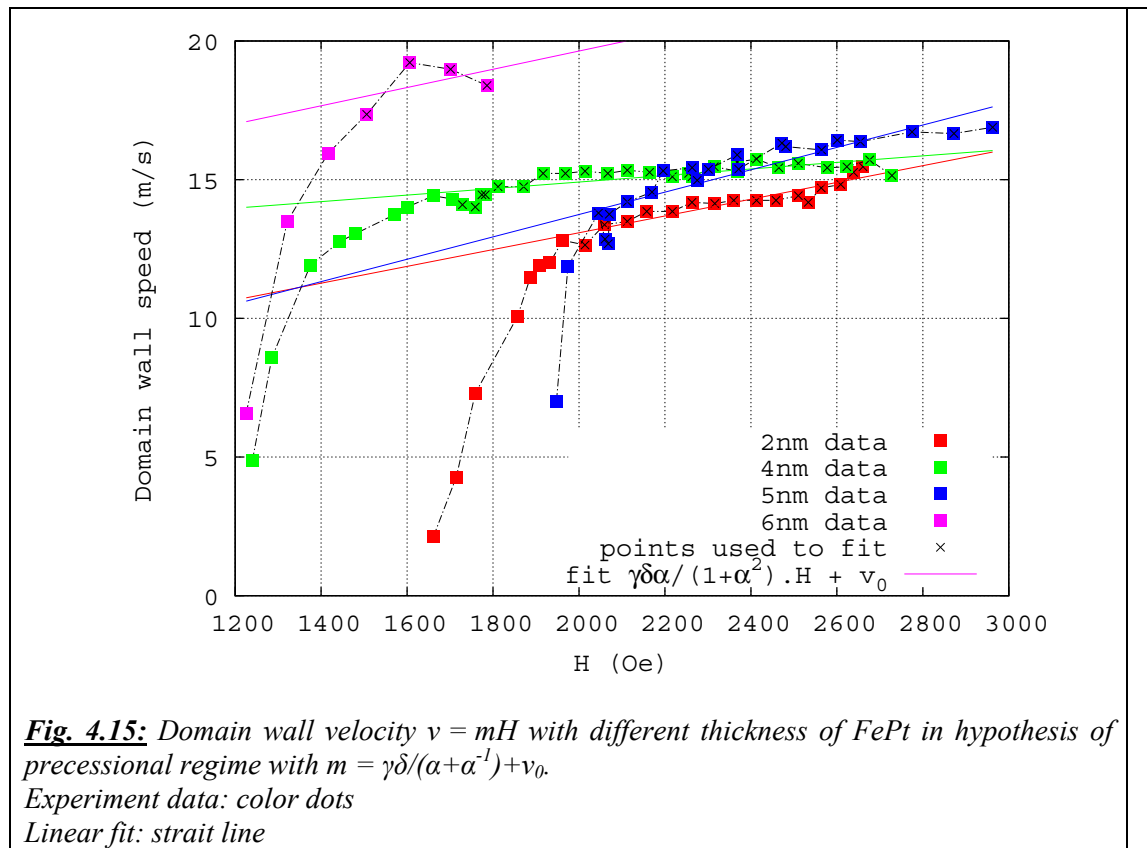
However, the behaviors of MOKE experiment data do not match properly with the formula (4.1) because the data can not go to at $H = 0$. Therefore we need to add an offset for the data. The formula in this case becomes:

$$V = \gamma\delta/(\alpha+\alpha^{-1})H + v_0$$

with v_0 is an offset.

For the hypothesis of precessional regime, data taken at the high field depend on the behavior of the velocity curve (above 2.0 kOe for the sample 2, 4, 5 nm but not for sample 6nm because the 6nm data lacks of experiment points).

The mobility $m = \gamma\delta/(\alpha+\alpha^{-1})$ in this case is lower than the one of the steady regime. From this formula, the values of α are calculated at every experiment data point (except low field points) and then data fitting gives us the value of α for each thickness in Table 4.2 and the fitted velocity curve in Fig. 4.15.



Thickness of FePt t(nm)	Mobility m (m/(Oe.s))	V_0 (m/s)	α	uncertainty of α	H_w caculated from α (Oe)
2	0.006	7.0	0.043	+/-0.005 (11%)	297
4	0.007	12.6	0.017	+/- 0.003 (16%)	118
5	0.006	5.7	0.057	+/- 0.007 (12%)	394
6	0.011	13.1	0.047		325

Table 4.2: Value of damping factor and Walker field with linear fit $v = \gamma\delta/(\alpha + \alpha^{-1})H$ in precessional regime.

The precessional flow mobility expression yields a value of α close to 0.05 for all samples. This value is acceptable with the small uncertainty (around 10%).

This results in predicting H_w values which are indeed below the fields above which we have been able to perform domain wall speed measurements.

As a result, in all the explored cases, we would see only the precessional regime. The fact that the value of H_w is lower than the value of H we can apply then explains the absence on the experimental curves of steady regime and even the absence of Walker breakdown. Finally, all the data are consistent if relying on this precessional motion hypothesis: domain wall speed leads to reasonable values of α (with limited scattering over different samples) – and the calculated Walker field is also perfectly consistent with the precessional motion hypothesis.

Basically, the Walker breakdown can not be observed to the strength of the pinning on the defects in our layers, too large to allow for domain motion at low magnetic fields.

Noticeably, other groups met the same limitation in other systems, such as Pt/Co/Pt thin films, where the limit applied field H^* was also too high to allow for the observation of domain wall speed below the Walker breakdown [MET 07] (probably due to different pinning defects, as the origin of the anisotropy differs completely in the two systems).

Summary:

Our data have been obtained in the precessional regime, above Walker field.

Our results are consistent with $\alpha \approx 0.05$

The model indeed consistently predicts H_W (calculated) $< H^$ (experimental)*

To support our hypothesis of precessional motion, we also perform simulation of the domain wall velocity as a function of field, with different varying parameter: damping factor α and thickness of FePt. The result of this simulation will be reported in the next part.

4.2.4 Simulation of domain wall motion with perpendicular magnetization

The simulation has been done by using the software developed by Jean-Christophe Toussaint (CNRS Grnoble) named GL_FFT2D.

Input parameters:

- Dimension of the box: 128 a.u.
- Width of the box: thickness of FePt layers.
- Anisotropy value: $4.6 \cdot 10^6 \text{ J.m}^{-3}$
- Exchange constant: $6.9 \cdot 10^{-12} \text{ J.m}^{-1}$

In order to compare with experimental data done by MOKE, we chose the thickness of FePt $t_{\text{FePt}} = 2, 4, 5, 6$ and 8 nm .

- Value of damping factor: $\alpha = 0.02, 0.05, \text{ and } 0.1$.

Results:

a) Position and velocity of domain wall as a function of time at several fields

As said, we carried out simulations for a perfect thin film without any defect inside. Fig. 4.16a and b show the evolution of domain wall position over time and Fig. 4.16c and d of the evolution of the wall velocity over time for several field values. The series presented in Fig. 4.16 are chosen with input parameter: 4 nm FePt and damping factor value $\alpha = 0.1$ as an example.

As presented in Fig. 4.16, the applied field has a strong influence on the wall position and velocity. At low field, (1280 Oe in this case) the wall moves with a constant velocity. With $H_{\text{app}} < H_W$, we are in steady regime now, therefore there is no strong relationship between the wall position and velocity in this regime. In the first $0 - 0.2 \text{ ns}$, the domain wall velocity accelerates and then the motion occurs at a constant velocity.

When increasing the field, for both position and velocity of wall, the movement changes from linear to oscillation. The oscillation frequency increases with the field. At field $> H_W$ we are in the so-called precessional regime. In this one, the behavior of wall position and velocity is oscillatory: the wall goes back and forth, while the velocity attains both positive and negative values, with a certain periodicity (Fig. 4.16d). The domain wall oscillates with an increasing period and decreasing amplitude when the field increases.

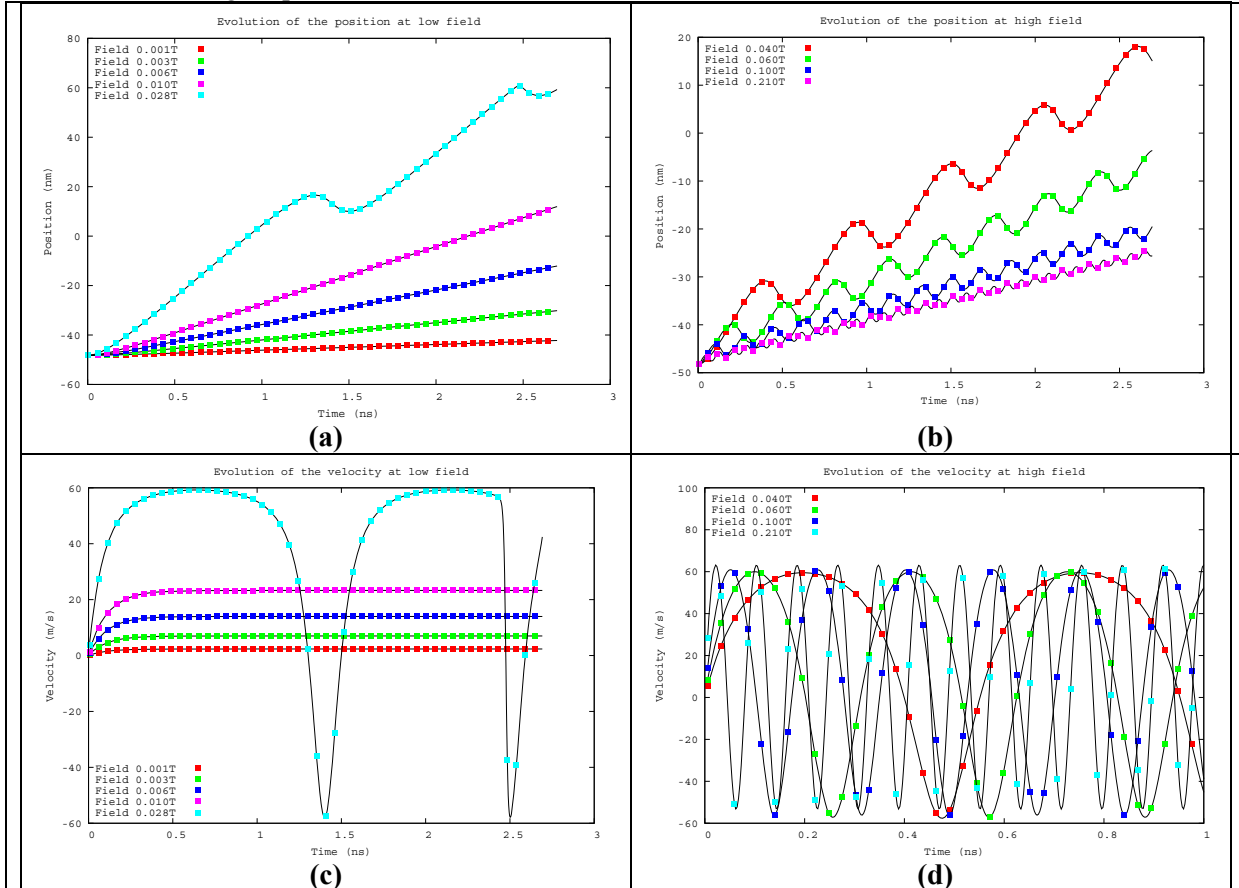
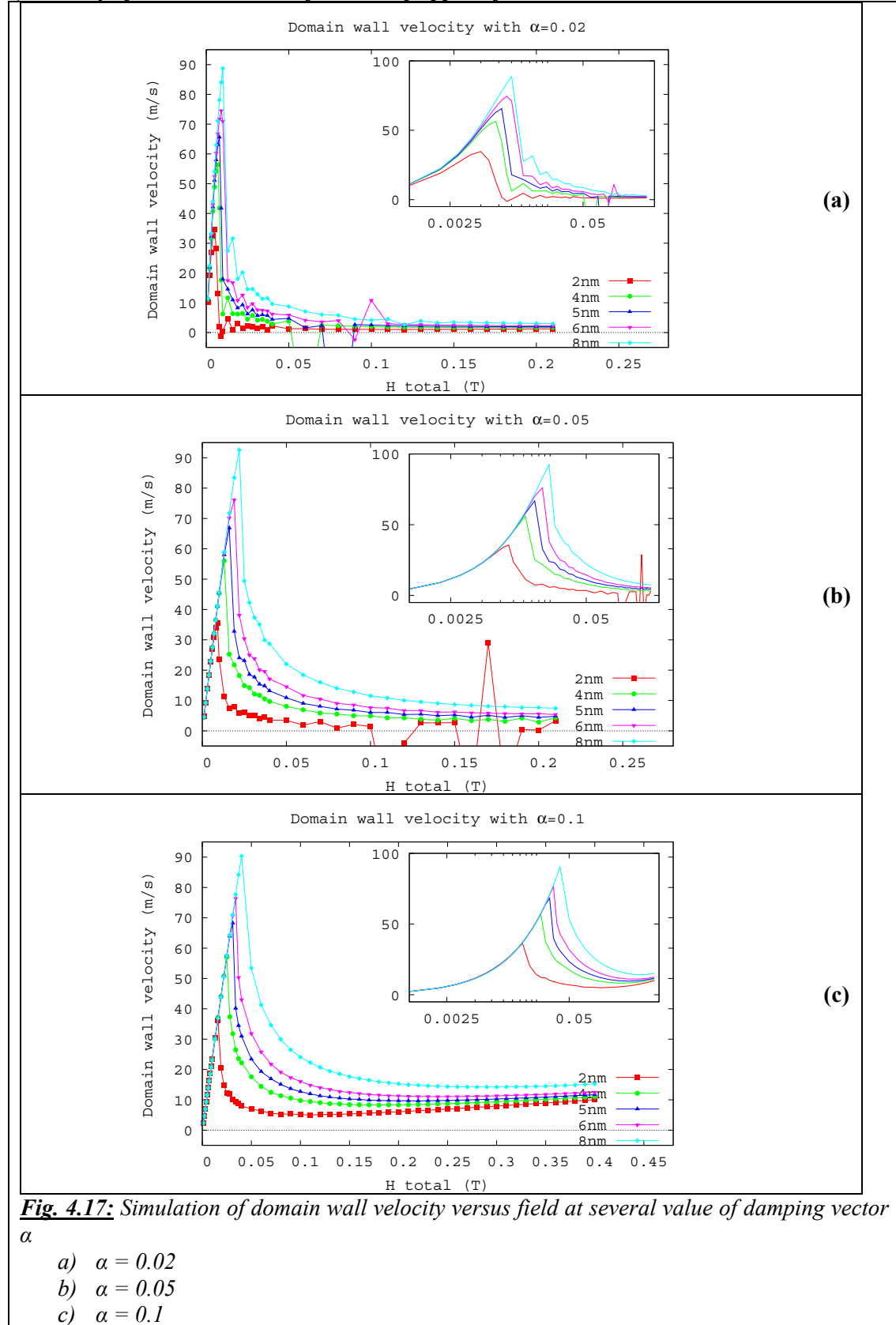


Fig. 4.16: Time evolution of domain wall position and velocity
a) and c): at low applied field
b) and d): at high applied field

b) Velocity of domain wall as a function of applied field

All our results concerning domain wall velocity simulations are presented in Fig. 4.17. This simulation has been done with 3 different values of the damping factor $\alpha = 0.02, 0.05, 0.1$. We can draw some conclusion from these results:

- The behavior of velocity curves is the same for of the different thickness and α : increasing very fast, reaching very high velocity peak ($v \approx 80 - 100$ m/s) and then decreasing. Finally, at a high applied field (> 500 Oe), the velocity becomes nearly constant.
- The domain wall velocity increases with the thickness of FePt layer. We observed this for all the damping factors α .
- The value of H_w also increases with the thickness of FePt layer. This increase is more pronounced when α is larger. The shift of H_w when increasing thickness from $t = 2$ nm to 8 nm is 50 Oe for $\alpha = 0.02$, 130 Oe for $\alpha = 0.05$ and 180 Oe for $\alpha = 0.1$. Moreover, the simulated H_w is small, always less than 400 Oe for all the cases of thickness and α . These results match our analysis of the MOKE data, when we set α to be around 0.05. It seems that the dynamical process we experimentally observe is a thermally activated depinning. The velocity maximum observed on the experimental curve is not a walker velocity that should be far larger. This conclusion is very important because it confirms our hypothesis (Even if the value of domain wall velocity are extracted from simulation performed at $T = 0$ and without defects, as the influence of these parameters should diminish when going above the depinning fields). Then we are fairly confident that our experimental data corresponds to the precessional regime, in agreement with our analysis of the MOKE data. The detailed comparison will be reported after.
- Domain wall velocity increases with damping factor α . However, this dependency is not very strong.

c) Comparison between results of calculation from MOKE data and simulation

With the calculation done with the hypothesis of precessional regime, we found the damping factor is ≈ 0.05 (see part 4.2.4.2). Therefore we have used this value of α to compare our simulations and the experimental data. The values are reported in Table 4.3.

	MOKE data	Calculation from MOKE data with precessional regime hypothesis	Simulation
H_w (Oe)			
2 nm		297	90
4 nm		118	130
5 nm		394	160
6 nm		325	191
Constant velocity after WB(m/s)			
2 nm	~ 14		1.5
4 nm	~ 15		3.4
5 nm	~ 16		4.6
6 nm	~ 19		5.6

Table 4.3: Comparison value of H_w and domain wall velocity with experiment and simulation.

From Table 4.3, we note that the domain wall speed predicted by the numerical simulation is close to the ones we observe experimentally on the plateau (within a factor 2). Beside that, the Walker field derived from the numerical simulation is similarly close to the one derived from the crude formulae giving the velocity. The differences between the simulated value and experiment for the domain wall speed may be linked to the simplified hypotheses done for the simulation: system without any defect and no thermal effect.

4.2.5 Conclusions

From those crude analyses and simulation, we are quite confident that experimental domain wall speeds have been recorded above the Walker field. The reason may be associated with the strong pinning by defects in the FePt layer that prevents domain wall propagation in the low field range and prevents the observation of the creep regime and the Walker breakdown.

4.3 Conclusions

In this study, we have reported on the behavior of domain structure and dynamics in thin films with perpendicular anisotropy.

Observations where done for single FePt layer, we recorded the domain propagation process as a function of both applied field and pulse duration; therefore we derived an in depth description of the domain growth, including “Swiss chess effect” at low field and vestigial 360° winding walls in thick layer.

Beside that, the domain wall velocity has also been measured by MOKE. Our results are supported by magnetostatic calculation and numerical simulation. Simulation results are found to be in good agreement with experimental data. According to our analysis, we believe that only the precessional regime is observed after thermally activated depinning, as the Walker breakdown would occur below the depinning field. This may be due to strong pinning by defects inside the FePt layer: due to the very large magnetocrystalline anisotropy of the alloy, it is indeed expected that structural defects will have a strong pinning effect.

Finally, experimental data can be described by using a reasonable value of the damping factor for FePt $\alpha = 0.1$, which describes the dissipation occurring during flow motion. Even if this is an indirect measurement of the damping factor α , we believe it to be in the correct range. It needs to be confirmed in the future by experimental measurement, for example by FMR.

In conclusion, we have experimentally and by simulations obtained the complete velocity-field characteristics of domain-wall motion in FePt thin films as well as in MTJ. Similar studies have been reported in many papers before for example [KIR93], [MET07], [WIE06], but for different high anisotropy perpendicular thin film: what separates our results from previous study on thin films is that we have been able to observe the thickness dependence of the velocity curves as a function of applied field: this is the first time one obtain the full view of velocity-field characteristics of domain-wall motion in thick sample from 2 to 6 nm.

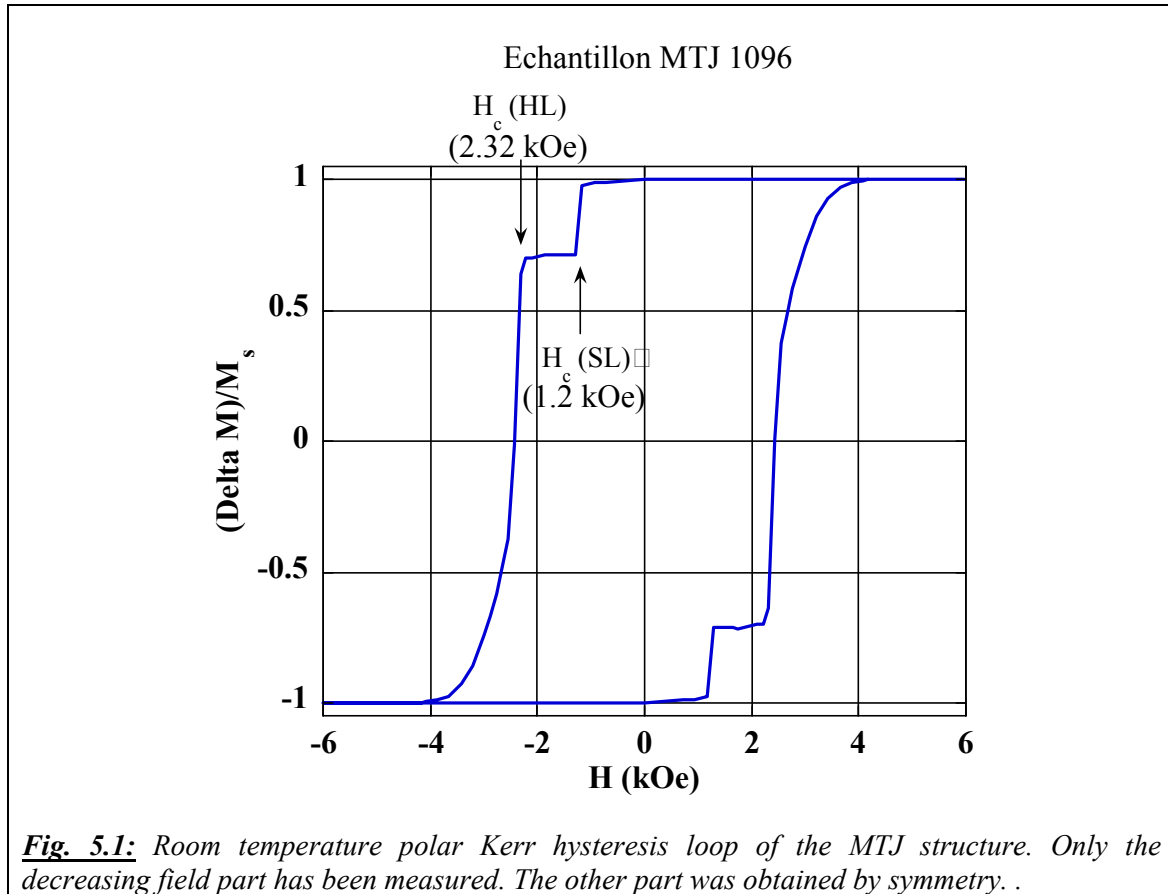
5 Magnetization dynamic and DW motion in FePt/MgO/FePt MTJ

5.1 Study on propagation of magnetic domain walls in MTJ sample

In this part, we study the dynamic of the propagation of magnetic domains in the full MTJ stacking. We use the PMOKE system from the “Laboratoire de Physique des Solides” (LPS) in Orsay (France) for recording images. The stackings are the following:

$$\text{MgO}_{\text{substrate}}/\text{Cr}_3 \text{ nm}/\text{Pt}_{60 \text{ nm}}/\text{FePt}_{5 \text{ nm}}/\text{MgO}_{2.5 \text{ nm}}/\text{FePt}_{10 \text{ nm}}/\text{Pt}_{10 \text{ nm}}$$

The hysteresis loop is shown in Fig. 5.1. It was obtained by measuring the amplitude of the magneto-optical signal for negative value of the field. We measured the magneto-optical signal only for negative field values; the part of the curve corresponding to positive field values has then been deduced by symmetry. The field sweep rate is ≈ 50 Oe/s. In Fig. 5.1, we can determine the coercive field for the soft layer $H_c(\text{SL}) = 1.20$ kOe and the coercive field for the hard layer which is $H_c(\text{HL}) = 2.32$ kOe. The reversal of the soft layer is very square. The saturation field is higher than 4.1 kOe (compare to the Fig3.6, the coercive fields values are different because samples are not the same and we know that the coercive field may differ strongly from sample to another.).



5.1.1 Applying field around the first reversal

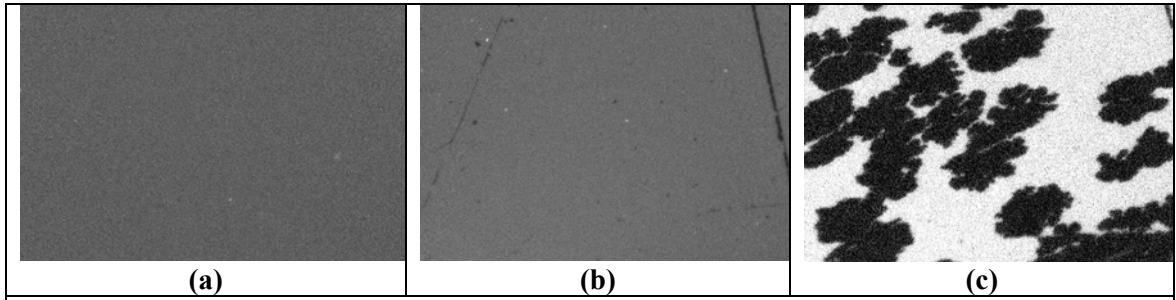


Fig. 5.2: PMOKE images obtained from magnetic configurations under low fields

- a) after an applied field $H = 1105$ Oe during $\Delta t = 2$ s.
- b) after an applied field $H = 1159$ Oe during $\Delta t = (2 \text{ s} + 10 \text{ s})$.
- c) after an applied field $H = -1440$ Oe during $\Delta t = 0.5 \mu\text{s}$

Size of images: $54.0 \mu\text{m} \times 48.6 \mu\text{m}$ for (c) and $57.5 \mu\text{m} \times 49.9 \mu\text{m}$ for (a) and (b).

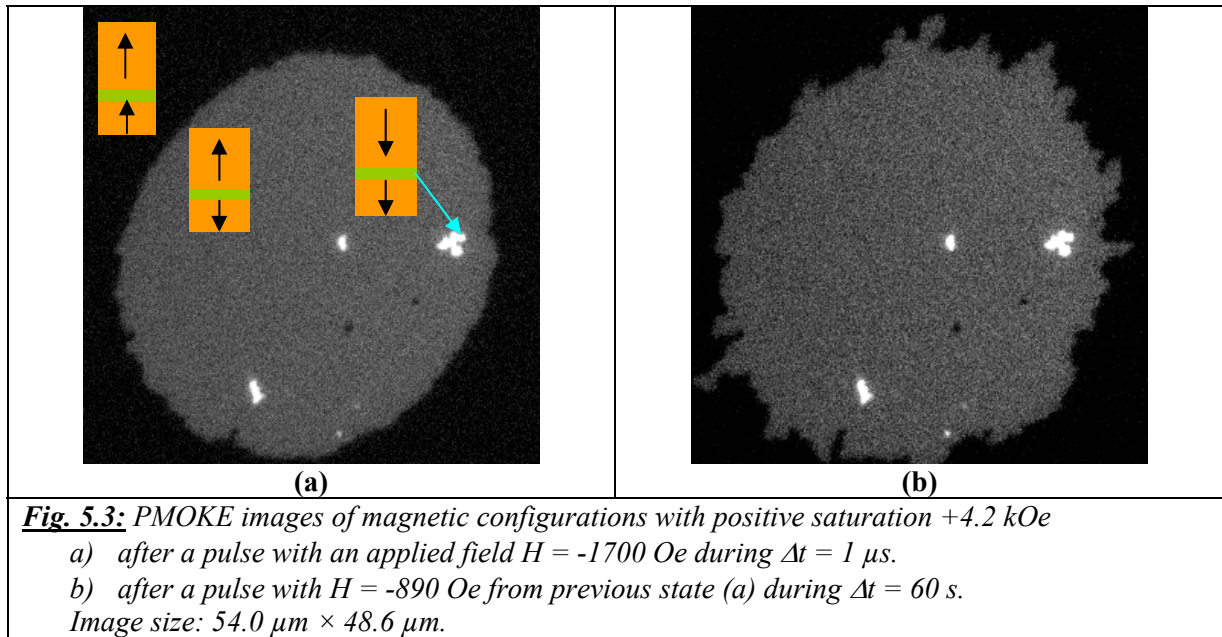
In this part, we study the process of propagation beginning with the behavior the soft layer. From the hysteresis loop in Fig. 5.1, we noted that the reversal field for the soft layer is 1.2 kOe, but this value actually comes from a quasi-static measurement. This value is expected to depend on the field sweep rate as thermal activation plays a role in magnetization reversal, and hence the reversal field can be significantly different when applying very short pulses. Nevertheless, this quasi-static value gives a lower bound of the dynamic reversal field.

Starting by applying a low field $H = 1105$ Oe during 2 s after having saturated the sample (saturation with a negative applied field), the Fig. 5.2a shows that nothing has happened yet. The field 1105 Oe is not enough for the magnetization reversal process to start. Coming back to the saturated state and then applying a slightly higher field than the previous value (54 Oe more) during a longer time, we can see that the propagation begins with a few reversed domains (black parts) but they are very small (actually in the 0.3-0.5 μm range). The start of the propagation may occur in Fig. 5.2b with two lines near the border, but such lines may come from small scratches on the surface of the sample. We continue to increase the field up to 1440 Oe (with a symmetric experimental process: positive saturation and then negative field pulse (just during $\Delta t = 0.5 \mu\text{s}$)).

All the changing of domain walls of the soft layer is then presented in Fig. 5.2c. All the images were taken at the same position (except for thermal and other drifts), therefore, we still see the propagation of the crack defect comparing to Fig. 5.2b. Also in Fig. 5.2c, we notice a preferred direction of the propagation, around 45° for all the domains. The preferred direction is due to either the stress of thin film on MgO substrate during the epitaxy growth or the axis is not being not on the perpendicular axis of the film. This preferred direction is confirmed later in the part 5.1.4.

Summary:

We can have a small conclusion here, about the behavior of two soft and hard layers. We observe domain wall propagation in the soft layer while no magnetization reversal takes place in the hard layer. This behavior is favored by the “low” field intensity (less than $H = -1440$ Oe) which positions the sample just after the first reversal, as shown on the hysteresis loop of Fig. 5.1.



Under higher fields, the domain wall behavior suddenly changes. In Fig. 5.3, we observed the elliptic domain (grey color) under a field $H = -1700 \text{ Oe}$ after a pulse during $\Delta t = 1 \mu\text{s}$. This elliptic domain is the domain of the soft layer. The very new information taken in this image is the appearance of white dots just after the very short pulse ($\Delta t = 1 \mu\text{s}$). These white dots, inside the \downarrow state domain of the soft layer, correspond to reversed domains in the hard layer. It means that, in this dynamic process, the nucleation of the hard layer occurs at a lower field than the static macroscopic reversal field determined from the hysteresis curve. The reason for this phenomena comes from the dipolar effect coupling the soft layer and the hard layer as it will be explained later (more precisely, it comes from the stray field from the soft layer and plus the externally applied field).

once the domain wall is further propagating in the soft layer (as new field pulses are applied), it is remarkable to observe that the domain appeared in the hard layer do not evolve because the total field acting on the hard layer (sum of the applied field plus the stray field from the soft layer) is much smaller than the propagation field.. As a result, the dipolar field created far from the domain wall is too low to have a significant effect on the hard layer. We will comment further later on this phenomenon. It is confirmed in Fig. 5.3b. We continue from the magnetic state described in Fig. 5.3a, by applying a low field of $H = -890 \text{ Oe}$ during a long period $\Delta t = 60 \text{ s}$. We remark that only the \downarrow state domain of the soft layer expands, while the domains already nucleated in the hard layer from the previous pulse are not modified, either in number or in shape or size.

Nevertheless, the boundary of the domain propagating in the soft layer deeply changes: at low field (890 Oe), after propagation induced by “low-field” pulses, the boundary of the bubble domain in the soft layer is rough, while it is smooth after “high-field” pulses. It is clear that there is a transition between rough and smooth boundary, due to the value of applied field.

When the field passes to the coercive field of the soft layer, the soft layer is completely reversed as shown in black in Fig. 5.4. Beside that, Fig. 5.4 shows also many small white dots which are nucleated domains in the hard layer. They appear very early before the macroscopic reversal of the hard layer. The importance and behavior of these white dots will be stressed in the next part.



Fig. 5.4: PMOKE image of the magnetic configuration after a field pulse: $H = 1.803$ Oe during $\Delta t = 2$ s.
Size of the image: $57.5 \mu\text{m} \times 49.9 \mu\text{m}$.

Summary:

In this part, the first time we observed nucleation of the hard layer just at the applied field $H = -1700$ Oe and then they didn't expand anymore even when we increase the applied field. An explanation will be given later.

5.1.2 Applying field between reversal of the soft layer and of the hard layer

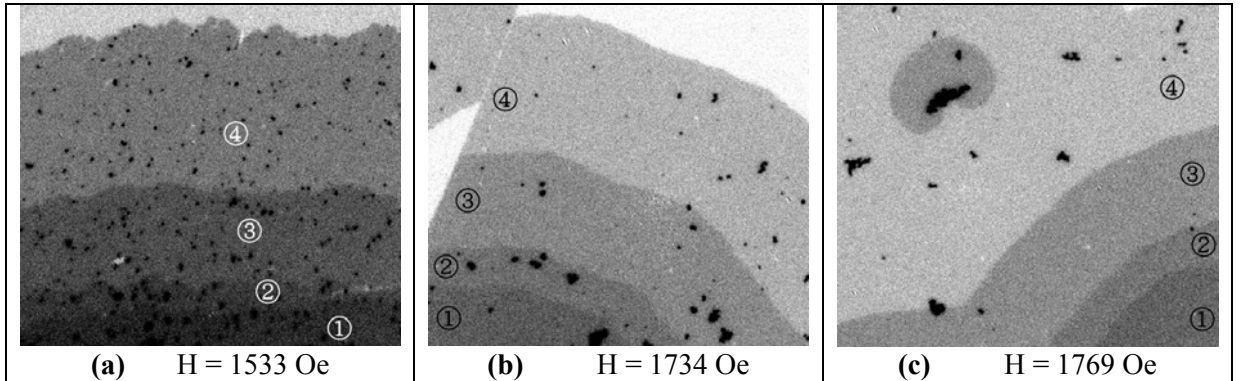


Fig. 5.5: PMOKE images showing the propagation of the soft layer and nucleation of the hard layer after different field pulses. For all the images, the indicated fields were applied during $\Delta t = (0.3 + 0.8 + 1.2) \mu\text{s}$

Area (1): nucleation centre.

Area (2): after applied pulse during $0.3 \mu\text{s}$ from the state (1)

Area (3): after applied pulse during $0.8 \mu\text{s}$ from the state (2)

Area (4): after applied pulse during $1.2 \mu\text{s}$ from the state (3)

Image size: $54.0 \mu\text{m} \times 48.6 \mu\text{m}$.

For all the cases from Fig. 5.5a to c, the fields we applied now are larger than 1500 Oe, enough for the soft layer to start reversing. So we can observe the process of the propagation of the soft layer in grey color. The domain wall of the soft layer on each image develops from the nucleation in the corner of images: right corner for Fig. 5.5a and c, left for Fig. 5.5b at the position call (1) in the images. The areas (2), (3), (4) correspond to the areas successively reversed after the application of each field pulse (field pulses are applied starting each time from the magnetic configuration resulting from the previous one, without returning to saturation). The first pulse duration is $0.3 \mu\text{s}$ and reversed area (2), the second pulse ($0.8 \mu\text{s}$) area (3) and the

third pulse (1.2 μ s) area (4). We conclude that the propagation of the soft layer domain wall proceeds in a continuous way, with a stable direction from the nucleation corner. The borders of all domains in this field range are smooth, as the applied fields are in the stable region in the domain wall velocity curve. At low field (1533 Oe), the border of domain is rough as the disorder within the layer can play a significant role. At a higher field (> 1734 Oe), the domain wall roughness vanishes.

On all those images, we can see blacker dots appearing during the propagation process. We would like to emphasize 3 important points based on these 3 images:

- The number of black dots decrease when we increase the applied field from image a to c.
- The size of black dots don't change (the visible changing comes from different contrast of images).
- The black dots only appear inside the domain of the soft layer.

The black dots denote nucleation in the hard layer, in spite of an applied field still smaller than $H_{C(HL)}$. The question now is how nucleation in the hard layer can occur? We already briefly suggested an explanation, based on the combination of the stray field from layer to another one and the applied field.

An analytical calculation (using an arctangent profile for the domain wall and translational invariance along the domain wall) of the stray field is shown in Fig. 5.6 at 8 nm above the surface of the soft layer; a distance corresponding to the middle of the hard layer. When the domain wall in the soft layer is propagating, the stray field created from the soft layer added to the applied field favors nucleation in the hard later in the close vicinity of the domain propagating in the soft layer. Then, we account for the observed nucleation events in the hard layer, behind the domain wall in the soft layer.

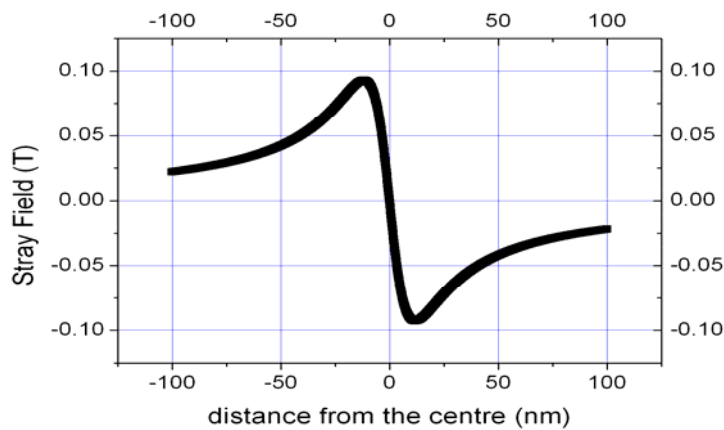
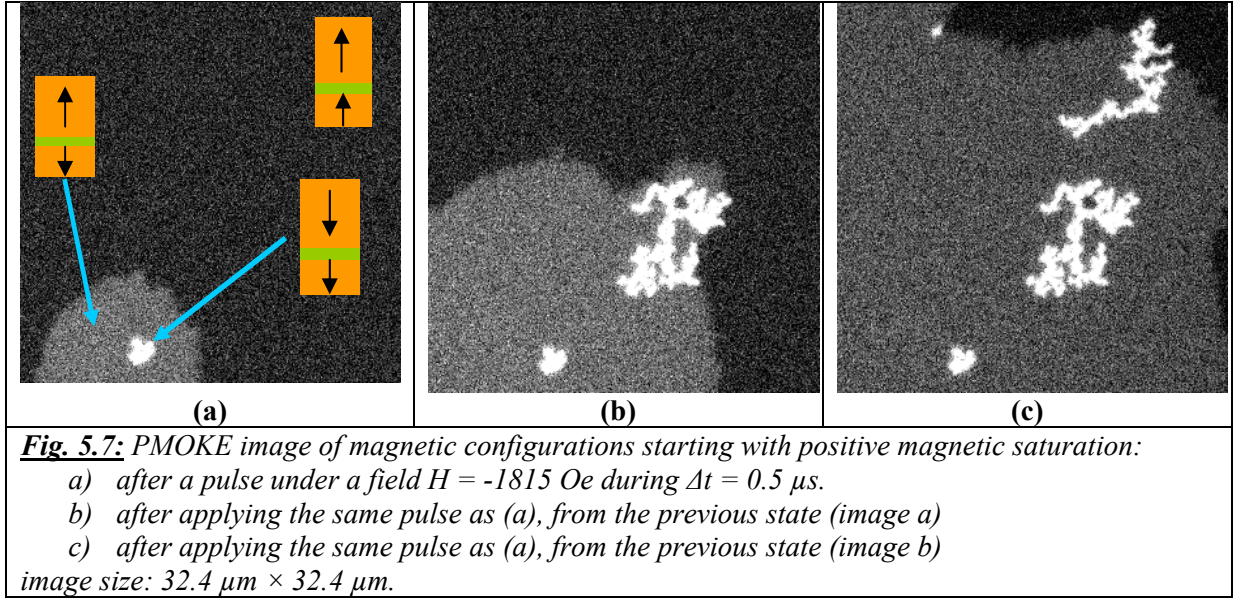


Fig. 5.6: magnetic stray field created above the domain wall in the soft layer within the hard layer.

When we increase the applied field, we also increase the DW velocity. As a result, the wall stray field (above the domain in the soft layer) combines during shorter time with the applied field over a given part of the hard layer. Magnetization reversal being a thermally activated

event then occurs less often at higher field. A certain pulse duration and field magnitude is needed to reverse the magnetization.

To understand well the nucleation occurring in the hard layer, we did some further experiments to confirm this phenomenon at higher field (Fig. 5.7). The sample was first saturated with a positive field under +4100 Oe, giving thus a \uparrow state to the soft layer and also a \uparrow state to the hard layer. Then a first pulse was applied under a field $H = -1815$ Oe during $\Delta t = 0.5 \mu s$. Without returning to saturation, a second pulse was applied from the previous state, and finally the same during a third pulse.



In Fig. 5.7, under an applied field $H = -1815$ Oe, and after several pulses, the grey domain we observe corresponds to the \downarrow state of the soft layer. It develops as usual expanding its size. After each pulse, some white domains appear near the borders of the domain of the soft layer. But as soon as they are situated in the middle of soft layer reversed domain, they don't evolve any more. This is demonstrated by the white domains (reversed part of the hard layer) located within the area already reversed in the soft layer: these no longer evolve with new pulses (see Fig. 5.7b and c).

As discussed before, nucleation events in the hard layer (white domains) only appear inside the area corresponding to the \downarrow domain in the soft layer. After the third pulse, the system has been left in the magnetic state under the field described by Fig. 5.7c during 40 minutes without any visible evolution or change.

It is interesting to notice that - since the applied field during the pulse is larger than the propagation field of the soft layer - we obtain a compact shape domain (bubble) in this layer. Conversely, the domain in the hard layer presents overhangs, certainly induced by defects encountered during its propagation. As could have been expected, the applied field should be much more important to obtain domains with a compact shape in the hard layer.

From now, we increase the field close to the static reversal field of the hard layer. Starting from the negative saturation (\downarrow state for soft layer and \downarrow state for hard layer also), we applied a high amplitude field $H = 1923$ Oe during $0.3 \mu s$. In Fig. 5.8a, the pulse creates two types of domains: the grey one and the black one. The grey one is a \uparrow state domain of the soft layer which has fully flipped in bubble in this case. The \uparrow state domains of hard layer in black color have

overhangs shape with several bifurcations coming from a common centre, once again to avoid defects. We deduce that the growing of this \uparrow state domain of the hard layer has been dendritic during the growth of the bubble \uparrow state of the soft layer.

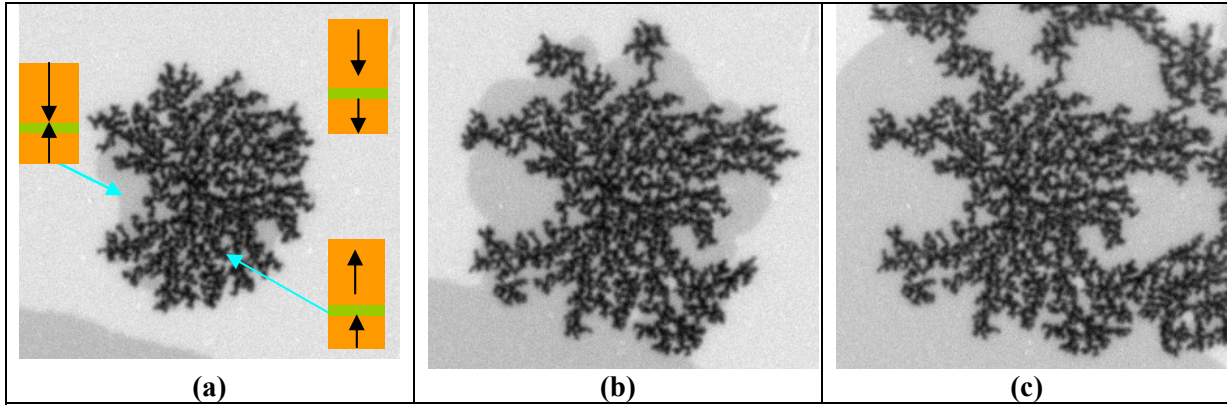


Fig. 5.8: PMOKE for sample FePt starting with negative magnetic saturation.

- a) after a pulse under applied field $H = 1923$ Oe during $\Delta t = 0.3 \mu s$.
- b) after applying the same amplitude pulse as (a) during $\Delta t = 0.1 \mu s$, from the previous state (image a).
- c) after applying the same amplitude pulse as (a) during $\Delta t = 0.2 \mu s$, from the previous state (image b).

Image size: $32.4 \mu m \times 30.2 \mu m$.

After applying the same pulses during $0.1 \mu s$ and $0.2 \mu s$ more, the expansion in the domain of the hard layer is clearly visible. It still has a dendritic shape, and it has expanded its size following the development of the soft layer, as homogeneously as before. The domain wall propagating in the hard layer never precedes the domain wall in the soft layer. This is a further indication of the key role of the stray field created by the domain in the hard layer to assist magnetization reversal in the hard layer. As in the previous case, the branches of the black domain of the hard layer which are disconnected from the bubble wall of the \uparrow state of the soft layer (*i.e.* left behind the domain wall in the soft layer) don't evolve any more. As explained before, this disconnection comes from the inhomogeneous magnetic properties of the sample: the domain of the hard layer follows the easiest path for propagation.

5.1.3 Around the second reversal: 2.32 kOe

In this situation, the field is larger than the reversal field of the soft layer (which is around 1200 Oe), so the soft layer is completely reversed with the \downarrow state in grey color (as for previous experiments, we started from \uparrow state for both layers). From the quasi-static magnetic data, a field $H = -2118$ Oe (as shown in Fig. 5.9a) is not enough to induce magnetization reversal of the hard layer. However, we notice some small white domains corresponding to nucleation in the hard layer after a pulse $\Delta t = 20$ s. The explanation for that, as suggested before, comes from the superimposition of the stray field from the soft layer and of the externally applied field.

We continue to increase the field to follow the magnetic process of the hard layer from Fig. 5.9b to e. Fig. 5.9b is obtained under the field $H = -2278$ Oe during $\Delta t = 50$ s from the previous state (Fig. 5.9a). We observed the beginning of propagation from some previous nucleation events. The next image in Fig. 5.9c corresponds to a switch to a positive field $H = 2303$ Oe (with positive reference also) during $\Delta t = 20$ s. It is worth noticing that while the field value in this

case is a bit lower than the coercive field of the hard layer, the \downarrow state domains of the hard layer created during the previous state, are still in the same position, and don't evolve at all, even don't expand any more. After a higher field $H = 2990$ Oe applied during $\Delta t = 50$ s as shown in Fig. 5.9d, the white \downarrow domains of the hard layer become thinner and thinner, and finally disappear in the last image (see Fig. 5.9e), higher field values such as $H = 3463$ Oe being effective even over shorter durations $\Delta t = 1$ s.

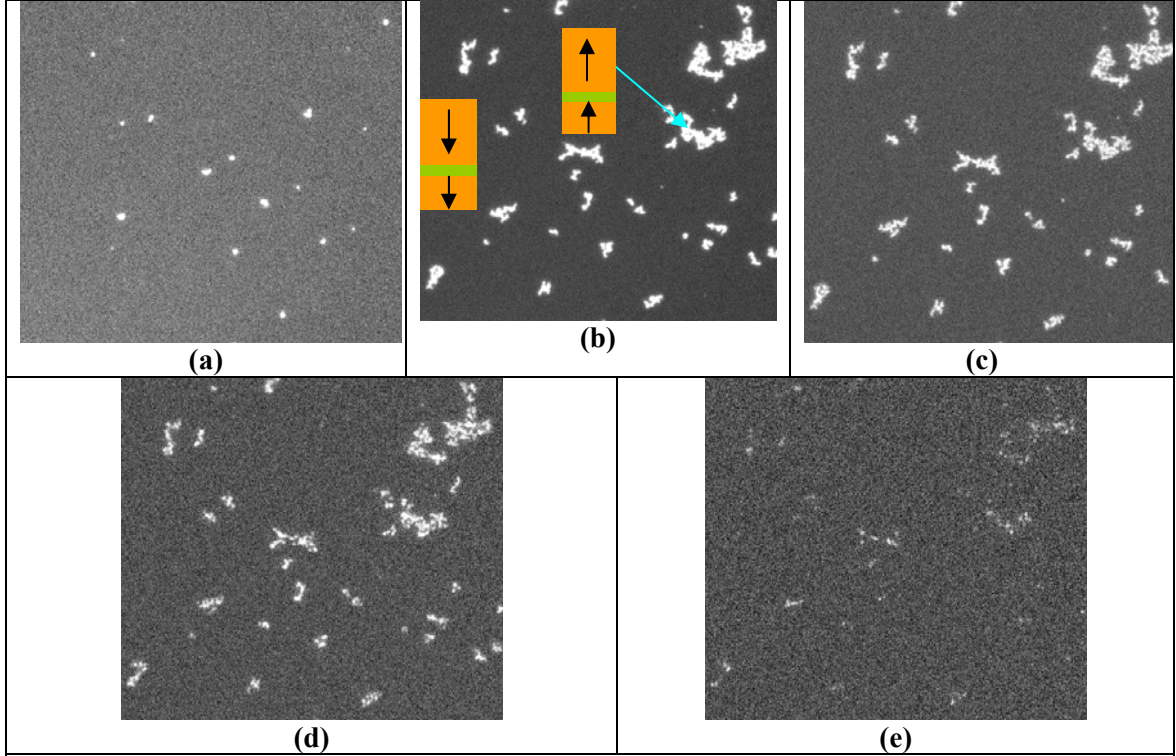


Fig. 5.9: PMOKE images for magnetic behaviors of the hard layer.

- a) after an applied field $H = -2118$ Oe during $\Delta t = 20$ s.
- b) after an applied field $H = -2278$ Oe during $\Delta t = 50$ s.
- c) after an applied field $H = 2303$ Oe during $\Delta t = 20$ s.
- d) after an applied field $H = 2990$ Oe during $\Delta t = 50$ s.
- e) after an applied field $H = 3463$ Oe during $\Delta t = 1$ s.

All the images were taken with positive magnetic saturation as starting configuration.

Image size: $54.0 \mu\text{m} \times 48.6 \mu\text{m}$.

5.1.4 Demagnetization

The purpose of demagnetization experiments is to gain understanding of the magnetic patterns created by dynamic processes. The ac-demagnetizing field was applied to our sample starting from 2 different amplitudes: ± 4.2 kOe and ± 1.5 kOe as shown in Fig. 5.10a and b. The demagnetization is done through a decaying oscillation. The variation of the amplitude is done through small steps of 230e during 5ms.

From the hysteresis loop in Fig. 5.1, we remind that the quasistatic saturation field for our sample is ≈ 4.1 kOe. The ac-demagnetized state as shown in Fig. 5.10a presents very tiny \uparrow (white) and \downarrow (black) domains. The shapes of the domains highlight a ribbon-like domain structure. We can approximately conclude that the number of \uparrow and \downarrow domains is the same.

Another experiment under a field of ± 1.5 kOe is shown in Fig. 5.10b. There are 3 types of contrast in this image:

- grey domains: corresponding to the \uparrow state of the soft layer;
- black domains: associated to the \downarrow state of the soft layer;
- white dots.

For the soft layer, the number of $S\uparrow$ (grey) and $S\downarrow$ (black) is not balanced; it is due to the relatively small value of applied field (± 1.5 kOe). Beside that, in this image, there is exactly the same phenomenon we observed in the Fig. 5.2c when studying propagation of the soft layer: the preferred direction ($\approx 45^\circ$) for all the domains of the soft layer. The explanations presented in that part are still valid for this case: either the stress of thin film on MgO substrate during the epitaxy growth or the axis is not strictly along the perpendicular axis of the film. This second experiment confirms clearly a preferred direction for the growth of the domains.

Coming back to the domains of the soft layer, the measurements of the width of the black domains give about $2\ \mu\text{m}$ and a length of $10\ \mu\text{m}$.

Concerning the white dots we compared the optical intensity of all the domains. The intensity of the black domains (down domain of the soft layer) is around 100 and the grey domains (up domain of the soft layer) in the range of 500. The one of the brighter white dots is 1180. The big difference between the intensity of white dots and the others confirms rules out any artifacts induced by the camera or the software (contrast threshold, subtraction of pictures). It clearly confirms the reality of these white dots. It is interesting to notice that the white dots only appear in the black domains (but not inside the grey domains).

The sample is saturated at -4.5 kOe and then demagnetized with a decreasing oscillating field with maximum amplitude of 1.5 kOe. These white dots are certainly up domain of the hard layer. The fact that we only observe them in the black (down) domain of the soft layer is because they are stabilized by the stray field.

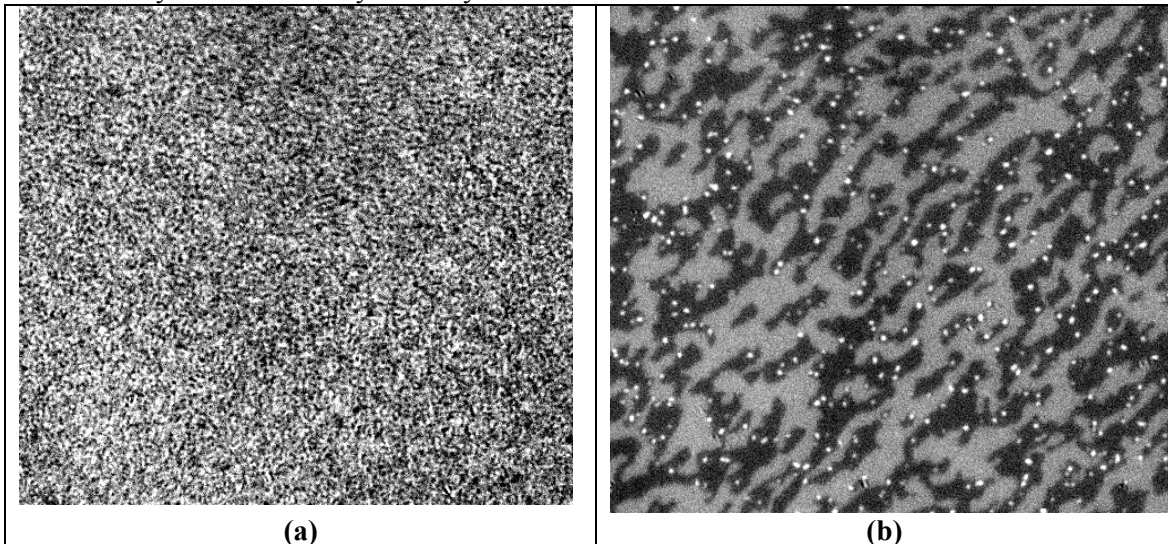


Fig. 5.10: PMOKE images of ac-demagnetizing.

a) after demagnetizing with an amplitude field $a = \pm 4.2$ kOe

b) after demagnetizing with an amplitude field $a = \pm 1.5$ kOe

size of images: $54.0\ \mu\text{m} \times 48.6\ \mu\text{m}$

Summary:

We once again observed the nucleation of the hard domain inside the soft layer domain with the same explanation involving the stray field coupling the two layers.

5.1.5 Conclusion

This part presented a full view of the propagation processes in the soft and hard layer in the MTJ, as well of the way domain wall propagation processes in the soft layer coupled to the magnetization in the hard layer. The time and field dependence of the magnetic domain structure were investigated by MOKE in FePt/MgO/FePt MTJ sample with perpendicular anisotropy.

We proposed physical origins for some unexpected behaviors. For instance, nucleation events in the hard layer appear before applying the field required to reverse magnetization in the hard layer (in quasistatic experiments). We believe that the results presented in that part illustrate the crucial role of the stray field above the domain wall propagating in the soft layer. It induces nucleation events in the hard layer. We have shown that the velocity of the domain wall plays also an important part via the magnitude of the applied field. Indeed the stronger the applied field the faster the domain wall propagates. However this shortens the duration when this stray field may interact with areas having weak nucleation field in the hard layer. Hence it explains the decrease of the nucleation events in the hard layer when the applied field is increased.

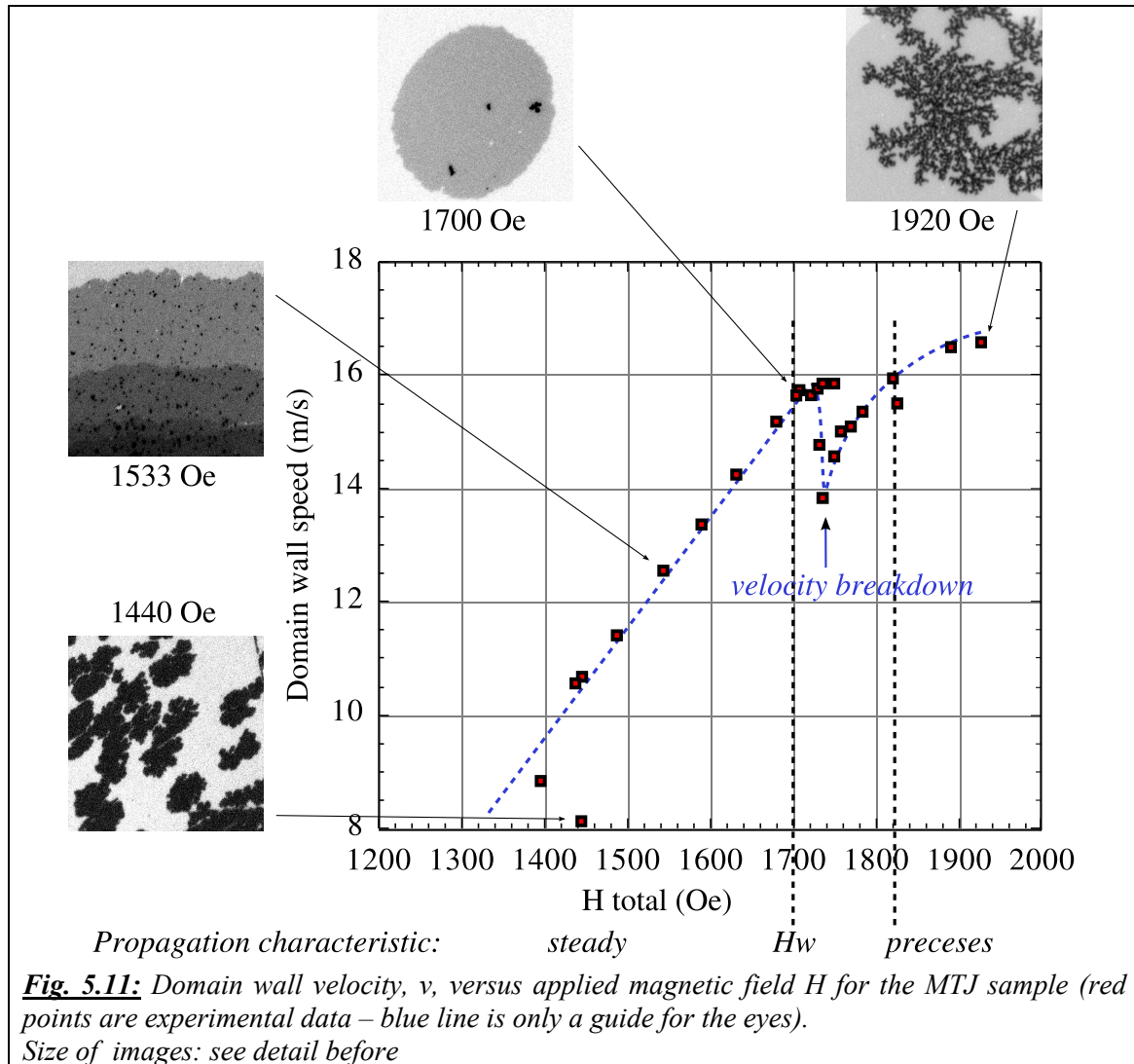
When the applied field is even stronger nucleated domains in the hard layer also propagate. However, it is a thermally activated propagation leading to the observation of dendritic patterns.

5.2 Study on domain wall velocity in MTJ sample**5.2.1 MOKE results for domain wall velocity in MTJ sample**

The first experiment concerns MTJ sample with the structure:

$$\text{MgO}_{\text{substrate}}/\text{Cr}_3 \text{ nm}/\text{Pt}_{60 \text{ nm}}/\text{FePt}_{5 \text{ nm}}/\text{MgO}_{2.5 \text{ nm}}/\text{FePt}_{10 \text{ nm}}/\text{Pt}_{10 \text{ nm}}$$

The hysteresis loop was presented before (see Fig. 5.1), the coercive field for the soft layer $H_c(\text{SL}) = 1.20 \text{ kOe}$ and the coercive field for the hard layer which is $H_c(\text{HL}) = 2.32 \text{ kOe}$.



The result of experiment $v(H)$ curve for domain wall velocity as a function of applied magnetic field, presented for MTJ sample, is shown in Fig. 5.11.

The velocity cannot be measured below 1380 Oe. It is due to the ramified structure of the domain wall below this field ($v = 8.6 \pm 2$ m/s for the lowest field). The measured values of velocity are presented in red square and the blue line is a guide to the eye. The last values at high field (> 1820 Oe) result from measurements got by starting from a certain wall position and reversing propagation. This last data point is not reliable because then nucleation and, subsequently, propagation occurred in a large part of the sample, so only one data could be obtained and even with a dramatic error bar. Data below 1824 Oe are obtained with one coil, while data above that value are measured by adding the field of the electromagnet.

The value 1385 Oe is a critical field characterizing the pinning force acting within the soft layer on this double layer). According to [MAL79], at zero temperature, a law $V(\text{m/s}) = (H - H_{\text{crit}})^\beta$ should be observed, with a $\beta < 1$ exponent ; here due to pinning centers from the intrinsic disorder of the layer prevents free movement of the domain wall. We are in a similar situation.

The $v = f(H)$ curve (see Fig. 5.11 in the 1440Oe - 1920Oe range) displays only the high field part of the preceding law, as domain wall speed is not measurable at lower fields.

Around $H = 1700$ Oe, a breakdown occurs on the curve. In a 1st part of experiment curve (at low field < 1820 Oe) we got a dip and a change of slope; in a 2nd part of the curve (at higher field > 1820 Oe), one got only a change of slope (3 last points). The striking feature in a first part of experiments was that an increase of the field value around 1727 Oe to 1734 Oe was sufficient to get a strong change of the velocity from 15.76 to 13.83 m/s. After the breakdown, the domain wall speed seems to increase again, but with a reduced slope over field

From the first look into the curve, we have the impression that the breakdown at 1700 Oe looks like the Walker breakdown which separate the two regimes of the velocity curve: steady regime and precessional regime. However, the data need to be analyzed to confirm this impression. We will report the analysis later.

5.2.2 Comparison between MTJ sample and 5nm MTJ sample

The FePt 5nm sample presents the hard layer in the MTJ sample. Therefore it is interesting to compare the behaviors of these samples.

In FePt 5nm sample, we do not see a velocity breakdown as for the MTJ sample. In the MTJ, the propagation velocity curve has some similarity with this 5nm single layer sample, since it shows also a trend towards an asymptotic velocity of the order of 17 to 18 m/s and below 1.3 to 1.4 kOe the system looks also as "freezing" the propagation of the domain wall. But we also clearly observe many different behaviors on the velocity curve from those two cases. Indeed, the different threshold field 1.95 kOe (in single sample) compared to 1.4 kOe (in MTJ sample) can probably be understood from the magneto-elastic different characteristics of the 2 samples or from dipolar effects in the case of the bilayer sample.

The key data extracted from velocity curves $v(H)$ in MTJ sample and single sample 5 nm FePt are shown in Table 5.1.

	MTJ sample	Single sample
Field range accessible during the experience	1385 Oe – 1950 Oe	1950 Oe – 3000 Oe
Speed Range	8 – 16 m/s	7 – 17 m/s
Velocity breakdown	1700 Oe	No
Regime before the breakdown within the breakdown after the breakdown	$H < 1700$ Oe 1700 Oe $< H < 1775$ Oe $H > 1800$ Oe	Data is above WB

Table 5.1: The different of velocity curve $v(H)$ between MTJ sample and single sample.

The observed differences may be associated with the presence of the hard layer in the MTJ sample. It not only acts as a reference layer for MTJ but also influences directly the soft layer through the stray field, and possibly magneto-elastic effects.

5.2.3 Analysis of the experimental results of DW propagation in MTJ

We will start our analysis by taking the assumption that the velocity break we observe at $H = 1700$ Oe on Fig. 5.11 is indeed a Walker Breakdown (WB). Theoretically, the WB marks, in the curve $v(H)$, the end of the steady regime of propagation. In Fig. 5.11, we clearly observe a linear regime below the velocity breakdown at 1700 Oe. At higher field the theory predicts that we should observe a second linear flow that corresponds to the precessional flow. However, the second linear regime was not clearly measured above 1800 Oe. The details of those regimes are shown below:

i) At low field $H < 1700$ Oe, the domain velocity varies exponentially with the applied field H , with is due to the thermally activated “jumplike” domain wall motion (see also in [KIR93]). We evidenced directly a “jumplike” type of motion: the DW moves by short jumps. In this case, the velocity follows the formula (5.1):

$$v = v_0 \exp\left[-(E_p - 2HM_s V_B) / k_B T\right] \quad (5.1)$$

Where E_p is the activation energy for domain wall propagation, v_B is the activation (Barkhausen) volume. Compared to the theoretical curve [MET07], we call this regime the steady regime. In this regime, below Walker breakdown with at the field H_W the domain-wall motion is steady with the mobility given by: $m = \gamma\Delta/\alpha$ where $\gamma = 1.76 \times 10^7$ (Oe.s)⁻¹ is the gyro magnetic ratio and α is Gilbert damping vector. Since that, steady velocity is calculated by:

$$v = (\gamma\delta / \alpha)H \quad (5.2)$$

with the value of δ was presented before (4nm)

ii) For higher field, at the regime between $1700 \text{ Oe} < H < 1775 \text{ Oe}$, the behavior of $v(H)$ curve change. It is not linear anymore because the balance of the steady regime is lost here. According to theory, we are in intermediate regime. The field at which we lose the steady regime is called the Walker field H_W , attributed to the domain wall motion regime. Here, field dependent wall mobility exists over a limited field range beginning at H_W . The pinning effect is the leading behavior of $v(H)$ curve in this case. The value of Walker breakdown is given by formula (5.3):

$$H_W = 2\pi \alpha M_s |N_y - N_x| \quad (5.3)$$

where α is the damping factor and $M_s = 1100 \text{ emu.cm}^{-3}$ for FePt.

iii) Above $H = 1800$ Oe, theoretically, we should observe the second linear regime, which is called the precessional regime. However, when doing the experiment, we can not go further than $H = 1924$ Oe, as explained before, because of nucleation.

We have followed this hypothesis in order to calculate α and H_W from our data. By extracting the value of DW velocity before the breakdown and by applying the formula $v = \gamma(\delta/\alpha)H$ for steady regime, and $V = \gamma\delta/(\alpha+\alpha^{-1})H$ for the regime above the Walker breakdown. The fits are shown in Fig. 5.12 and the value of α and H_W are shown in Table 5.2

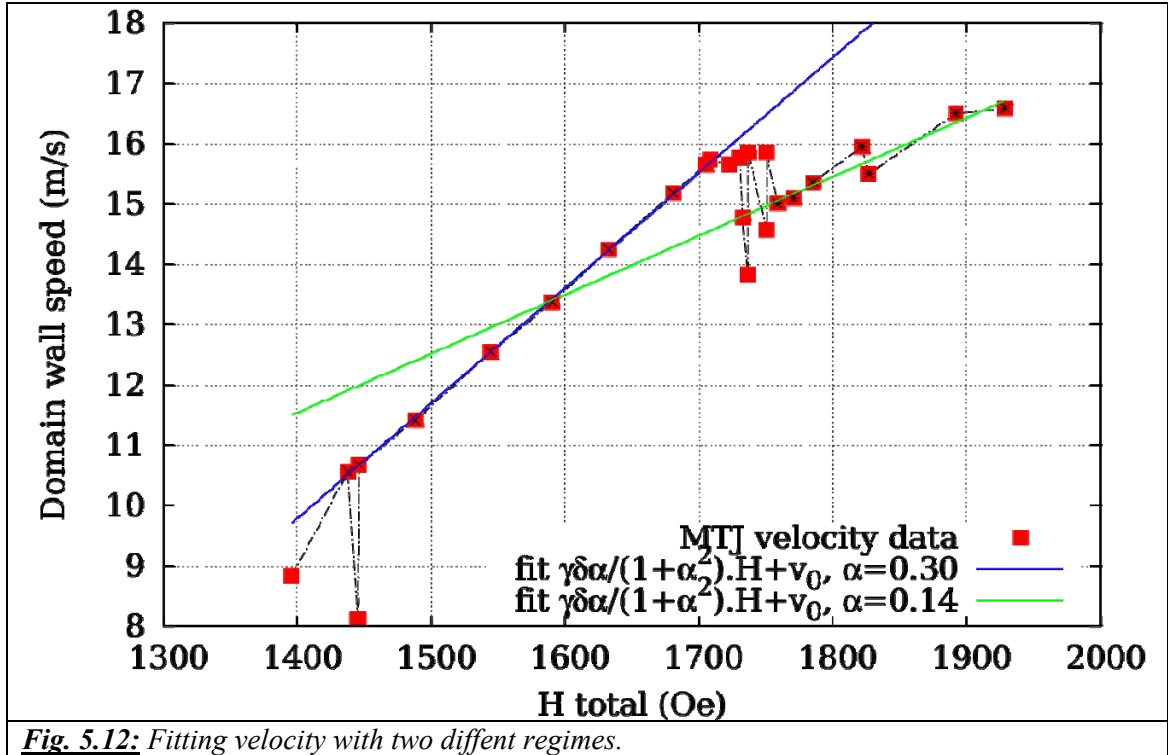


Fig. 5.12: Fitting velocity with two different regimes.

regime	Mobility m (m/(Oe.s))	V_0	α	Uncertainty of α
Below Walker Breakdown	0.008	-17.0	3.7	+/-0.04 (1.1%)
Above Walker Breakdown	0.009	2.1	0.14	+/-0.02 (12.7 %)

Table 5.2: Value of damping factor with the two hypotheses in the steady and precessional regime.

According to the Table 5.2, the value of α in steady regime is much too high, as the same explanation in FePt single: the pinning is too strong for us to follow the steady regime. Therefore the breakdown observed on Fig. 5.11 does not correspond to a Walker Breakdown. It is difficult to apply the precessionnal regime hypothesis to the high field regime because of the lack of experimental data point. Even we can extract the value of $\alpha = 0.14$ but we are not confident because lacking of experimental data point. So we would rather say that we cannot properly extract the damping value α or any other parameters from this set of experiments. The observed regime is certainly a thermally activated regime above the depinning transition. It is quite probable that the Walker Breakdown happens below the depinning transition.

5.2.4 Conclusion

Even if it seems obvious that we observe a steady regime followed by the Walker breakdown, a careful analysis contradicts this assumption. The remaining question is the nature of the velocity breakdown observed on Fig. 5.11.

5.3 Demagnetizing the hard layer by cycling the soft layer

5.3.1 Introduction

One major application for MTJ is in the field of memory devices, such as MRAM. As discussed before, in this structure, the magnetization of each magnetic layer may be in two states: parallel or antiparallel. When the two magnetic layers have their magnetization antiparallel, the resistance R is high because for a given electron spin state in one layer, there are a small number of empty electron states with the same spin in the other layer. Inversely, when they are parallel, the tunneling probability is higher and R is low. These two configurations - parallel (P) and antiparallel (AP) - represent the two states for a bit, 0 or 1. Reading the information relies on a resistance measurement of the MTJ. Writing information corresponds to the reversal of the magnetization of one electrode (the soft one, storage layer) while the magnetization of the second (the hard, reference layer) remains unchanged.

In a memory, the hard layer is used as a reference layer: its magnetization should remain unchanged during the memory life. Let us fix the hard layer (HL) in the up state that we symbolize by an up arrow \uparrow . The two magnetic states of the magnetic junction are then (SL \uparrow /HL \uparrow) and (SL \downarrow /HL \uparrow).

It has been shown in some systems [GID98], [THO00] that hard layer demagnetization may occur through repeated cycling of the soft layer magnetization, even if a short number of cycles seems to leave the hard layer unchanged. Such a process effectively destroys the memory cell functionality. Indeed, it would be required to reset the bit after a piece of time by saturating the HL again, an operation that cannot be easily implemented within a real memory. Depending of applications, a magnetic tunnel junction then requires a reference layer with magnetization stable over 10^5 to 10^{14} reversals of the free layer.

In [GID98], the authors investigated the stability of Co₇₅Pt₁₂Cr₁₃ hard layer and the Al₂O₃ tunneling barrier formed by dc magnetron sputtering. They found that the hard layer can be demagnetized by repeated cycling of the soft layer. However if the hard layer is exchange-bias to an antiferromagnetic layer, that layer is stable for at least 10^7 cycles. Such a performance is equivalent to about one write cycle per second for 1 year (but is insufficient for random access memory (RAM) applications. A marked difference in the stability of magnetization \mathbf{M} of exchange-biased and hard layers is evident in the decay curves of Fig. 5.13. The decay was strongly dependent on the thickness of the hard layer. Increasing the thickness of hard layer from 50 to 100 Å delays the demagnetization by one order of magnitude in the number of cycles.

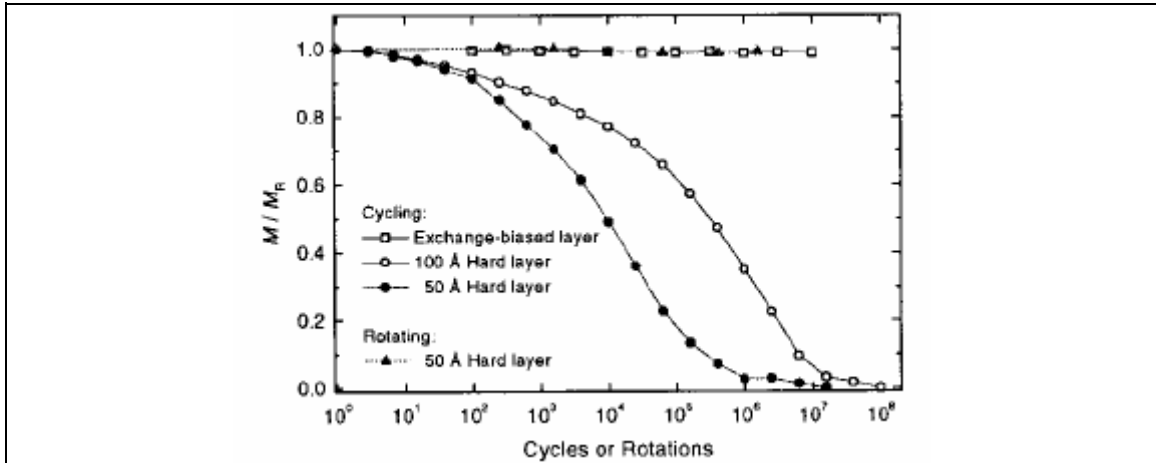


Fig. 5.13: The change in remanent magnetization of the reference layers with numbers of field cycles or rotations of the free layers, plotted on a logarithmic scale. The curves are normalized by the remanent magnetization M_R , set at 5000 Oe before cycling or rotating. [GID98]

In [THO00], they worked on the Magnetic trilayers, comprised of a hard magnetic layer of CoPtCr ($\text{Co}_{75}\text{Pt}_{12}\text{Cr}_{13}$), a nonmagnetic spacer, and a soft layer of Co or FeNi ($\text{Fe}_{60}\text{Ni}_{40}$) were grown by dc magnetron sputtering in 10^{-3} Torr Ar on Si/SiO₂ wafers. The cycling was found to progressively demagnetize the hard magnetic layer, even though the cycling field was chosen weaker than the coercive field of the reference layer, and then was expected to be too small to have any direct effect on the hard layer. The authors then proposed a model taking into account the stray fields from domain walls in the soft layer. Indeed, in the close vicinity of the domain wall, the stray fields were found to reach values as high as a few thousand Oe, far exceeding the hard layer coercive field. It was also found that the demagnetization rate of the hard layer was highly sensitive to the thickness of both FM layers, in excellent agreement with calculations of the domain wall stray field strengths and spatial extent. These results can be explained by a model in which stray fields are generated by Néel-like domain walls sweeping through the free layer during reversal of its moment.

Noticeably, all published papers deal with in plane MTJ (or spin valves). As a result, our study may be the first to investigate in depth the physics associated with hard layer demagnetization in perpendicular MTJs.

5.3.2 Kerr effect experiment for cycling measurements

5.3.2.1 Kerr- effect measurement

We have conducted the demagnetization studies of the FePt/MgO/FePt MTJ on the Kerr experiment built in our lab we described above. For a specific requirement for demagnetization experiment is the ability to repeat the cycling of the soft layer. In our case, each demagnetization experiment takes a long time (for example: cycling 500 times with a field 2.0 kOe requires more than 20 hours). Therefore, the ability of the setup to provide a stable magneto-optical signal over hours is crucial. In order to minimize thermal drift, the room is air conditioned.

The experiments have been performed on the full MTJ sample, with the same structure introduced in the part 3.1.2. The sample, with this structure, is in perpendicular configuration. The experimental procedure is reported here below:

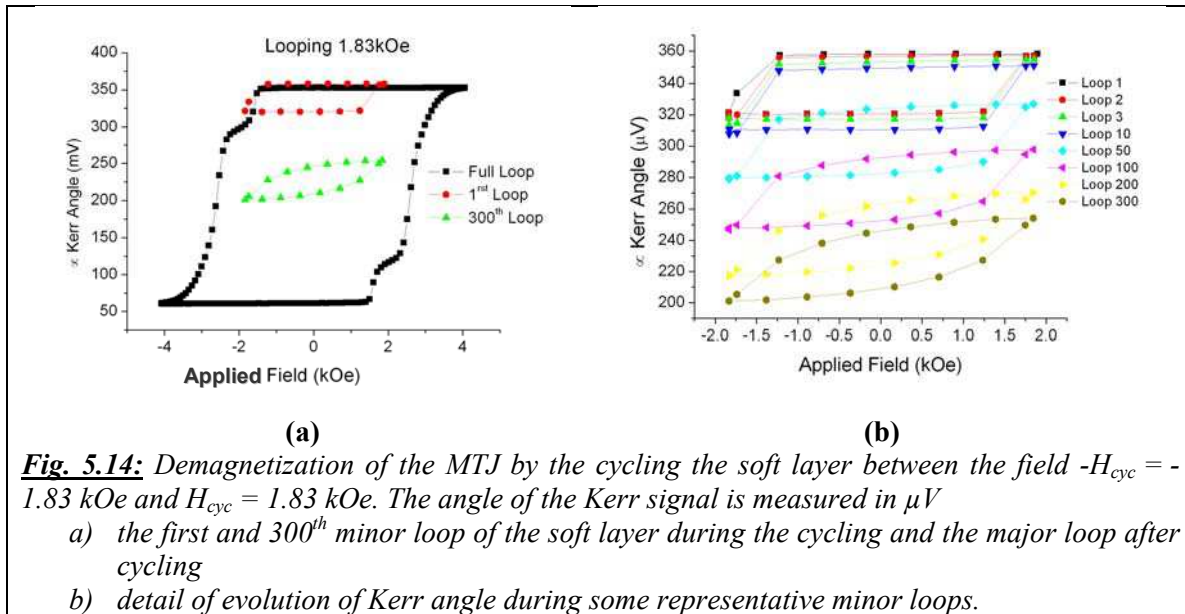
- the sample is first saturated under the field 1 T;
- N minor loops are recorded;
- the full loop is recorded after cycling to determine properly the final state, and the response of the hard layer.

The applied field varies between H_{cyc} and $-H_{cyc}$. To investigate the phenomena of interest, the value of H_{cyc} must be in a range between the saturation field of the soft layer (Oe) and the field at which the hard layer starts reversing ($1.8 \text{ kOe} < \text{signal } H_{cyc} < 3 \text{ kOe}$). It means that the applied field H_{cyc} is large enough to totally reverse the soft layer but should remain too small to have a direct effect on the hard layer according to the quasistatic hysteresis loop.

Each experiment produces a significant amount of data (N cycles). These data are analyzed to determine the value of magnetization amplitude and centre of the minor loop. Please note that the centre of the minor loop can be linked to the magnetization of the hard layer only if the full magnetization of the soft layer is reversed in each cycle. The parameters for this cycling process are the number of cycles and the value of H_{cyc} . Results on these demagnetizing experiments are presented below.

5.3.2.2 Observation of the demagnetization of the structure by cycling the soft layer

We begin the experiment with a cycling field $H_{cyc} = 1.83 \text{ kOe}$. After saturation in a field of 1 T, the sample is cycled 300 times. The Fig. 5.14 shows the evolution of minor loop angle signal and the major loop after cycling.



The progressive demagnetization of the MTJ structure is evidenced in the Fig. 5.14a. The center of the 300th minor loop has shifted toward the centre of the major loop. The full loop (in black color) was recorded after the demagnetization process. We take note that the 1st minor loop is at the expected position within the major loop. It means we have a good thermal stability (that

what not the case before optimizing the experimental set-up and the procedures to avoid thermal drift).

We can see very clearly (Fig. 5.14b) that the shape of the minor loop and its position have changed during the cycling. These effects that we will discuss here below, are clearly linked to changes in the magnetization pattern of the hard layer (demagnetization). Noticeably, if saturating again the full MTJ, we observed again the same initial cycles for the soft layer.

At the beginning of experiment, as is shown on the hysteresis loop, the soft and hard the layers reverse independently, separated by the plateau between two square loops. The shape of the minor and major loop is square, especially for minor loop.

After some cycles, the amplitude of the minor loop is decreasing. The centre of the minor loop (Kerr angle axis) is also shifting towards lower values. It is obvious that the minor loop is less and less square over repeated cycling. It might that the magnetization of the soft layer does not reverse completely between $-H_{cyc}$ and H_{cyc} . However, the Kerr experiment does not record the signal of the soft layer and of the hard layer separately: the shape of the hysteresis loop maybe affected by the combination of changes in both layers. It would be tempting to attribute the change in the loop shape (no longer square) to a now partial reversal of the magnetization of the hard layer. However, the amplitude of the minor loop does not change so significantly. We will discuss later how both observations can be attributed to demagnetization of the hard layer.

Let us focus first on the detail of the minor loop. The first minor loop of the soft layer is perfectly square. Over the first field cycles, the minor loop keeps a square shape until the 50th cycle. After that, the shape is changed to a rounder shape (Fig. 5.14b). After the 200th cycle, the minor loop no longer exhibits a square reversal, even if the applied field for cycling $H_{cyc} = 1.83$ kOe is larger than the quasistatic saturation field of the soft layer.

It is probable that the demagnetized domains, created in the hard layer, block the propagation of the walls during the magnetic reversal of the soft layer, which stays then in magnetic state and but also part of the hard layer magnetization cycling at the same time. This magnetic state of the walls is more and more blocked during the cycling. This point is deduced from the reduced magnetization change between the two zero field points of the up and down branches of the loop. As a conclusion, we can say that cycling the soft layer induces nucleation of reversed domains in the hard layer. These domains – through the stray field they create in the soft layer - pins the propagating domain wall in the soft layer, thereby preventing full reversal at the applied field.. the soft layer partially reverses due to pinning on the stray field of the domains appeared in the hard layer, but also - part of the magnetization of the hard layer reverses over each cycle (most part oscillating, that is part of the demagnetization process), adding a contribution to the amplitude of the loop.

In addition focussing on Fig. 5.14b, the centre of the minor loop is decreasing with the number of cycle. This means that the overall positive magnetization of the sample decreases, as may be expected from the demagnetization of the hard layer. We will comment this point later.

Summary:

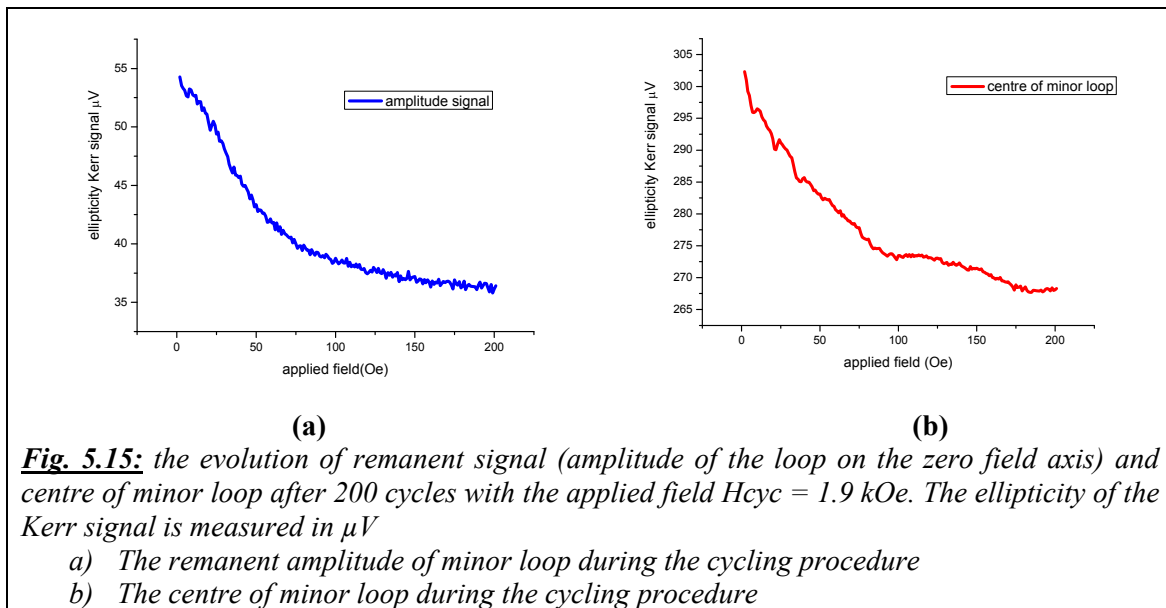
During the soft layer cycling process, under an applied field in the range $1.4 \text{ kOe} < H_{cyc} < 2.2 \text{ kOe}$, we observed the decrease of the centre of the minor loop. After cycling more than 200 times the soft layer, the hard layer is demagnetized. We propose one possible reason deduced from our knowledge of the coupling between the two layers.

5.3.2.3 Behavior of amplitude and centre of the minor loop during cycling process

The amplitude of minor loop (A) is defined by $A = \text{maximum magnetization of minor loop} - \text{minimum one}$. Beside that, the centre of minor loop (C) corresponds to the mean value of the magnetization of minor loop. The centre C is calculated by:

$$C = (\text{maximum magnetization of minor loop} + \text{minimum one})/2$$

Fig. 5.15 shows the evolution of remanent amplitude and centre of the minor loop in experimental condition: $H_{\text{cyc}} = 1.90 \text{ kOe}$ in 200 cycles. The ellipticity signal is shown instead of angle signal.



In Fig. 5.15a and b, the evolution of amplitude as well as centre of minor loop is drawn as a function of the number of cycles. The decrease of the minor loop amplitude can be explained by the appearance of magnetic domains in the hard layer. Indeed, reversed domain in the hard layer (with respect to initial magnetization direction) may progressively develop under the combined action of external applied field H_{cyc} and of the dipolar field H_{dip} due to the magnetic domain in the soft layer. Once these domains have appeared, they are creating up and down stray fields in the soft layer, thereby pinning the soft layer magnetization. As said, over repeated cycling, the decrease of the centre of minor loop in Fig. 5.15b indicates a decrease of the magnetization of the hard layer, consistent with a demagnetization process.

The behavior of demagnetizing procedure is summarized below. We can divide this demagnetizing experiment in three steps:

Step I

For the first 10 loops:

- Square shape of the minor loop
- Centre does not move
- Remanent amplitude of the minor loop constant

Step II

From 10th to 50th loop:

- Nearly Square Shape
- Centre decreases
- Amplitude decreases

Step III

From 50th to 300th loop:

- Square to bundle shape
- Centre and amplitude decrease.

We can draw several conclusions concerning the physical mechanisms involved in these three steps.

Step I:

Nothing happens, apparently... except the local reversal of magnetization in the hard layer through the occasional nucleation of small reversed domains. As these domains cover a small part of the sample surface, these do not affect (in overall measurements) the magnetization reversal of the hard layer.

Step II:

The decrease of the position of the minor loop centre indicates the progressive demagnetization of the hard layer. The fact that the minor loop keeps a rather square shape demonstrates that the demagnetization of the hard layer has a limited effect on the reversal process of the soft layer. The decrease of the remanent amplitude is nevertheless an indication of some influence.

Step III:

The decrease in the centre position keeps going. The hard layer is further demagnetizing (it may continue till zero mean magnetization). One possible mechanism is the one proposed by Thomas *et al* [THO00]. Propagating domain wall inside the soft layer creates a strong stray field inside the hard layer. Added to the applied field it favors the nucleation of reversed domains in the hard layer. These domains then grow under the same combination of fields. In addition, the minor loop shape evolves toward a bundle: the stray field from reversed domains in the hard layer prevents the free propagation of domain walls in the soft layer. Finally, the sample may end up with a partially frozen configuration where only part of the soft layer magnetization can change over minor loops... while part of the hard layer magnetization is submitted to fields high enough to induce partial magnetization reversal (through local domain wall propagation). It remains an open question to know what are the proportions of these two components (hard layer and soft layer magnetization changes) is the observed minor loops.

During the cycling process, after some first cycles, the remanent amplitude of the minor loop is decreasing. Magnetic domains are created in the hard layer and evolve depending on the applied field H_{cyc} . The hard layer thus begins to lose its magnetization. Concerning the soft layer, the minor loop keeps a square shape. It is an indication that the evolution of the magnetization of

the hard layer has no macroscopic consequence on the soft layer: the magnetization cycle is still square.

Then the soft layer begins also to lose its magnetization: it evolves in the stray field created by the magnetic domains of the hard layer and it links with the soft layer. However, after 50 cycles, the minor loop still keeps a square shape.

At last, after $N = 200$ cycles, the Fig. 5.15b shows a quick drop of the coercive field of the minor cycle. For $N < 200$ cycles, a magnetic jump is still present, indicating that the two electrodes are not fully linked: the soft can flip a good part of itself even with the stabilizing effect of the leakage field of the hard. After this limit, the minor cycle look like bundle. The magnetic coupling between the two layers is then too important to observe a jump in the minor cycles.

Summary:

Cycling the soft layer (with field below $H_c(HL)$) results in:

- *progressive demagnetization of the hard layer, due to the combination of externally applied field and of stray field from domain wall in the soft layer.*
- *progressive pinning by stray field from hard layer domain walls preventing full reversal of soft layer over minor loops.*

5.3.2.4 Demagnetizing procedure under different value of applied field for cycling H_{cyc}

As discussed before, interesting values for the applied field in the cycling procedure must be larger than the saturation field of the soft layer and lesser than the field at which the hard layer start reversing (reversal field): 1.4 kOe – 2.2 kOe. In order to study the influence of the applied cycling field H_{cyc} , we performed experiments with different value of H_{cyc} : 1.6 kOe, 1.7 kOe, 1.8 kOe and 2.0 kOe. The result is shown in Fig. 5.16.

The overall tendencies observed during the demagnetization experiment does not change with changing H_{cyc} , except that the amplitude of the minor loop may reach higher values at higher cycling fields (compare Fig. 5.16c to a).

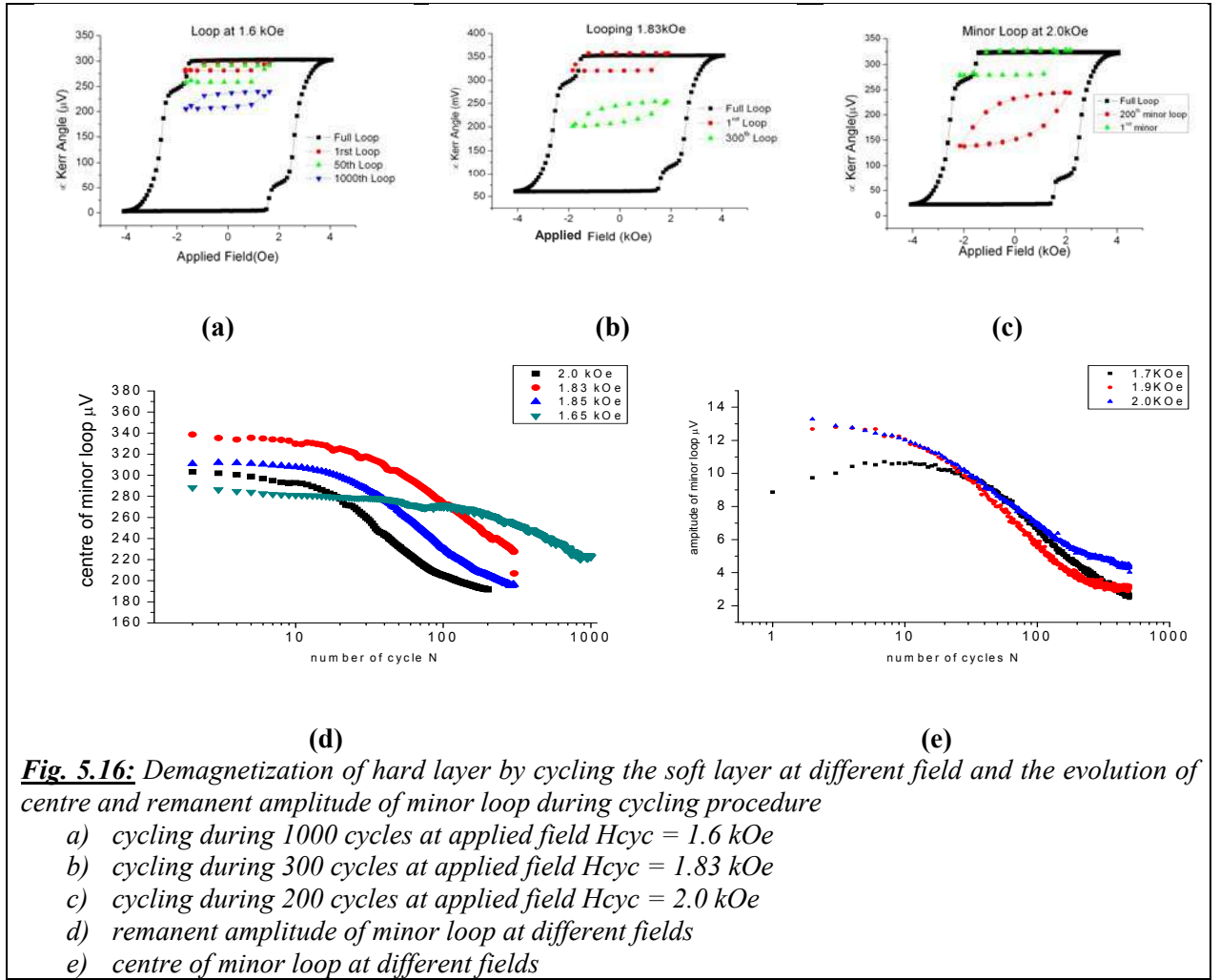


Fig. 5.16d and e present the variation of the remanent amplitude and the centre of the minor loop as a function of the number of cycles. Those figures show a decrease of the remanent amplitude and the centre of minor loop with the number of cycles. The decrease is more rapid when the applied field H_{cyc} is increased. Our first conclusions are:

The dependence of both the centre and the remanent amplitude of the minor loop upon the number of cycles look like exponent decreasing. The decreasing looks monotonous for all the cases. We will discuss further these observations later.

The applied field $H_{\text{cyc}} = 1.6 \text{ kOe}$ value is the lower value of applied field in our measurements. We think that the stray field from domain walls in the soft layer hardly nucleate / propagate domains in the hard layer. So the demagnetization process is significantly slower.

Interestingly, the decreasing of the hard layer magnetization (corresponding to the centre of the minor loops on the Kerr signal axis) starts earlier when the applied field is increased. It means that the larger the applied field H_{cyc} is, the larger the part of the hard layer magnetization reversed in each cycle for minor loop is, and finally, as a result: the quicker the demagnetization is.

This is evidenced on Fig. 5.17, which assembles normalized data. This can obviously be associated with a faster demagnetization process. The obvious part is that the combination of the

stray field from the domain wall in the soft layer, and of an increased external cycling field, is stronger. An additional but less obvious effect may be that – due to higher applied field - magnetization pinning in the soft layer must be reduced. As a result, more domain wall propagation may be observed in the soft layer, thereby submitting a larger part of the hard layer to significant demagnetizing fields.

As said, the decrease of the minor loop centre “is” a measure of the demagnetization of the hard layer (Fig. 5.17). With this normalization, the centre of minor loop during the cycling is calculated by:

$$C_{nor}(N) = \frac{C(N) - C(FL)}{C(N=1) - C(FL)} \quad (5.4)$$

Where: $C_{nor}(N)$ is the centre of N^{th} minor loop after normalization

$C(N)$ is the centre of N^{th} minor loop

$C(FL)$ is centre of the major loop

$C(N=1)$ is the centre of minor loop form the beginning of cycling procedure

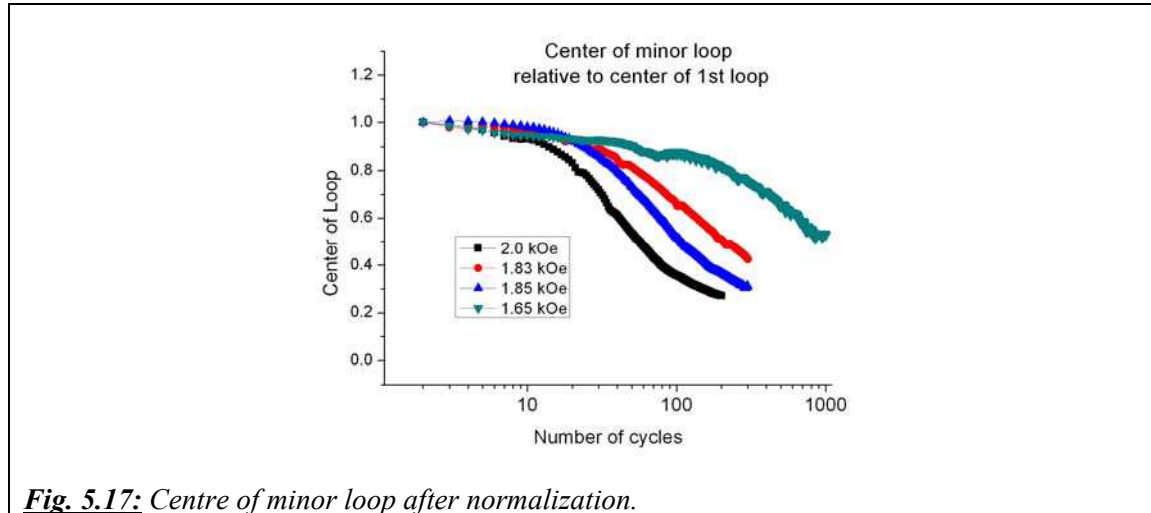


Fig. 5.17: Centre of minor loop after normalization.

After normalizing the data, it is easier to compare data of all the cases of different applied field. Let us find the number of loops needed to have $C = 0.5$, which mean that the hard layer is half demagnetized, and compare that value for each applied field:

- $C_{nor} = 0.5$ after 30 cycles for 2.0 kOe
- $C_{nor} = 0.5$ after 90 cycles for 1.85 kOe
- $C_{nor} = 0.5$ after 1000 cycles for 1.6 kOe

This confirms again the dependency of demagnetization to applied field H_{cyc} . With the lower applied field, we need more cycles for the centre of the loop to be shifted; therefore the demagnetization occurs more slowly.

Summary:

- *The dependency of the centre and remanent amplitude of minor loop to number of the cycles looks like exponent decreasing.*
- *The larger the applied field, the quicker the demagnetization is.*

5.3.3 MFM experiment

5.3.3.1 MFM experiment at various points of the cycling experiment

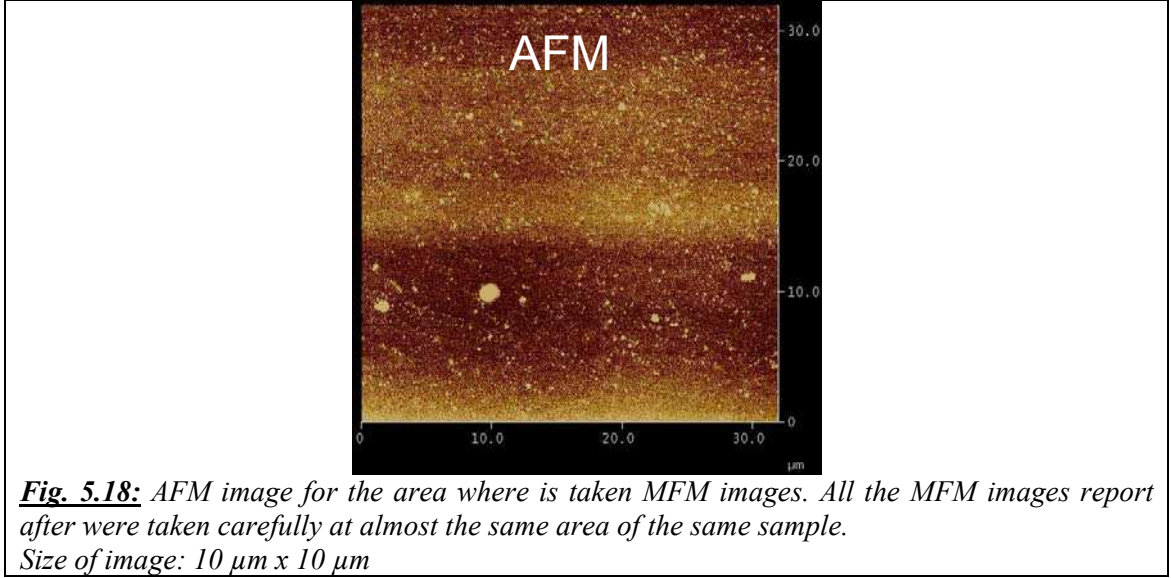


Fig. 5.18 presents MFM images recorded at various steps of the cycling procedure. The experimental procedure is the same than for the experiments described in the previous part. The applied field here varies from $-H_{\text{deg}} = -2$ kOe to $H_{\text{deg}} = 2$ kOe. We stopped the cycling at a field $H = 0$ Oe. The MFM images were taken after several cycles, always at almost the same area on the surface (as for AFM image in Fig. 5.17). The location of this area is followed by the camera.

Just let us start with a few words on MFM. Indeed, the issue of contrast in magnetic force microscopy is a complex one, mainly as the tip probe field (or field gradient...) and not directly magnetization. For all experiments, we classically used MFM tips magnetized along the tip direction (hence close to the perpendicular to the plane of the imaged layer). Whatever the tip configuration (and neglecting changes in the sample magnetization due to tip influence), a uniformly magnetized layer does not produce any contrast. It is also important for the forthcoming images in the fact that the contrast between up and down domains is the larger close to the domain walls. Indeed, the field (and field gradient) is the highest close to a domain wall, the domain wall separating areas where the MFM tip experiences up and a down magnetic field. The contrast between up and down domains, far from the domain wall, can be very weak. For the same reason, the contrast is higher between small domains, implying one should not interpret too rapidly differences in contrast amplitude as linked to differences in the magnetization states.

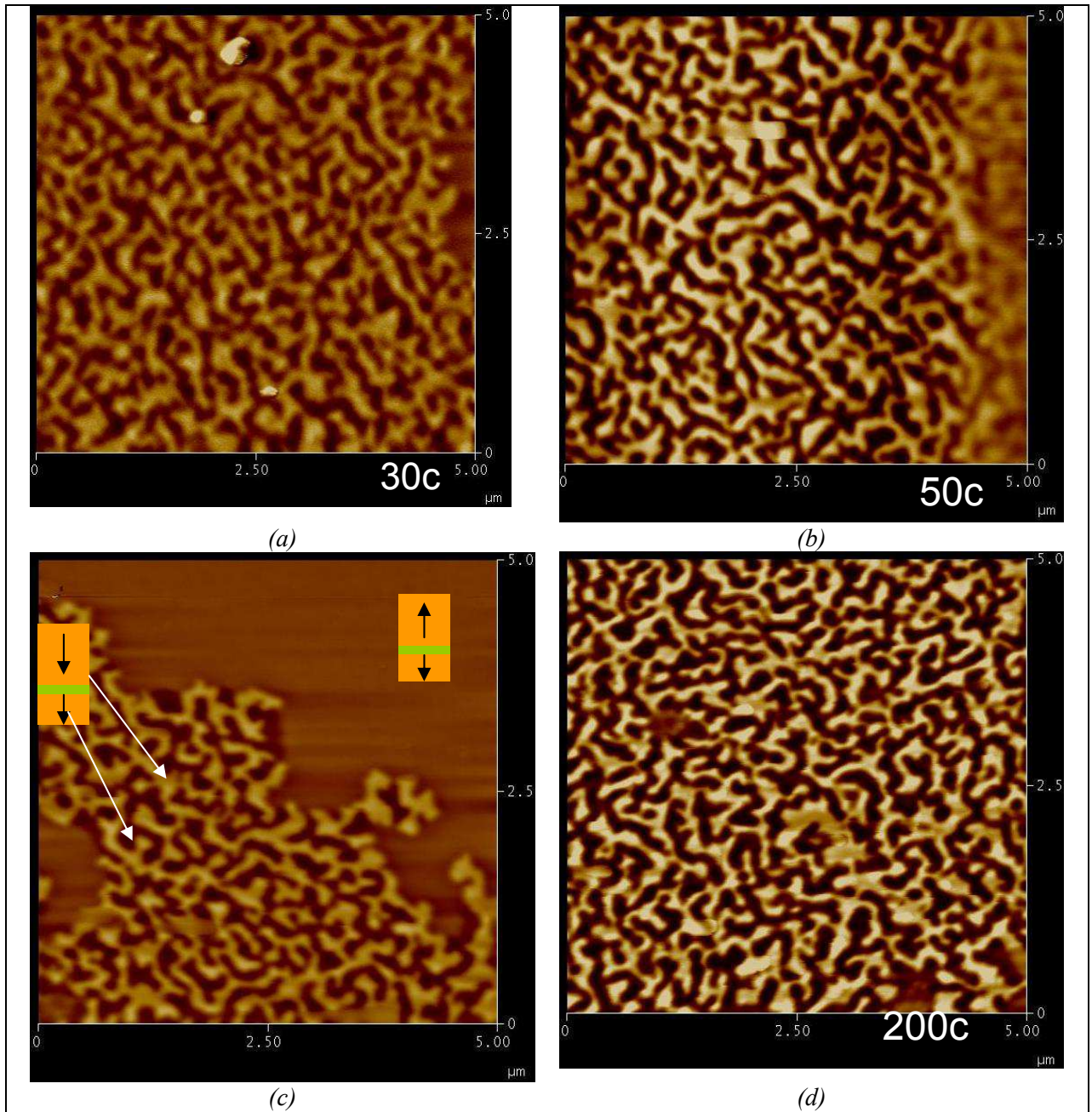


Fig. 5.19: MFM images of magnetic configuration during cycling procedure with applied field $H_{deg} = 2.0$ kOe.

- a) after 30 cycles (image recorded at 0 field)
- b) after 50 cycles (image recorded at 0 field). Note that the reduced contrast in the right part of the image is due to a drift in imaging conditions and does not correspond to differences in the sample.
- c) after 100 cycles (image recorded at 0 field)
- d) after 200 cycles (image recorded at 0 field)

Image size: $5 \mu\text{m} \times 5 \mu\text{m}$

Fig. 5.19 shows MFM images recorded after the procedure described above. They were taken after 30, 50, 100 and 200 loops respectively. First of all, when the applied field reach $H_{\text{cyc}} = 2.0$ kOe, all the soft layer is expected to be reversed to \downarrow state.

Whatever the number of cycles, where reversed domains can be found, they always exhibit the same morphology: a classical maze pattern. The remarkable fact is that this pattern does not cover the entire surface (see Fig. 5.19c), but attests an original demagnetization process. Let us comment:

- even if the width of the ribbons exhibits significant variations, a mean width can be easily highlighted, close to 150 nm. This width, close to the equilibrium size of the ribbons, is controlled by the equilibrium between demagnetizing field and domain wall energy.
- in most cases, magnetization reversal occurs in disordered layers through dendritic, or even fractal growth of the reversed domain (see recent publications from our laboratory on FePt thin films [ATT04]). This is not the case here, as reversed domains in the hard layer (down) propagate through compact areas, where up and down ribbons are both of similar width: the mean magnetization is close to zero over these areas, while other (large) areas remain unaffected.
- what evolves upon further cycling is the part of the surface of the hard layer covered by the up and down ribbons, this part obviously increasing as the demagnetization proceeds.

To sum it up, the demagnetization process occurs through the growth of μm -sized (and larger) areas that are locally demagnetized, and where the magnetic pattern is close to equilibrium.

Our suggestion is that this peculiar reversal mode is intimately linked to the oscillating field we apply: the reversed domains are bound to grow and next partially shrinks as the field oscillates. As a result, the domain wall can “try” many paths, thereby diminishing the weight of sample disorder on the domain shape, and removing the less stable configurations. This ends up with the compact pattern of up and down ribbons we observe.

Noticeably, on all the images we observed till now, we did not see any feature we can relate to domain walls in the soft layer. In Fig. 5.19, after applying 2 kOe, it is clear that the soft layer is indeed saturated, at least far from the reversed areas in the hard layer.

Conversely, in the areas covered by the reversed ribbons in the hard layer, it is not possible to fully ascertain the magnetic configuration of the soft layer:

- large domains (with respect to the ribbons observed in the hard layer) with either up or down magnetization will not create a large enough stray field at the tip position to be differentiated from the strong contrast associated the HL ribbons.
- domain mirroring is a possibility below the hard layer ribbons, but will not introduce any distinguishable signal.

5.3.3.2 MFM experiments to observe domains of both soft and hard layer at lower applied field $H_{\text{cyc}} = 1.8$ kOe

Till now, we evidenced only the magnetic domain in the hard layer. However, building upon experimental clues from the Kerr measurements, we proposed a model in which the combination of the external field with the stray field from domain walls in the soft layer accounts for the hard layer demagnetization. It is then worth trying observing these domain walls in the soft layer. We then need to apply smaller fields, such that the soft layer may not be fully saturated before MFM imaging.

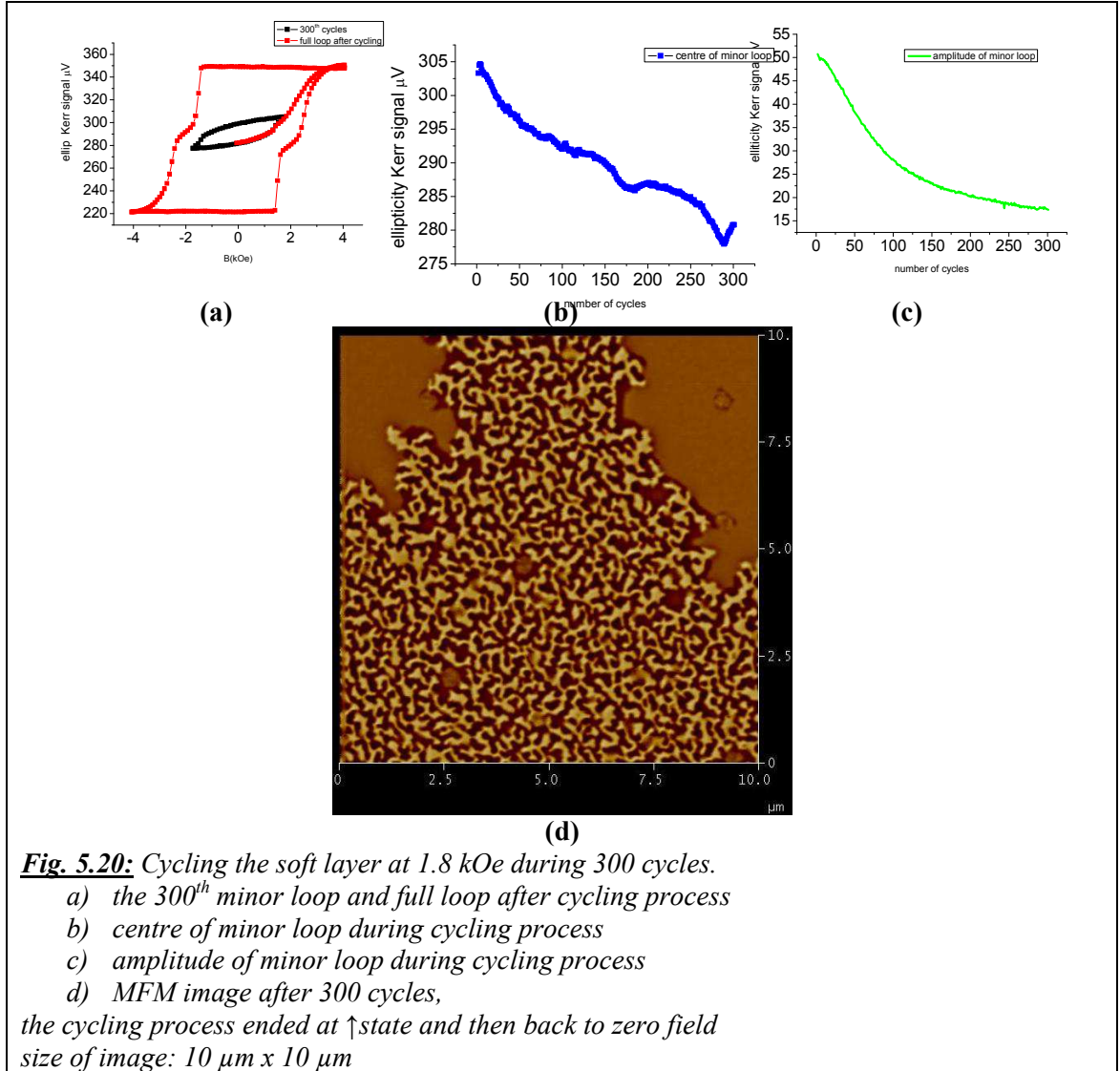
We started along this direction by cycling the sample at $H_{\text{cyc}} = 1.8$ kOe (instead of 2 kOe). Then, we hoped to be able to observe some parts of the domain wall propagating in the soft layer.

In Fig. 5.19, the sample is partially demagnetized, as evidenced by parts a), b) and c). We can see in part d) that demagnetized areas with the up and down ribbons in the hard layers cover a (large) part of the sample surface. Most interestingly, we observe remanent parts of the down domain (darker) in the soft layer as the cycling has been stopped after the positive field excursion. These remanent parts surround the demagnetized area of the hard layer, as the down magnetic configuration is here stabilized to the field from the up domains in the hard layer.

The fact that the dark areas we here observe are not simply due to the stray field from the hard layer up (white) domains is clear as these dark areas are not observed in the vicinity of all white domains. In addition, these dark areas exhibit large radius of curvature that are more typical of the thinner (hence the domain equilibrium size is larger) and less disordered (hence the domain wall shape is less governed by structural defects) soft magnetic layer.

This domain wall propagating in the soft layer is responsible from the demagnetization process in the hard layer, and we can now propose two further comments:

- looking closer to images obtained with the 2 kOe cycling field, similar dark areas were also observed (though less extended), indicating that the down domain was still present below the demagnetized areas;
- the fact that the domain wall in the soft layer retracts to and grows again from the demagnetized areas should participate to the compact shape of the demagnetized areas.



These comments are further supported by the large images from Fig. 5.20. Here we clearly see how the unfavored domain in the soft layer is collapsing, leaving some small domains with irregular shapes from place to place (dark areas), but is also retracting around the demagnetized areas where it is stabilized. In addition, some sample defects (may be scratches) may explain the straight features observed in the left and middle right part of the image. We also see clearly how the demagnetized area is growing while keeping a compact shape, a remarkable observation.

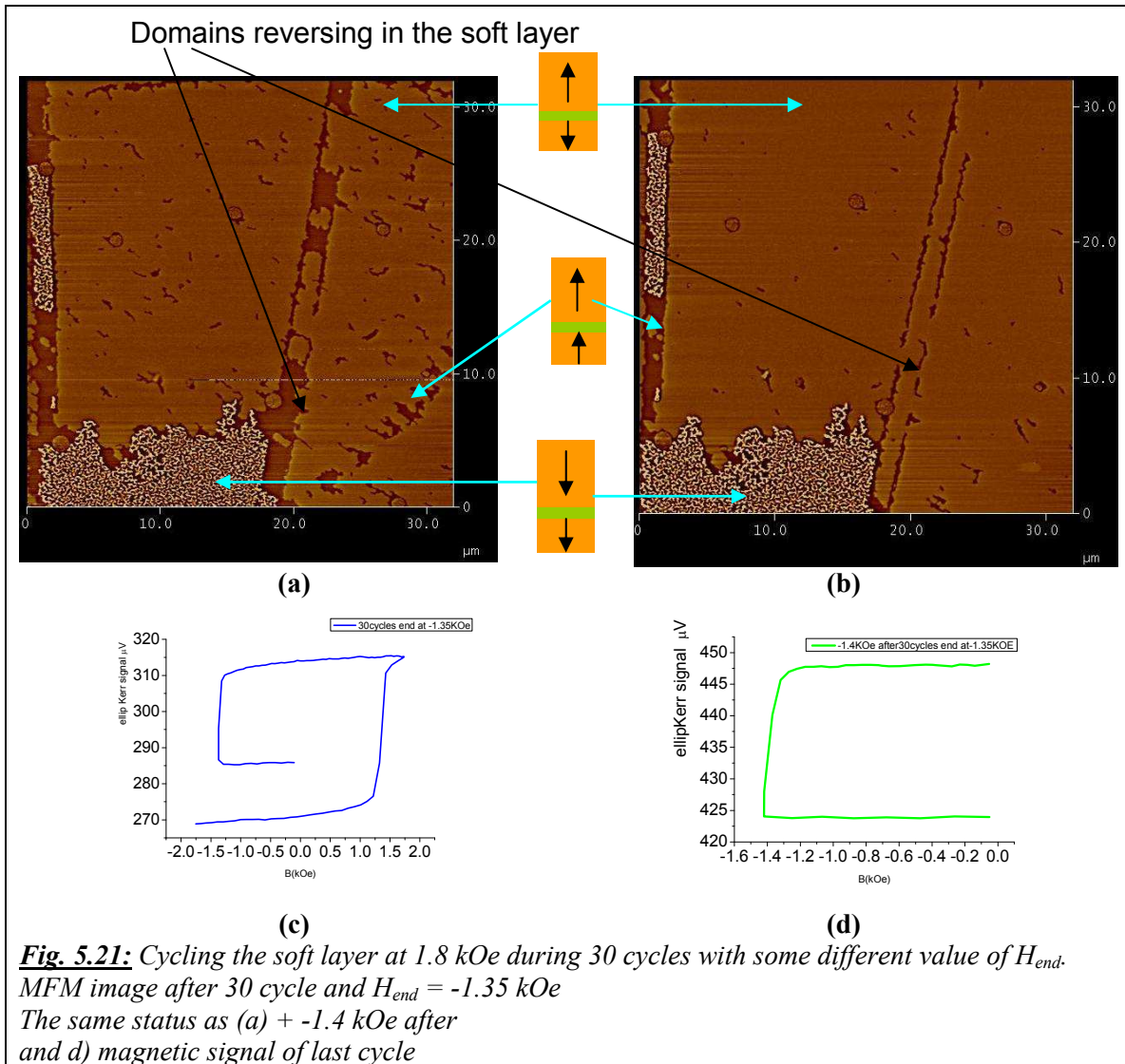


Fig. 5.21: Cycling the soft layer at 1.8 kOe during 30 cycles with some different value of H_{end} . MFM image after 30 cycle and $H_{end} = -1.35$ kOe
The same status as (a) + -1.4 kOe after
and d) magnetic signal of last cycle

On Fig. 5.21a and b, magnetic domains in the hard layer and in the soft one are visible. The most interesting in those images is that we can follow the reversing process of the soft layer. Indeed, when we increase H_{end} by a 0.05 kOe (from -1.35 kOe to -1.4 kOe), unreversed magnetic domains of the soft layer are less numerous. It means also that the soft layer is still reversing while the domains of the hard layer do not evolve. Domains in the soft layer, in dark brown color, propagate freely. They do not follow any crystal direction. In addition, domains in the hard layer have original shapes: we have the impression that they grow compactly from some nucleation centers.

We also observe that domains of the hard field seem to be constrained inside unreversed domains of the soft layer, thanks to the stray field.

Summary:

Cycling 30 cycles at 1.8 kOe and ending at -1.3 kOe and -1.4 kOe, we have:

- *In the soft layer: domain wall propagates freely (without any directional anisotropy).*
- *In the hard layer: reversed domain exhibits a peculiar compact shape clearly associated with the specific reversal process of the soft layer.*

5.3.4 Mathematical analysis of the behavior of the centre and remanent amplitude during cycling

We reported the phenomena indicating a decrease of the magnetization in the hard layer by cycling the soft one. This is also reported in [GID98] and [THO00] with planar magnetization. In [GID98], they found that magnetization of the hard layers had a slow logarithmic decay toward demagnetization. The initial form of the decay can be well described by $M/M_R \approx 1 - [\log(N/N_0)]^2$, where M_R is the initial remanent M of the reference layer, N is the number of cycles, and N_0 is an adjustable parameter. The decay is independent of the frequency of the cycling. Beside that, in the thesis of De Person [PER07], for the same MTJ structure with perpendicular magnetization like us, he also found that the evolution of the normalized remanent amplitude of the magnetic cycles can be fitted with a function in the form of $\exp^{-(N/N_0)^\beta}$ where N is the number of the cycle and N_0 and β are constant ($N_0 \sim 260$ and $\beta \sim 0.9$). However, as he discussed in his thesis, it is difficult to conclude anything from this fit except the speed of the demagnetization process. Indeed, the magnetization of the two electrodes is studied by Kerr effect: the beginning of the process corresponds to a state where only the hard electrode loses its magnetization, the end of the process is itself a complex state, difficult to describe without further data (like magnetic images), where the two electrodes are coupled. Moreover, in both studies [GID98, THO00], they do not determine any influence of applied field H_{cyc} for cycling to the demagnetization evolution. Therefore, we devoted ourselves to determining the evolution of the demagnetization process as a function of related parameters: applied field for cycling H_{cyc} and number of cycles N .

5.3.4.1 Formula for centre of minor loop

Fig. 5.22b shows that the generic behavior of all the curves for the centre of the loop is a monotonous decrease, with a fast start and slowly going to a saturation state. For these reasons we fit all these curves with an exponential decay formulation:

$$C = C_{\text{inf}} + \Delta C \times \exp^{\frac{-N}{N_0}} \quad (5.5)$$

here $\{C_{\text{inf}}, \Delta C, N_0\}$ are the fitting parameters. They correspond to:

- C_{inf} : the position of the centre after an infinite number of cycles. This value seems to depend on the configuration of the measurement tools.
- ΔC : the variation of the position of the centre between the initial state and the one after an infinite number of cycles. It gives the remanent amplitude of the demagnetization of the sample.
- N_0 , the number of cycles to obtain a variation of 36% (when $\exp^{\frac{-N}{N_0}}(N=N_0) = \exp^{-1} = 0.36$) of the position of the centre.

The fit is done following a mean square minimization, *i.e.* we try to minimize the set of parameters $\{C_{\text{inf}}, \Delta C, N_0\}$. The minimization uses an iterative algorithm called “Marquardt-Levenberg algorithm”, as implemented in the Gnuplot software we used for the numerical analysis. The detailed description of the algorithm and its implementation can be found in “Numerical Recipes in C, Chapter 15.5: Nonlinear models”¹.

¹ <http://www.fizyka.umk.pl/nrbook/c15-5.pdf>

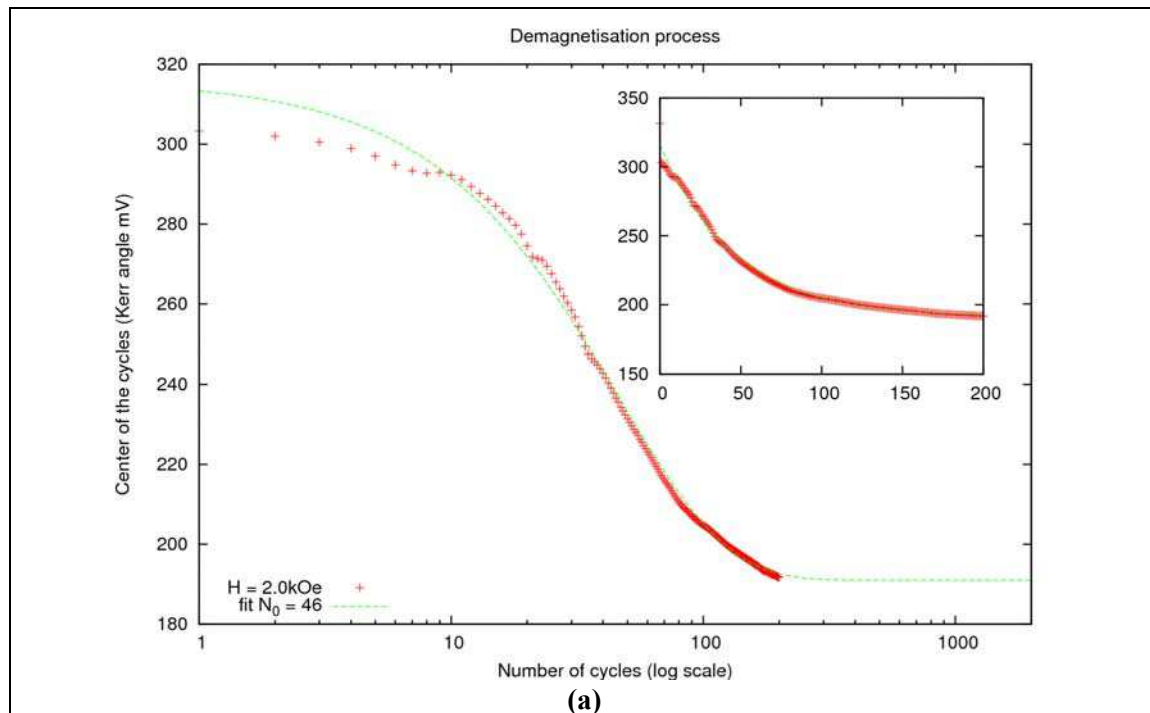
The values are reported in Table 5.3:

	C_{inf}	ΔC	N_0	RMS^2
H = 2.0 kOe	191 mV	125 mV	46	2.3 mV
H = 1.85 kOe	218 mV	124 mV	129	1.6 mV
H = 1.83 kOe	192 mV	131 mV	84	1.6 mV
H = 1.65 kOe	199 mV	82 mV	721	1.5 mV

Table 5.3: centre fitting value of C_{inf} , ΔC and N_0

The RMS is here the “root mean square” of residuals: $\sqrt{SSR / NDF}$, with SSR being the sum of square residuals and NDF the number of degrees of freedom (*i.e.* the number data in the fit). This value is to be compared to the overall variation of the data, roughly represented by ΔC . The lower it is, the better the fit is.

The fit is of a good quality, as the RMS values testify, even for the worst case H = 2.0 kOe as shown on the Fig. 5.22a. All data and their respective fits are represented on Fig. 5.22b.



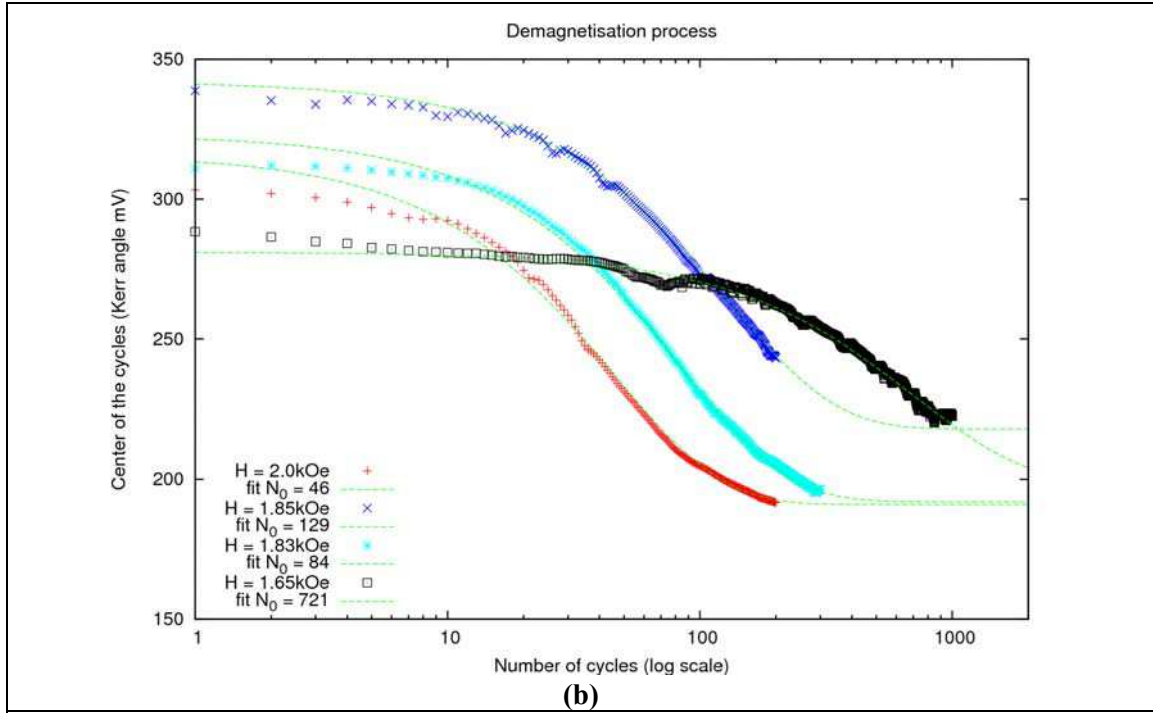


Fig. 5.22: variations of the position of the centre in Kerr measurements during cycling. The fitting curve is an exponential decay.

Data are represented both in logarithmic scale and linear scale for the number of cycles for $H = 2.0$ kOe.

Data are plotted for all values of applied field and respective fit are given.

These fits highlight two points:

- there are two regimes for the parameter ΔC , representing the demagnetization of the sample. Above 1.8 kOe, the variation in the position of the centre does not depend on the applied field and is roundly equal to 127 ± 4 mV. On the contrary, below this value, we observe a lower demagnetization of only 82 mV for $H = 1.65$ kOe. This seems to indicate a critical H_c value of the applied field around 1.7 kOe above which the demagnetization is significantly more effective.
- the characteristic number of cycles N_0 is a function of the applied field and decreases with it.

Before discussing the behavior of $N_0(H)$, we can try to see what happens if we remove the H_c hypothesis described in the first point. Indeed, we can consider that the set of data for $H = 1.65$ kOe is not complete enough to reach the full demagnetization and this prevents a correct fitting. It means that the demagnetization is not complete and need numerous of cycle more for the hard layer to be demagnetized. We decided to impose $\Delta C = 127$ mV also for the set of data at 1.65 kOe:

	C_{inf}	ΔC	N_0	RMS
$H = 1.65$ kOe	199 mV	82 mV	721	1.5 mV
$H = 1.65$ kOe	151 mV	127 mV	1513	2.2 mV

Table 5.4: fitting for the set of data at 1.65 kOe.

The plot of the new fit is shown on Fig. 5.22.

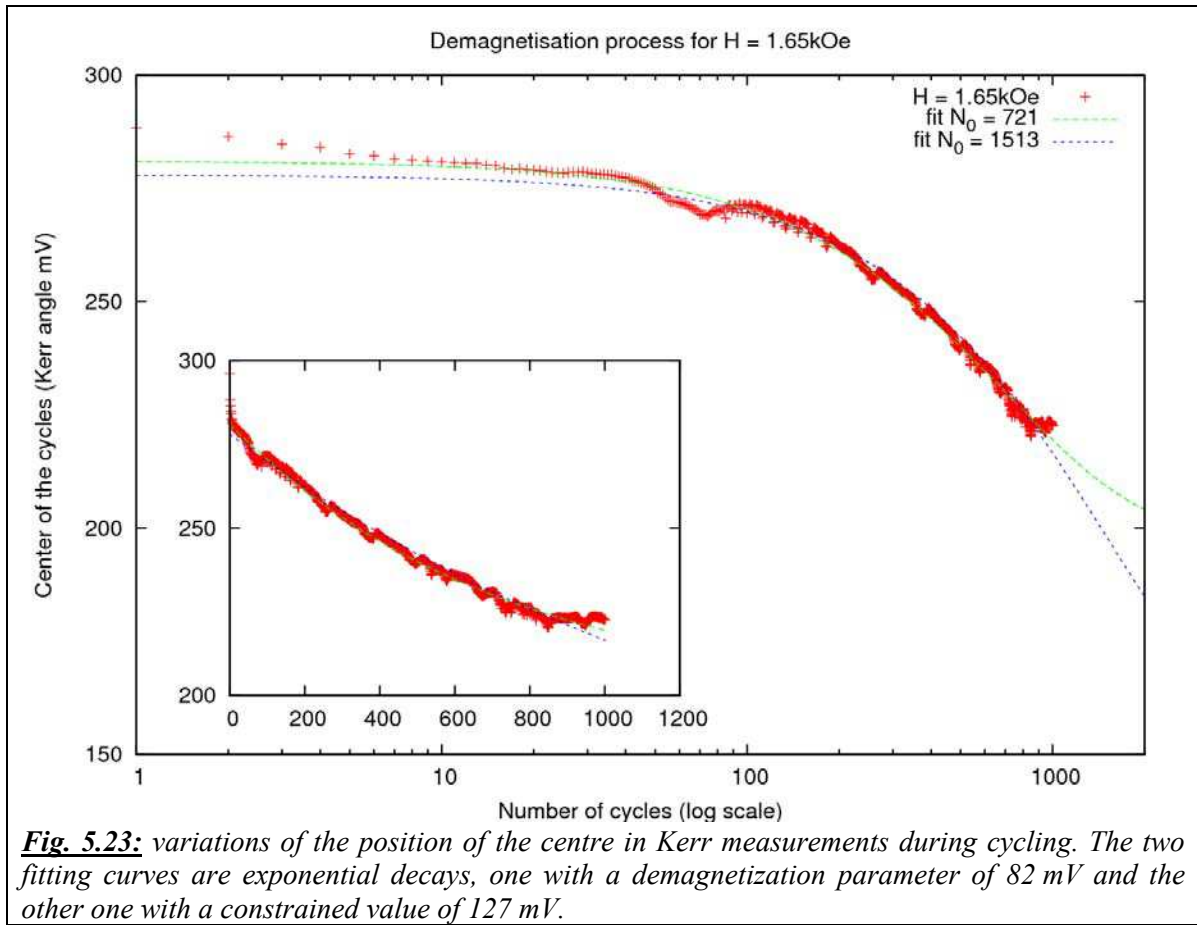


Fig. 5.23: variations of the position of the centre in Kerr measurements during cycling. The two fitting curves are exponential decays, one with a demagnetization parameter of 82 mV and the other one with a constrained value of 127 mV.

The new fit is quite correct also regarding the RMS value but the curvature is not fully representing the shape of the set of data.

The plot of $N_0(H)$ is represented on Fig. 5.24.

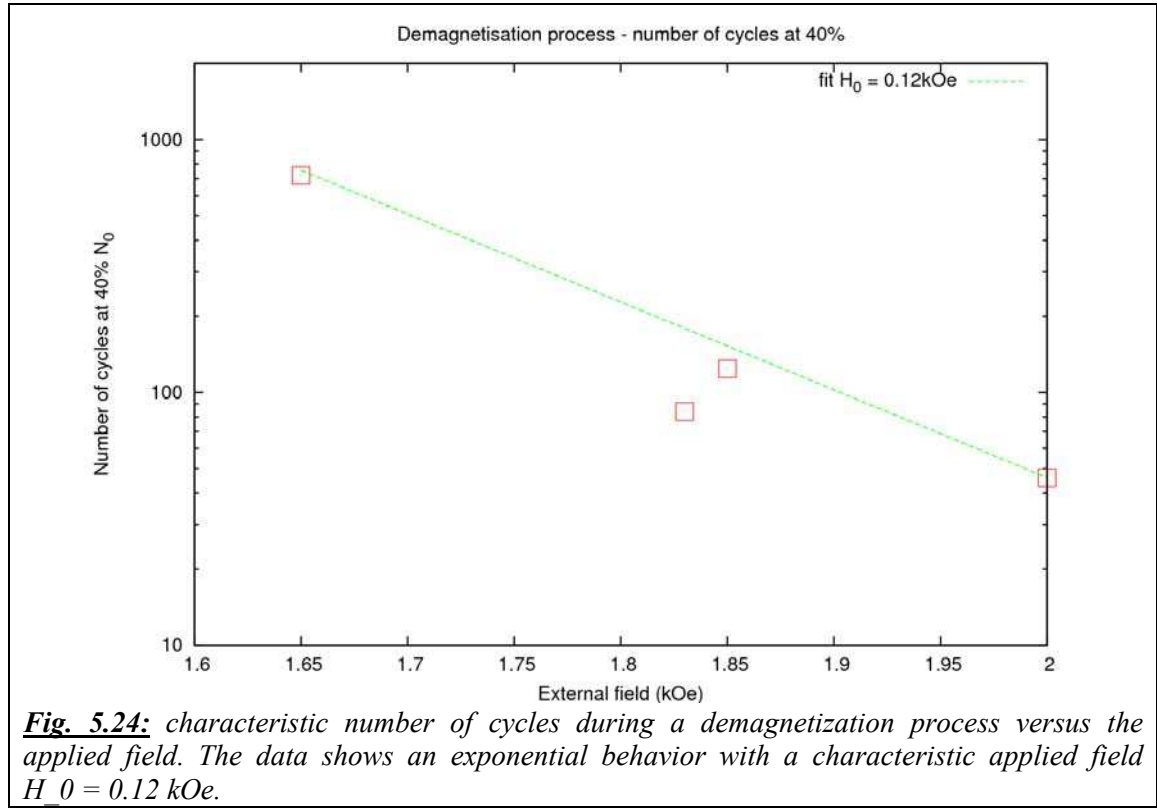


Fig. 5.24: characteristic number of cycles during a demagnetization process versus the applied field. The data shows an exponential behavior with a characteristic applied field $H_0 = 0.12$ kOe.

The behavior of $N_0(H)$ seems to be an exponential decrease with H . The fitting curve on Fig. 5.23 is:

$$N_0(H) = N_0(H = 2.0\text{kOe}) \times \exp \frac{H-2}{H_0} \quad (5.6)$$

with $H_0 = 0.125$ kOe, using the characteristic number of cycles N_0 at applied $H = 2.0$ kOe as a reference. One can thus use H_0 to extrapolate this characteristic number to other values of applied field. It characterizes the response of the sample to an applied field H . The higher H_0 is, the quicker the demagnetization process.

Summary:

Decay of centre of minor loop C can be expressed by the formula:

$$C = C_{\text{inf}} + \Delta C \times \exp \frac{N}{N_0}$$

$$\text{With: } N_0(H) = N_0(H = 2.0\text{kOe}) \times \exp \frac{H-2}{H_0}$$

The decay depends directly on the number of cycles and applied field for cycling. The formula is also related to experimental set up. The formula fits well with experimental data.

5.3.4.2 Formula for remanent amplitude of minor loop

After this analysis of the position of the centre, we can try to apply the same exponential decay behavior to the remanent amplitude sets of data. To obtain a proper exponential fit, we need in that case to remove the 20 first values because of unstable experimental condition at the beginning of the experiment. The fitting parameters are summarized in Table 5.5:

	C_{inf}	ΔC	N_0	RMS
$H = 1.7 \text{ kOe}$	2.5 mV	7.6 mV	137	0.4 mV
$H = 1.9 \text{ kOe}$	3.0 mV	7.1 mV	81	0.4 mV
$H = 2.0 \text{ kOe}$	4.4 mV	5.7 mV	101	0.4 mV

Table 5.5: parameter for remanent amplitude fitting.

In the case of remanent amplitude, no variation in ΔC is observed. For the case of N_0 , the behavior is not clear but looking at the curves as shown on Fig. 5.25, we can see that the curves decay almost at the same time. So we conclude that N_0 for the remanent amplitude is not significantly impacted by the applied field.

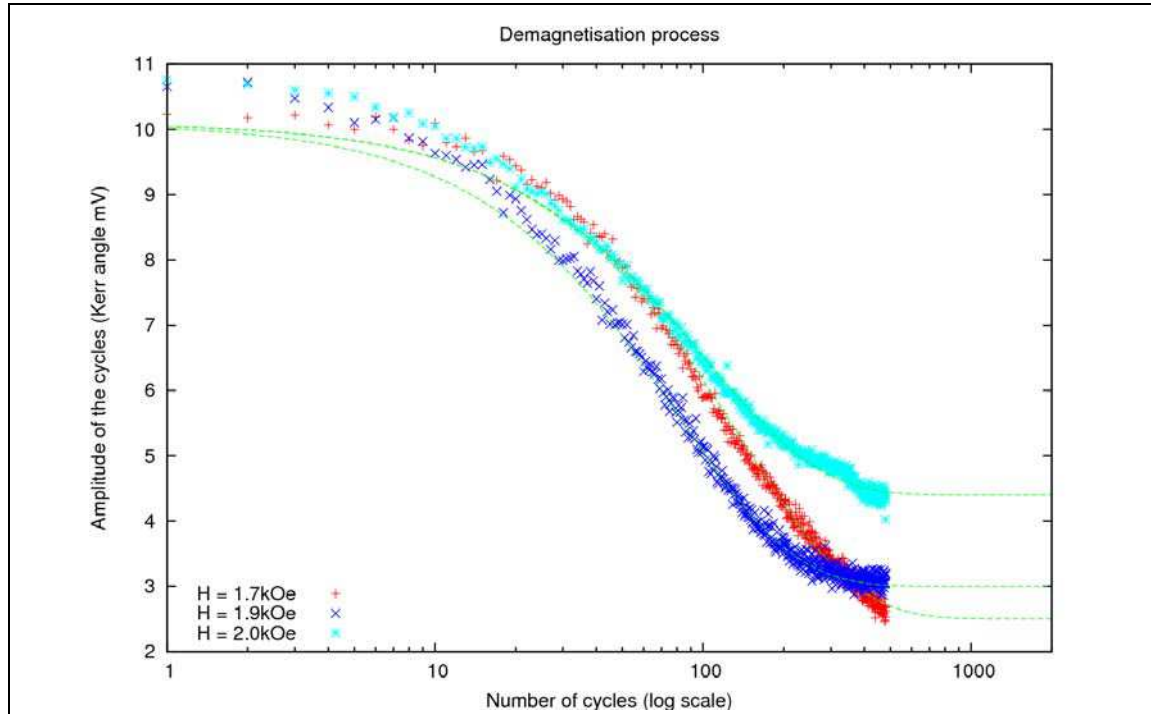


Fig. 5.25: variations of the remanent amplitude of the cycle in Kerr measurements during cycling. The fitting curves are exponential decays.

5.3.5 Conclusion

In MTJ structure, it is possible to demagnetize the hard layer by cycling the soft layer. We have presented evidences from remanent amplitude and centre of minor loop decreasing to confirm that. When coercive field of the hard layer is not large enough, hard layer magnetization is sensitive to repeated cycling of the soft layer, leading to:

- progressive hard layer demagnetization. MFM gives evidence of that effect.
- progressive vanishing of soft layer sharp reversal as more and more pinning is introduced by hard layer domain wall stray fields
- the higher the applied field for cycling, the quicker the cycling process is.

This demagnetization occurs very rapidly. We believe that the stray field above the soft layer domain wall is the driving force behind this effect. We have also observed by MFM specific domain shape in the hard layers. They grow very compactly during the cycling process.

CONCLUSION AND PERSPECTIVES

Both the study of magnetization reversal in thin films with perpendicular magnetic anisotropy (PMA) and of magnetic coupling within perpendicular magnetic tunnel junctions (MTJs) revealed rewarding, as uncovering a rich and complex physics.

Let us remind two of the initial questions, when we started this work:

- till now, dynamic studies of domain wall propagation phenomena in thin films with PMA have been focused on systems with interface anisotropies, such as Pt/Co/Pt. It is possible to extend such studies to FePt thin films, where PMA is related to bulk magnetocrystalline anisotropy, and then extend the studies towards “thick” layers?
- the feasibility of ultra high anisotropy – high magnetization (FePt based) MTJs has been demonstrated by P. De Person (2006), who observed independent magnetization reversal of the two FePt layers in quasi-static single hysteresis loops... but observe progressive demagnetization of the hard layer over repeated cycling of the soft one. Was it possible to gain further understanding of the involved mechanisms, to finally draw a consistent picture of the involved processes?

Practically, we investigated perpendicular MgO based MTJ as well as single FePt layer. All films were grown by MBE. Both in situ and ex-situ techniques were used to ascertain the sample qualities with respect to our objectives: hysteresis loops show square reversals and full magnetic decoupling in quasi-static loops.

FePt/MgO/FePt trilayers were obtained with high perpendicular anisotropy associated with strong and uniaxial chemical ordering of the FePt alloy in the $L1_0$ phase (with perpendicular c-axis). The bulk anisotropy value of the chemically ordered FePt alloy is close to $K_u \approx 5 \cdot 10^6 \text{ J.m}^{-3}$. Interestingly, the huge magnetocrystalline anisotropy means that most of structural defects are also strong anisotropy defects and introduce a large sample disorder, that influences domain wall propagation in certain field conditions.

As initially hoped, we have been able to investigate the dynamics of domain wall propagation in FePt single layer with thicknesses of 2, 4, 5 and 6 nm, and in a FePt/MgO/FePt MTJ sample by MOKE. This study has been performed in the Laboratoire de Physique des Solides premises.

After applying magnetic pulses with an intensity below a given value, we observed “Swiss cheese” state and “overhangs” in the propagating domain.. Such features are characteristics of situations when the field is not high enough to reduce the effect of sample disorder on the domain wall propagation.. At higher field, the reversed domain propagates with an increasing velocity when increasing the amplitude of the applied field. Typically, we have been able to determine domain wall speed over more than 1 kOe (in the 1-3 kOe range), with recorded domain wall speeds in the 5-20 m.s⁻¹ range. Indeed, at even higher fields, domain nucleation tends to dominate over the domain wall propagation and prevents a quantitative determination of domain wall speed.

In the MTJ sample, domain wall propagation phenomena are more complex due the stray field interactions between the two layers. This stray field accounts for some specific behaviors. For instance, domain nucleation in the hard layer happens before reaching its quasi-static reversal field, and is specifically observed in parts of the sample already covered by the domain wall propagating in the soft layer. This observation outlined the effect of domain wall stray field in magnetic coupling phenomena.

Experimentally, we observed that- in the investigated thickness range (2-6 nm), higher thickness ends with higher domain wall velocity for a given a given field. We observe velocity anomaly inmost of experimental data that is decreasing velocity when increasing applied field over a limited field range. Such anomalies have been related to the Walker breakdown in many systems, that is to domain wall instability above a given value of the applied field. In our case, we believe that our data are all recorded for fields higher than the Walker field. As a result, we explored the oscillatory propagation regime, in which the expected domain wall velocity is much lower than in the viscous flow regime. We draw this conclusion from consistent comparison of our experimental data with uniaxial models [3.3.4].

In addition, we performed one dimensional micromagnetic simulation of the propagation of the domain wall in FePt thin films. These simulations support the conclusion we drawn from simple models [3.3.5].

These conclusions provoke two comments:

- Practically, sample disorder (*i.e.* structural defects creating magnetic disorder) is responsible for the low field limit for measuring domain wall velocity. There is no specific reason implying that high magnetocrystalline anisotropy thin films could not be grown with a lower density of defects. This is not a small challenge as it would require a control of expitaxy processes still not obtained, but it may be worth trying as thin films with large magnetization and large anisotropy are seducing candidates for high density magnetic logic applications or domain wall based data recording devices. Indeed, such films (as FePt) would combine high data stability due to the large anisotropy, and in not too thin films, significant dipolar field interactions.
- Both the numerical simulations we performed and the comparison of our experimental data with some crude models required or ended up with a value of the damping factor (α) that we have not been able to compare with direct experimental values. It is then clear that an independent determination of the damping factor would be very valuable to support ours conclusions. However, a material such as FePt in the L1₀ phase reveals a very challenging when one wants to perform ferromagnetic resonance (FMR). Indeed

with such a high anisotropy field (7 T range), most FMR experimental setup are not suitable when fitted with standard cavity in the Q-band. Current efforts are then focused on the FMR measurement relying on strip-line.

These experiments have been completed by the observation of the dynamics of domain wall propagation in a full magnetic tunnel junction (FePt/MgO/FePt). Among other results, we observed that domain nucleation may occur in the hard layer in the areas swept by the domain wall in the soft layer, even if the externally applied field is lower than the quasistatic coercive field of the hard layer. This is a clear indication of magnetic coupling between the two layers through the stray field created by a domain wall.

We next focused our efforts on a detailed study of the magnetic coupling in dynamic conditions, when cycling repeatedly the magnetization of the soft layer. Even if the applied field was well below the HL coercive field, a progressive demagnetization of the hard layer is then observed, occurring over tens or hundreds of magnetic cycles. Key results are:

- the demagnetization speed depends on the applied field during cycling
- the demagnetization curve (hard layer magnetization over number of cycles) can be fitted by a single formula taking into account the number of cycles and the applied field
- MFM images outlines the key role of (stray field from) the domain wall propagating in the soft layer in destabilizing the hard layer magnetization
- MFM images reveal a unique growth mode of the reversed domain in the hard layer: compact demagnetized areas (where up and down magnetic ribbons are associated) coexist with vast and still unchanged parts with up magnetization.

BIBLIOGRAPHY

- [ALL05] D. A. Allwood, G. Xiong, C. C. Faulkner, D. Atkinson, D. Petit, R. P. Cowburn, **Magnetic Domain-Wall Logic**, Science **309**, 1688 (2005)
- [ATT03] Jean-Philippe Attané, Interactions entre parois magnétiques et défauts structuraux, et mise en ordre chimique par irradiation, observées dans des couches minces d'alliages FePt(Pd) thèse de doctorat de l'université Joseph Fourier (2003)
- [ATT04] J.P.Attane, Y.Samson, A.Marty, J.C.Toussaint, G.Dubois, A.Mougin, J.P.Jamet, **Magnetic DomainWall Propagation un to the Percolation Threshold across a seudorectangular Disordered Lattice**, Physical Review Letters, volume 93, p257203-1-4 (2004)
- [BAI88] M.N. Baibich, J.M. Broto, A. Fert, F. Nguyen Van Dau, F. Petro, P. Etienne, G. Creuzet, A. Friederich, J. Chazelas, **Giant magnetoresistance of (001)Fe/(001)Cr magnetic superlattices** ,Physical Review Letters, volume 61, issue 21, p2472-2475 (1988)
- [BEL05] K.D.Belashchenko, J.Velev, E.Y.Tsymbal, **Effect of interface states on spin-dependent tunneling in Fe/MgO/Fe tunnel junctions**, Physical Review B, volume 72, p140404-1-4 (2005)
- [BON01] M. Bonfim, G. Ghiringhelli, F. Montaigne, S. Pizzini, N. B. Brookes, F. Petroff, J. Vogel, J. Camarero, and A. Fontaine **Element-Selective Nanosecond Magnetization Dynamics in Magnetic Heterostructures** Volume 86, Number 16 Physical Review Letters (2001)
- [BOW01] M. Bowen, V. Cros, F. Petroff, A. Fert, C. Martínez Boubeta, J. L. Costa-Krämer, J. V. Anguita, A. Cebollada, F. Briones, J. M. de Teresa, L. Morellón, M. R. Ibarra, F. Güell, F. Peiró, et A. Cornet **Large magnetoresistance in Fe/MgO/FeCo(001) epitaxial tunnel junctions on GaAs(001)** Applied Physis Letters **79**, 1655 (2001)

- [BUT01] W.H. Butler, X.G. Zhang, T.C. Schulthess, **Spin-dependent tunneling conductance of Fe/MgO/Fe sandwiches**, Physical Review B, volume 63, issue 5, p054416-1-12 (2001)
- [CHS02] M. Chshiev, D. Stoeffler, A. Vedyayev and K. Ounadjela **Magnetic diode effect in double-barrier tunnel junctions** *Europhys. Lett.*, **58** (2), pp. 257–263 (2002)
- [CHE02] X. Chen, O. Sichel Schmidt, W. Kleemann, O. Petravic, C. Binek, J. B. Sousa, S. Cardoso, and P. P. Freitas, **Domain Wall Relaxation, Creep, Sliding, and Switching in Superferromagnetic Discontinuous Co₈₀Fe₂₀=Al₂O₃ Multilayers** Physical Review Letters. **89**, 137203 (2002)
- [DIE91] B.Dieny, V.S.Speriosu, S.Metin, S.S.P.Parkin, B.A.Gurney, D.R.Wilhoit, D.Mauri, **Giant magnetoresistance in soft ferromagnetic multilayers**, Physical Review B, volume 43, number 1, p1297-1300 (1991)
- [FAU03] J. Faure-Vincent, C. Tiusan, E. Jouguelet, F. Canet, M. Sajieddine, C. Bellouard, E. Popova, M. Hehn, F. Montaigne, et A. Schuhl **High tunnel magnetoresistance in epitaxial Fe/MgO/Fe tunnel junctions** Applied Physic Letters. **82**, 4507 (2003)
- [FAU04] J.Faure-Vincent, Transport tunnel polarisé en spin dans le système épitaxié Fe/MgO/Fe: Interactions magnétiques et Symétries électroniques, thèse de doctorat de l'Institut National Polytechnique de Lorraine (2004)
- [FER97] J. Ferré, V. Grolier, P. Meyer, S. Lemerle, A. Maziewski, E. Stefanowicz, S. V. Tarasenko, V. Tarasenko, M. Kisielewski, D. Renard, **Magnetization-reversal processes in an ultrathin Co/Au film** Physical Review B, volume **55**, number 22 (1997)
- [FUK06] K. Fukumoto *et al* **Dynamics of Magnetic Domain Wall Motion after Nucleation: Dependence on the Wall Energy** Physical Review Letters 96, 097204 (2006)
- [FUL92] E. Fullerton, J. E. Mattson, S. R. Lee, C. H. Sowers, Y. Y. Huang, G. Felcher, S. D. Bader et F. T. Parker J. **Non-oscillatory antiferromagnetic coupling in sputtered Fe/Si superlattices** Magn. Magn. Matter. **117**, L301 (1992)
- [FUL99] E. Fullerton, J. S. Jiang et S. D. Bader **Hard/soft magnetic heterostructures : model exchange-spring magnets** J. Magn. Magn. Matter. **200**, 392 (1999)
- [GEH97] Véronique Gehanno, **Anisotropie magnétique perpendiculaire des couches minces épitaxiées d'alliages ordonnés FePd**, Thèse de doctorat de l'Institut National Polytechnique de Grenoble (1997)
- [GEH97a] V. Gehanno, Y. Samson, A. Marty, B. Gilles et A. Chamberod **Magnetic susceptibility and magnetic domain configuration as a function of the layer thickness in epitaxial FePd(001) thin films ordered in the L10 structure**, Journal of Magnetism and Magnetic Materials 172 (1997) 26-40
- [GEH97b] V. Gehanno and A. Marty **Magnetic domains in epitaxial ordered FePd.001. thin films with perpendicular magnetic anisotropy** Physical Review B Volume 55, Number 18 (1997)
- [GEH99] V.Gehanno, R.Hoffmann, Y.Samson, A.Marty, S.Auilet **In plane to out of plane magnetic reorientation transition in partially ordered FePd thin films**, European Physical Journal B, number 10, p457-464 (1999)

- [GID98] S. Gider, B.-U. Runge, A. C. Marley, S. S. P. Parkin, **The Magnetic Stability of Spin-Dependent Tunneling Devices**, SCIENCE Vol 281 (1998), p 797 - 799
- [GOT65] E. Goto, N. Hayashi, T. Miyashita, et K. Nakagawa **Magnetization and Switching Characteristics of Composite Thin Magnetic Films** Journal of Applied Physic. 36, 2951 (1965)
- [GRO02] J. Grollier, D. Lacour, V. Cros, A. Hamzic, A. Vaurès, A. Fert, D. Adam and G. Faini, **Switching the magnetic configuration of a spin valve by current induced domain wall motion**, Journal of Applied Physic. **92** 4825 (2002).
- [GRU86] Grünberg, P., R. Schreiber, Y. Pang, M. B. Brodsky, and H. Sowers, **Layered magnetic structures: Evidence for antiferromagnetic coupling of Fe layers across Cr-interlayer**, Physical Review Letters **57**, 2442 (1986).
- [HAL01] D. Halley, Y. Samson, A. Marty, C. Beigné, B. Gilles, **Surface morphology and chemical ordering in FePd/Pd(001) thin layers**, Surface science, volume 481, p25-32 (2001)
- [HAL02] D. Halley, Y. Samson, A. Marty, P. Bayle-Guillemaud, C. Beigné, B. Gilles, J. E. Mazille, **Anomaly of strain relaxation in thin ordered FePd layers**, Physical Review B, volume 65, issue 20, p205408-1-8 (2002)
- [HAL04] D. Halley, A. Marty, P. Bayle-Guillemaud, B. Gilles, J. P. Attane, Y. Samson, **Chemical order and selection of the mechanism for strain relaxation in epitaxial FePd(Pt) thin layers**, Physical Review B, volume 70, p174438-1-5 (2004)
- [HUB98] Alex Hubert, Rudolf Schäfer **Magnetic domain: the analysis of Magnetic microstructure** Springer, 1998, 696 pages
- [HUR69] P. HURAULT **Tunnelling through impure barriers** Physical Review B vol. 185, num. 2, p. 592-602 (1969)
- [IKE08] S. Ikeda, J. Hayakawa, Y. Ashizawa, Y. M. Lee, K. Miura, H. Hasegawa, M. Tsunoda, F. Matsukura, and H. Ohno **Tunnel magnetoresistance of 604% at 300 K by suppression of Ta diffusion in CoFeB/MgO/CoFeB pseudo-spin-valves annealed at high temperature** Applied Physic Letters **93** 82508 (2008)
- [JAN00] R. Jansen and J. C. Lodder **Resonant tunneling via spin-polarized barrier states in a magnetic tunnel junction** Physical Review B Volume 61, Number 9 (2000)
- [JAN98] R. Jansen and J. S. Moodera **Influence of barrier impurities on the magnetoresistance in ferromagnetic tunnel junctions** Journal of Applied Physics Volume 83, Number 11 (1998)
- [JAN99] R. Jansen and J. S. Moodera **Enhanced tunnel magnetoresistance in Fe-doped Al₂O₃ barriers** Applied Physics Letters Volume 75, Number 3 (1999)
- [JAN99] R. Jansen and J. S. Moodera **Magnetoresistance in doped magnetic tunnel junctions: Effect of spin scattering and impurity-assisted transport** Physical Review B Volume 61, Number 13 (2000)
- [JUL75] M. Jullière, **Tunneling between ferromagnetic films**, Physics Letters A, volume 54, issue 3, p225-226 (1975)
- [KAP93] B. Kaplan, G. A. Gehring, **The domain structure in ultrathin magnetic films**, Journal of Magnetism and Magnetic Materials, volume 128, p111-116 (1993)

- [KAN05] F. Kanjouri *et al* **Diode effect in magnetic tunnel junctions with impurities** Journal of Applied Physics **98**, 083901 (2005)
- [KEA96] D. J. Keavney, E. E. Fullerton, and S. D. Bader **Perpendicular conductance and magnetic coupling in epitaxial Fe/MgO/Fe(100) trilayers** Journal of Applied Physics **81**, 795 (1996)
- [KIR93] A. Kirilwk, J. Ferre, D. Renard **Domain Walls in Ultrathin Ferromagnetic Films: Velocity and Fractal Dimension** Europhysics Letters., **24** (5), pp. 403-408 (1993)
- [KLE07] W. Kleemann, J. Rhensius, O. Petravic, J. Ferre, J.P. Jamet, and H. Bernas, **Modes of Periodic DomainWall Motion in Ultrathin Ferromagnetic Layers** Physis Review Letters **99**, 097203 (2007)
- [LEE80] F H De Leeuw, R Van Den Doel and U Enz **Dynamic properties of magnetic domain walls and magnetic bubbles** Rep. Prog. Phys., Vol. 43, (1980)
- [LEW03] W.S.Lew, S.P.Li, L.Lopez-Diaz, D.C.Hatton, J.A.C.Bland, **Mirror Domain Structures Induced by Interlayer MagneticWall Coupling** , Physical Review Letters, volume 90, number 21, p217201-1-4 (2003)
- [LYB99] A Lyberatos and J Ferré **Domain wall velocity in ultra-thin magnetic films with perpendicular anisotropy** Journal Physis D: Applied Physis **33** (2000) 1060–1069.
- [MAL79] A.P Malozemoff, J .C Slonczewski **Magnetic Domain walls in Bubble materials** Academic Press (1979)
- [MAS08] Masatoshi Yoshikawa, Eiji Kitagawa, Toshihiko Nagase, Tadaomi Daibou, Makoto Nagamine, Katsuya Nishiyama, Tatsuya Kishi, and Hiroaki Yoda **Tunnel Magnetoresistance Over 100% in MgO-Based Magnetic Tunnel Junction Films With Perpendicular Magnetic L1₀-FePt Electrodes** IEEE Transactions On Magnetics, Vol. 44, No. 11, (2008)
- [MAT01] J.Mathon, A.Umerski, **Theory of tunneling magnetoresistance of an epitaxial Fe/MgO/Fe(001) junction**, Physical Review B, volume 63, issue 22, p220403-1-4 (2001)
- [MAT02] J Mathon, **Theory of spin-dependent tunnelling in magnetic junctions**, Journal Physis D: Applied Physis **35**, 2437-2443 (2002)
- [MET07] P. J. Metaxas, J. P. Jamet, A. Mougin, M. Cormier, J. Ferré, V. Baltz, B. Rodmacq, B. Dieny, and R. L. Stamps, **Creep and flow regimes of magnetic domain wall motion in ultrathin Pt/Co/Pt films with perpendicular anisotropy** Physical Review Letters, **99**, 217208 (2007)
- [MET07] P.J. Metaxas, J.P. Jamet, J. Ferré, B. Rodmacq, B. Dieny, R.L. Stamps **Magnetic domain wall creep in the presence of an effective interlayer coupling field** J. Magn. Mater. **320** 2571 (2008)
- [MEY01] H. L. Meyerheim, R. Popescu, J. Kirschner, N. Jedrecy, M. Sauvage-Simkin, B. Heinrich and R. Pinchaux **Geometrical and Compositional Structure at Metal-Oxide Interfaces: MgO on Fe(001)** Physical Review Letters **87** 076102 (2001)
- [MOO95] J.S.Moodera, L.R.Kinder, T.M.Wong, R.Meservey, **Large magnetoresistance at room temperature in ferromagnetic thin films tunnel junctions**, Physical Review Letters, volume 74, number 16, p3273-3276 (1995)

- [MOU07] A. Mougín, M. Cormier, J. P. Adam, P. J. Metaxas and J. Ferré “**Domain wall mobility, stability and Walker breakdown in magnetic nanowires**” EPL **78** 57007
- [OKA02] Okamoto, S., Kikuchi, N., Kitakami, O., Miyazaki, T., Shimada, Y. & Fukamichi **Competition between ferromagnetism and antiferromagnetism in FePt** Physical Review Letters, **66** 024413 (2002)
- [PAR91] S. S. P. Parkin, R. Bhadra and K. P. Roche **Oscillatory Magnetic exchange coupling through thin copper layers** Physical Review Letters volume 66, number 16 page 2152 (1991)
- [PAR04] S.S.P.Parkin, C.Kaiser, A.Panchula, P.M.Rice, B.Hughes, M.Amant, S.H.Yang, **Giant tunnelling magnetoresistance at room temperature with MgO (100) tunnel barriers**, nature materials, volume 3, p862-867 (2004)
- [PAR08] Stuart S. P. Parkin,* Masamitsu Hayashi, Luc Thomas, **Magnetic Domain-Wall Racetrack Memory**, Science **320** 190 (2008)
- [PER07] P. de Person PhD manuscript, University Joseph Fourier Grenoble I France (2007)
- [PER07b] P. de Person, P. Warin, M. Jamet, C. Beigne, and Y. Samson **Magnetic coupling between high magnetization perpendicular electrodes in an epitaxial FePt/MgO/FePt magnetic tunnel junction** Physical Review B **76**, 184402 (2007)
- [SAM99] Y. Samson, A. Marty, R. Hofmann, V. Gehanno, B. Gilles, **Magnetic domains in thin films with perpendicular anisotropy: An extensive study**, Journal of Applied Physics, volume 85, number 6, p4604-4606 (1999)
- [SEK03] T.Seki *et al.* **11_0 ordering of off-stoichiometric FePt(001) thin films at reduced temperature** Applied Physics Letters, Vol 82, num 15, 2461-2463 (2003)
- [SEK06] T.Seki *et al.* **Spin-polarized current-induced magnetization reversal in perpendicularly magnetized $L1_0$ -FePt layers** Applied Physics Letters, Vol 88, 172504 (2006)
- [SIM63] J.G. Simmons *et al.* **Generalized formula for the electric tunnel effect between similar electrodes separated by a thin insulating film**, Journal of Applied Physics, volume 34, number 6, p1793-1803 (1963)
- [SOU99] R.C.Sousa, M.Kerekes, I.L.Prejbeanu, O.Redon, B.Dieny, J.P.Nozières, P.P.Freitas, **Crossover in heating regimes of thermally assisted memories**, Journal of Applied Physics, volume 99, p08N904- 1-3 (1999)
- [THO99] Luc Thomas, Jan Lüning, Andreas Scholl, Frithjof Nolting, Simone Anders, Joachim Stöhr, and Stuart S. P. Parkin **Oscillatory Decay of Magnetization Induced by Domain-Wall Stray Fields** Physical Review Letters Volume 84, Number 15 April 2000
- [THO00] L.Thomas, M.G.Samant, S.S.P.Parkin, **Domain-Wall Induced Coupling between Ferromagnetic Layers**, Physical Review Letters, volume 84, number 8, p1819-1819 (2000)
- [TIU04] C.Tiusan, J.Faure-Vincent, C.bellouard, M.Hehn, E.Jouguelet, A.Schuhl, **Interfacial Resonance State probed by Spin-polarized tunneling in epitaxial Fe/MgO/Fe tunnel junctions**, Physical Review Letters, volume 93, number 10, p106602-1-4 (2004)

- [TIU06] C.Tiusan, M.Sicot, J.Faure-Vincent, M.Hehn, C.Bellouard, F.Montaigne, S.Andrieu, A.Schuhl, **Static and dynamic aspects of spin tunneling in crystalline magnetic tunnel junctions**, Journal of Physics : Condensed Matter, volume 18, p941-956 (2006)
- [TSY03] Evgeny Y Tsymbal, OlegN Mryasov and Patrick R LeClair **Spin-dependent tunnelling in magnetic tunnel junctions** Journal of Physics: Condens. Matter **15** (2003) R109–R142
- [TUS05] C.Tusche, H.L.Meyerheim, N.Jedrecy, G.Renaud, A.Ernst, J.Henk, P.Bruno, J.Kirschner, **Oxygen-Induced Symmetrization and Structural Coherency in Fe/MgO/Fe(001) Magnetic Tunnel Junctions**, Physical Review Letters, volume 95, p176101-1-4 (2005)
- [WIE06] S. Wiebel, J.-P. Jamet, N. Vernier, A. Mougin, J. Ferré, V. Baltz, B. Rodmacq, and B. Dieny **Magnetic domain structure and dynamics in interacting ferromagnetic stacks with perpendicular anisotropy** Journal of Applied Physics **100**, 043912 (2006)
- [WOR03] D. C. Worledge and P. L. Trouilloud **Magnetoresistance measurement of unpatterned magnetic tunnel junction wafers by current-in-plane tunnelling** Applied Physics Letters Volume 83, Number 1 (2003)
- [WUL01] W. Wulfhekkel,a) M. Klaua, D. Ullmann, F. Zavaliche, J. Kirschner, R. Urban, T. Monchesky, and B. Heinrich, Applied Physis Letters **78**, 509 (2001)
- [YOU99] J. Ben Youssef *et al*, J. Magn. Magn. Mat **202** 277 (1999)
- [YUA00] S.Yuasa, T.Sato, E.Tamura, Y.Suzuki, H.Yamamori, K.Ando, T.Katayama, **Magnetic tunnel junctions with single-crystal electrodes: a crystal anisotropy of tunnel magneto-resistance**, Europhysics Letters, volume 52, number 3, p344-350 (2000)
- [YUA04] S. Yuasa, A. Fukushima, T. Nagahama, K. Ando, et Y. Suzuki **High Tunnel Magnetoresistance at Room Temperature in Fully Epitaxial Fe/MgO/Fe Tunnel Junctions due to Coherent Spin-Polarized Tunneling** Japan Journal of. Applied Physis 43, No. 4B (2004)
- [YUJ08] Yujiro Taniguchi, Yoshio Miura, Kazutaka Abe, and Masafumi Shirai **Theoretical Studies on Spin-Dependent Conductance in FePt/MgO/FePt(001) Magnetic Tunnel Junctions** IEEE Transactions On Magnetism, VOL. 44, NO. 11 (2008)
- [ZHA03] X.G.Zhang, W.H.Butler, A.Bandyopadhyay **Effects of the iron-oxide layer in [Fe/FeO/MgO/Fe tunneling junctions**, Physical Review B, volume 68, p092402-1-4 (2003)
- [ZHA04] X.G.Zhang, W.H.Butler **Large magnetoresistance in bcc Co/MgO/Co and FeCo/MgO/FeCo tunnel junctions**, Physical Review B, volume 70, p172407-1-4 (2004)
- [ZHA97] Xiangdong Zhang *et al*. **Spin-polarized tunneling and magnetoresistance in ferromagnet/insulator.semiconductor. single and double tunnel junctions subjected to an electric field**, Physical Review B, volume 56, Number 9 1997

Abstract

Epitaxial (MgO barrier) magnetic tunnel junctions (MTJs) are the most promising systems for applications ranging from high performance recording heads to magnetic random access memories (MRAM). Besides, such junctions also involves new and fascinating physics, such as the physics of electronic transport across epitaxial barriers, or the physics of magnetic coupling across a thin barrier.

We described results obtained on MTJs perpendicular FePt/MgO/FePt magnetization. Far less studied, systems with perpendicular magnetization may have the highest potential for use at the highest recording densities in MRAM. We demonstrated that high magnetic anisotropy – L_{10} phase FePt layers can be grown in FePt/MgO/FePt trilayers, spontaneously with one soft and one hard layer. In addition, full magnetic decoupling is obtained in spite of the large magnetization of both layers. The manuscript then focuses on two studies.

First, we observe the domain wall propagation speed on FePt single layers, as a function of both the applied field and of the layer thickness (from 2 to 6 nm), thereby extending the studies previously limited to ultrathin Pt/Co/Pt films to non-zero thicknesses.

Second, we observed in details the magnetic coupling phenomena between the two FePt layers in full MTJs. By combining magneto-optical (macroscopic) studies and Magnetic Force Microscopy imaging, we gained a detailed understanding of the origin of the coupling, and of the process by which the cycling of the soft layer can induce a progressive demagnetization of the hard one.

Résumé

Les jonctions tunnel magnétiques (JTM) épitaxiées à barrière MgO constituent probablement le système le plus prometteur pour des applications allant depuis les têtes de lecture des disques durs jusqu'aux mémoires magnétiques à accès aléatoire. De plus, de telles jonctions mettent en jeu une physique nouvelle et fascinante, celle de la physique du transport électronique au travers de barrières épitaxiées, ou du couplage magnétique entre électrodes au travers d'une fine barrière.

Nous présentons des travaux conduits sur des jonctions à perpendiculaire (FePt/MgO/FePt). Très peu étudiés, les systèmes à aimantation perpendiculaire semblent présenter le potentiel le plus élevé aux très hautes densités dans les mémoires MRAM. Nous avons montré que des jonctions FePt/MgO/FePt peuvent être obtenues avec des couches de FePt chimiquement ordonnées dans la phase L_{10} de très forte anisotropie magnétocristalline. Ces jonctions présentent spontanément une couche dure et une couche douce, et un découplage magnétique en dépit de la forte aimantation volumique de l'alliage FePt. La thèse porte alors principalement sur deux études :

- la propagation de parois dans des films minces de FePt, en fonction du champ appliqué et de l'épaisseur de la couche mince (entre 2 et 6 nm). Nous étendons ici les études auparavant réalisées dans la limite de films ultra-minces (Pt/Co/Pt)/
- les phénomènes de couplage magnétique entre électrodes à aimantation perpendiculaire dans la jonction complète. En combinant études macroscopiques (magnéto-optiques) et locales, nous proposons une description détaillée de l'origine du couplage magnétique, et du processus qui peut conduire à la démagnétisation progressive de la couche dure lors du cyclage de la couche douce.